Seismic Response Assessment of Ductile and Non-Ductile Reinforced Concrete Columns Affected by Corrosion and Axial Load Variations

Doctoral Thesis

by

Safdar Naveed Amini

(2018CEZ0001)

DEPARTMENT OF CIVIL ENGINEERING

INDIAN INSTITUTE OF TECHNOLOGY ROPAR

December, 2024

Seismic Response Assessment of Ductile and Non-Ductile Reinforced Concrete Columns Affected by Corrosion and Axial Load Variations

A Thesis Submitted

In Partial Fulfillment of the Requirements

for the Degree of

Doctor of Philosophy

by

Safdar Naveed Amini

(2018CEZ0001)

DEPARTMENT OF CIVIL ENGINEERING

INDIAN INSTITUTE OF TECHNOLOGY ROPAR

December, 2024

Safdar Naveed Amini: *Seismic Response Assessment of Ductile and Non-Ductile Reinforced Concrete Columns Affected by Corrosion and Axial Load Variations.*

DEDICATED TO

MY MOTHER, FATHER,

SISTERS, WIFE & MENTORS

Declaration of Originality

I hereby declare that the work being presented in the thesis entitled **Seismic Response Assessment of Ductile and Non-Ductile Reinforced Concrete Columns Affected by Corrosion and Axial Load Variations** has been solely authored by me. It presents the result of my own independent investigation/research conducted during the time period from the 23rd of February 2022 to the 30th of March 2024 under the supervision of Dr. Aditya Singh Rajput, Assistant Professor, IIT Ropar. To the best of my knowledge, it is an original work, both in terms of research content and narrative, and has not been submitted or accepted elsewhere, in part or in full, for the award of any degree, diploma, fellowship, associateship, or similar title of any university or institution. Further, due credit has been attributed to the relevant state-of-the-art collaborations (if any) with appropriate citations and acknowledgments in line with established ethical norms and practices. I also declare that any idea/data/fact/source stated in my thesis has not been fabricated/ falsified/ misrepresented. All the principles of academic honesty and integrity have been followed. I fully understand that if the thesis is found to be unoriginal, fabricated, or plagiarized, the Institute reserves the right to withdraw the thesis from its archive and revoke the associated Degree conferred. Additionally, the Institute also reserves the right to appraise all concerned sections of society of the matter for their information and necessary action (if any). If accepted, I hereby consent for my thesis to be available online in the Institute's Open Access repository, inter-library loan, and for the title and abstract to be made available to outside organizations.

Signature
Name: Safdar Naveed Amini
Entry Number: 2018CEZ0001
Program: PhD
Department: Civil Engineering
Indian Institute of Technology Ropar Rupnagar, Punjab 140001

Date: 25 December 2024

Acknowledgments

I take I am profoundly grateful for the invaluable guidance and support I have received throughout my doctoral journey. My heartfelt gratitude to Dr. Aditya Singh Rajput for his exceptional mentorship, kindness and steadfast support. Dr. Rajput's expertise, patience and commitment have been instrumental in shaping both the direction and outcomes of this research. His insightful feedback, continuous monitoring and guidance have been crucial in fostering my academic development.

I also extend my sincere gratitude to the members of my doctoral committee, Dr. Mitesh Surana, Dr. Putul Haldar and Dr. Khushboo Rakha. Their profound insights and constructive advice have significantly enriched my research, contributing greatly to its depth and quality.

I am also deeply appreciative of the staff members and technicians of the Central Workshop for their indispensable assistance in specimen preparation and testing. Additionally, I extend special thanks to the maintenance personnel at the Central Civil Workshop, whose diligent efforts in maintaining a clean and organized laboratory environment were essential for the smooth execution of experiments. Their commitment to ensuring a well-maintained workspace was highly valued.

Finally, I wish to convey my heartfelt gratitude to the Almighty and to my parents, my beloved mother and father. Their unwavering encouragement, love, and support have been the foundation of my academic and personal growth. Their belief in my potential has continually inspired and motivated me. I also dedicate this thesis to my sisters, whose continuous motivation, prayers, and blessings have been a source of strength throughout my academic journey.

This journey has been challenging yet immensely rewarding, and I am profoundly thankful to all those who have supported and contributed to its success.

Safdar

Safdar Naveed Amini

Certificate

This is to certify that the thesis entitled "**Seismic Response Assessment of Ductile and Non-Ductile Reinforced Concrete Columns Affected by Corrosion and Axial Load Variations**", submitted by Safdar Naveed Amini (2018CEZ0001) for the award of the degree of Doctor of Philosophy of Indian Institute of Technology Ropar, is a record of bonafide research work carried out under my (our) guidance and supervision. To the best of my knowledge and belief, the work presented in this thesis is original and has not been submitted, either in part or full, for the award of any other degree, diploma, fellowship, associateship or similar title of any university or institution.

In my opinion, the thesis has reached the standard of fulfilling the requirements of the regulations relating to the Degree.

Aditya Rajput

Signature of the Supervisor
Name: Dr. Aditya Singh Rajput
Department: Civil Engineering
Indian Institute of Technology Ropar
Rupnagar, Punjab 140001
Date: 25-12-2024

Lay Summary

The study comprehensively explored the combined impacts of corrosion and varying axial loads on the seismic response of both ductile and non-ductile reinforced concrete columns. These columns are fundamental structural elements responsible for bearing the entire load of a building, thus playing an essential role in maintaining the structural integrity of buildings. Understanding the interactions between corrosion and axial compression variations on these key components is paramount for ensuring the long-term durability and reliability of structures exposed to natural disasters, such as earthquakes and floods, as well as to accidental loadings and differential settlements.

The primary objective of this research was to assess how corroded columns behave under seismic conditions, and to achieve this, detailed simulation models were developed and calibrated using experimental data. The developed models were rigorously validated, serving as a basis for an extensive parametric analysis that aimed to deepen understanding of the intricate dynamics involved.

A significant focus of the study was on quantifying the damage in the hinge region of columns, specifically under varying degrees of corrosion and axial compression. This region is critical as it significantly influences the overall ductile performance of the structure during seismic activity. To evaluate the impact of these factors on column performance, several parameters were analyzed, including hysteresis and backbone curves, stiffness degradation, ductility, and energy dissipation capacity. The study encompassed a detailed examination of both ductile and non-ductile columns, each with distinct lateral tie configurations.

The findings of this investigation contribute valuable insights into how the severity of corrosion and levels of axial compression affect the seismic resilience of reinforced concrete columns. These results provide engineers with a robust framework for predicting the remaining strength and service life of such columns, thereby aiding in the assessment and enhancement of the safety and stability of entire structures. This work underscores the importance of integrating corrosion and axial load factors into structural evaluations and maintenance strategies, especially for structures located in seismically active or corrosive environments.

Abstract

This research delves into the combined impacts of reinforcement corrosion and axial compression ratio (ACR) on the seismic performance of large-scale ductile and non-ductile reinforced concrete (RC) columns. The study employed quasi-static cyclic lateral loading tests with progressively increasing magnitudes to simulate seismic conditions. Initially, the seismic behaviour of control ductile and non-ductile RC columns was examined. The theoretical axial load capacity (P0) under concentric axial loading was calculated, and an axial load equivalent to 0.35P0 was applied consistently during seismic testing. The construction of the columns featured distinct lateral reinforcement ratios—1.31% for ductile columns and 0.33% for non-ductile columns—to highlight the performance differences.

A detailed parametric study was conducted using three-dimensional (3D) simulation models in ABAQUS, which were calibrated and validated against experimental data to ensure reliability. To investigate the influence of ACR on column performance, a comprehensive analysis was performed by varying the ACR from 0.35P0 to 0.7P0. Results demonstrated that ductile columns exhibited a modest increase in peak strength up to an ACR of 0.5P0, accompanied by a consistent reduction in ductility. In contrast, non-ductile columns experienced a pronounced decline in peak strength, deformability, and overall ductility with increasing ACR levels.

Further, to evaluate the combined effects of varying corrosion levels and ACR on column behaviour, advanced 3D numerical models of corroded RC columns were developed and rigorously validated through experimental testing to evaluate the combined effects of varying corrosion levels and ACR on column behaviour. Key performance parameters such as hysteresis and backbone curves, stiffness degradation, ductility, equivalent viscous damping, and energy dissipation were meticulously calculated and compared across different conditions. The findings revealed that both ductile and non-ductile columns subjected to corrosion showed significant reductions in strength, deformability, stiffness, and ductility at higher ACR levels. The increased ACR led to diminished pre-peak and post-peak response characteristics and resulted in peak response reaching lower drift levels, indicating reduced seismic resilience.

This condition precipitated various deterioration phenomena, including longitudinal cracking, spalling of the concrete cover, and the weakening of the bond between reinforcing steel and concrete. These observations underscore the critical importance of factoring in ACR and corrosion impacts in the design and maintenance of RC columns to enhance their seismic performance and structural reliability.

Keywords: Axial Compression Ratio, Corrosion, Ductile columns, Modelling, Non-ductile columns, Reinforced Concrete, Seismic Analysis

Table of Contents

List of Figures

List of Tables

Notations and Abbreviations

Acronyms

Symbols	**Description**
A/S	Abaqus-Standard
ACR	Axial Compression Ratio
C3D8R	8-node Linear Hexahedral Solid Element with Reduced Integration
CDP	Concrete Damaged Plasticity
CO_2	Carbon Dioxide
3D	Three Dimensional
FE	Finite Element
GFRP	Glass Fiber-Reinforced Polymer
LVDT	Linear Variable Differential Transformer
NSRC	Non-Seismically designed Reinforced concrete
RC	Reinforced Concrete
SAP	Structural Analysis Program
SC	Smeared Cracking
T3D2	Two-node Three-Dimensional Truss Element
WCO	World Corrosion Organization

List of symbols

Symbols	**Description**
A_{sh}	Area provided
C	Clear concrete cover
d	Yield Damage Variable
d_b	Diameter of anchored steel bars
ε_{c1}	Strain at peak stress
ε_c	Concrete strain at peak load
E_{c1}	Secant modulus of elasticity
E_s	Modulus of elasticity of Steel
E_{ef}	Effective elastic modulus
E_u	Ultimate cumulative energy dissipation
f_{b0}/f_{c0}	Ratio of initial equibiaxial compressive yield stress to initial compressive yield stress
f_{cm}	Peak stress

f_{cc}	Reduced compressive strength of concrete
f_{tt}	Reduced tensile strength of concrete
f_{uc}	Ultimate stress
f_{yc}	Yield stress
f_c	Maximum compressive strength of uncorroded concrete
F_u	Ultimate force
K_c	Ratio of the second stress invariant on the tensile meridian
k	Parameter that relies on diameter and roughness of reinforcement
K	Stiffness
K_0	Initial stiffness
l_c	Characteristic length
P_{cor}	Radial pressure caused by corrosion
ξ_{eq}	Equivalent Viscous Damping ratio
t_n	Nominal stresses in normal direction
ts	Shear stress
T	Time period for corrosion
t_t	Stress in tangential directions
S_s	Spacing between shear stirrups
S_{max}	Maximum bond stress
V	Lateral load
$v_{r/s}$	Ratio of volumetric expansion of oxides with respect to virgin material
W_{cr}	Crack width
Δ_y	Yield displacement
Δ_p	Deformability
μ	Ductility Factor
τ_{max}	Maximum bond strength

Greek symbols

Symbol	**Description**
ψ	Dilatation angle
α	Enthalpy efficiency
ε	Flow potential eccentricity
μ	Viscosity parameter
θ	Poisson's ratio

Chapter 1

Introduction

1.1 Background

Reinforced concrete (RC) structures are among the most widely used and versatile construction systems in the world. Combining two fundamental materials—concrete and steel—these structures capitalize on the strengths of each component to deliver exceptional performance in a wide range of applications, from buildings and bridges to dams and highways. Concrete, a composite material made primarily of cement, aggregates, water, and admixtures, offers remarkable compressive strength, durability, and resistance to environmental effects. However, it is inherently weak in tension, making it susceptible to cracking under tensile loads.

To overcome this limitation, steel reinforcements, commonly referred to as rebars, are embedded within the concrete to create a composite system. Steel, with its high tensile strength, ductility, weldability, and elastic properties, complements the compressive capabilities of concrete, ensuring the structural elements can resist various types of stresses. This synergy between concrete and steel has made reinforced concrete an indispensable material in modern construction, providing engineers with a reliable solution for constructing robust, long-lasting infrastructure.

While RC structures exhibit remarkable strength and durability under normal conditions, they are not immune to deterioration. Among the most critical challenges faced by RC structures is the problem of corrosion of steel reinforcements. Corrosion is an electrochemical process where steel, due to its thermodynamically unstable nature, reacts with environmental agents such as oxygen, water, and chlorides. This reaction leads to the formation of rust, causing significant damage to the steel and the surrounding concrete.

Corrosion often begins unnoticed but can have profound consequences over time. As the steel corrodes, its cross-sectional area decreases, reducing its load-carrying capacity. Simultaneously, the rust formed during corrosion expands, exerting tensile stresses on the surrounding concrete. This can result in cracking, delamination, and spalling of the cover concrete, further exposing the reinforcement to environmental elements and accelerating the degradation process. In severe cases, this deterioration compromises the safety, serviceability, and lifespan of the structure, leading to costly repairs, retrofitting, or even premature failure.

The deterioration caused by corrosion impacts the structural performance of RC elements in numerous ways. The reduction in reinforcement strength and bond between steel and concrete decreases the load-carrying capacity, ductility, and stiffness of structural members. This deterioration compromises the overall stability of the structure, making it vulnerable to serviceability issues, such as excessive deflections and cracking, and, in extreme cases, structural failure. These effects are particularly concerning in critical infrastructure such as bridges, hospitals, and high-rise buildings, where structural reliability is paramount for the safety of occupants.

The problem of corrosion becomes even more critical when considering the seismic response of RC structures. The capacity of a structure to withstand seismic forces and provide the desired seismic response depends heavily on the ductility and energy dissipation properties of its members. Corrosion adversely affects both of these attributes. The loss of cross-sectional area reduces the ductility of steel reinforcements, while the weakening of bond strength impairs the composite action between steel and concrete, which is essential for energy absorption during seismic events. Corroded RC elements exhibit reduced stiffness and strength, leading to amplified displacements and higher vulnerability to damage under earthquake-induced loads. In severe cases, corrosion can lead to brittle failure mechanisms, drastically reducing the structure’s ability to withstand seismic forces and increasing the risk of collapse. The combined effects of reduced structural capacity, impaired ductility, and compromised seismic response underscore the urgency of addressing corrosion in RC structures.

Among all structural elements in RC buildings, columns are perhaps the most critical to the overall stability and integrity of the structure. Acting as the primary load-bearing members, columns transfer vertical loads from the upper levels of a building to the foundation and play a vital role in resisting lateral forces during seismic events. Their contribution to the global stability of the structure is unparalleled; even minor reductions in their capacity can have significant repercussions on the building’s safety and performance. Therefore, the structural implications of corroded columns are severe. A reduction in the load-bearing capacity of columns affects the entire load path of a building, potentially leading to partial or complete collapse under service loads. In seismic conditions, the consequences become even more dire. Corroded columns exhibit reduced stiffness, ductility, and energy dissipation capacity, all of which are critical for absorbing and redistributing seismic forces. This degradation increases the likelihood of structural instability during an earthquake, as the columns may fail to support lateral and vertical loads simultaneously.

The global impact of corrosion in columns extends beyond localized damage. A single compromised column can trigger a cascade of failures in the surrounding elements, leading to progressive collapse. This phenomenon is particularly dangerous in high-rise buildings and critical infrastructure, where the failure of even a few columns can have catastrophic consequences. Additionally, in earthquake-prone areas, corroded columns significantly heighten the risk of brittle failure mechanisms, as the reduced capacity and confinement compromise the structure’s ability to undergo plastic deformation and absorb seismic energy.

Previous research studies have extensively investigated the effects of reinforcement corrosion on the structural and seismic behaviour of RC columns. These studies have consistently reported significant reductions in stiffness, load-carrying capacity, and ductility due to corrosion (Anh Huy et al., 2022; Cairns et al., 2008; Fernandez et al., 2018; Zandi et al., 2011)

In addition to these findings, other researchers (D. Li et al., 2018; Ma et al., 2012; Yang et al., 2016) have carried out experimental investigations on multiple RC columns to evaluate how varying levels of rebar corrosion affect their structural performance. The results of these tests revealed that high levels of corrosion in rebar had a significant impact on the hysteretic behaviour of the corroded columns, notably impairing their ability to dissipate energy under cyclic loading.

Furthermore, researchers have developed a variety of empirical, analytical, and numerical models to establish relationships between corrosion levels and the corresponding reductions in load-carrying capacities (Bhargava et al., 2008; Biondini & Vergani, 2015; Coronelli, 2002). These models provide valuable insights into predicting the performance of corroded RC structures and guiding effective rehabilitation strategies.

While considerable progress has been made in understanding the individual effects of reinforcement corrosion on the structural performance of RC columns (Ou & Nguyen, 2016), particularly under steady axial compression ratios (ACR) (Y. Wang et al., 2017), the combined influence of ACR and corrosion on the seismic response of these columns has not been sufficiently studied. Existing research has largely focused on isolated factors, frequently neglecting the intricate interaction between varying levels of corrosion and axial compression under dynamic, seismic loading conditions. This oversight has created a gap in the understanding of how these combined variables affect the overall performance of RC columns during seismic events, particularly in terms of stiffness, ductility, energy dissipation, and seismic resilience.

Addressing this gap is crucial because both corrosion and axial compression ratios can significantly alter the seismic behaviour of columns. Corrosion degrades the reinforcement’s mechanical properties, reducing its capacity to carry loads and absorb seismic energy, while axial compression affects the distribution of stresses within the column during an earthquake. When combined, these factors can lead to unpredictable and potentially catastrophic failures in RC structures, especially during seismic events where the behaviour of the structure under cyclic loading is critical.

The importance of investigating these combined effects becomes even more evident when considering columns designed under different seismic design guidelines. Columns designed according to the latest seismic standards, which emphasize ductility and energy dissipation, may behave differently under the combined effects of corrosion and varying ACR levels compared to those designed prior to these guidelines, which are typically non-ductile and less capable of withstanding seismic forces. The seismic performance of these two types of columns—ductile and non-ductile—under corrosion and axial load variations has not been thoroughly explored, creating a critical need for more targeted research.

The present study aims to address this crucial knowledge gap by investigating the seismic behaviour of both ductile and non-ductile columns under varying levels of reinforcement corrosion and ACR. This in-depth analysis will provide valuable insights into the residual strength, ductility, and energy dissipation of ductile and non-ductile RC columns, enabling more accurate assessments of their seismic performance. The findings from this research will not only contribute to the development of better design practices for corrosion-affected structures but also offer essential guidance for effective retrofitting strategies. Ultimately, this study is vital for improving the safety and longevity of our infrastructure, protecting lives, and safeguarding valuable investments, particularly in seismic-prone regions.

1.2 Research Objectives

In response to the research gaps identified in the previous discussion, the present study was meticulously designed with the following key objectives to investigate the seismic behaviour of RC columns, both with and without corrosion, under varying ACRs:

1. **To develop comprehensive three-dimensional (3D) numerical models of both uncorroded and corroded large-scale ductile and non-ductile RC columns**: This objective involved creating a detailed 3D numerical model capable of simulating the behaviour of RC columns under seismic loading conditions. The model represented both uncorroded and corroded columns, considering various corrosion levels. The developed model was rigorously validated using experimental data to ensure its accuracy and reliability in predicting the structural response.
2. **To quantify and compare the seismic response of uncorroded ductile and non-ductile columns under different ACRs**: This objective entailed performing a detailed analysis of the seismic performance of uncorroded RC columns designed as ductile and non-ductile structures. By varying the ACRs, the study assessed how these factors influenced the columns' stiffness, load-carrying capacity, energy dissipation, and overall seismic resilience, providing a foundation for understanding the performance of intact columns in seismic conditions.
3. **To quantify and compare the seismic response of corroded ductile and non-ductile columns under different ACRs**: Building upon the previous objective, this part of the study explored how corrosion affected the seismic behaviour of both ductile and non-ductile RC columns. The performance of corroded columns was assessed under different ACRs, and

comparisons were made to the uncorroded columns. This allowed for a comprehensive understanding of how corrosion and varying axial compression ratios jointly influenced the seismic response, particularly with respect to stiffness degradation, loss of ductility, and load-carrying capacity.

1.3 Research Scope

1. This research comprehensively investigated the combined effect of corrosion and varying ACRs on the seismic response of both ductile and non-ductile RC columns. RC columns, as essential structural elements, bear the load of buildings and play a pivotal role in maintaining the overall stability and integrity of structures. Given their critical importance, understanding the interaction between corrosion and ACR is vital for ensuring the long-term durability, safety, and resilience of buildings. By considering these factors in real-world seismic conditions, this study aimed to fill existing knowledge gaps regarding how corrosion and ACR together influence the performance of columns during seismic events and other structural challenges, such as floods, fires, or accidental impacts.
2. To gain a comprehensive understanding of the complex interactions between corrosion and ACR on RC columns, the research involved the development and calibration of advanced 3D simulation models using ABAQUS software. These models were rigorously validated against experimental data to ensure their accuracy and reliability in predicting the columns' behaviour under various loading conditions. With a strong computational foundation, the study then conducted an extensive parametric analysis, exploring a wide range of ACR levels and corrosion severities. To simulate real-world seismic loading conditions, quasi-static cyclic lateral loading tests with progressively increasing magnitudes were employed, mimicking the seismic forces that RC columns might experience during an earthquake. This detailed simulation allowed for a deeper understanding of how these columns behave under the combined stress of corrosion and varying ACR levels, with a particular focus on key structural performance indicators.
3. A significant focus of this research was on the potential plastic hinge region of RC columns, which plays a pivotal role in the ductile performance of these structures during seismic events. The plastic hinge region is typically the first to experience significant deformations and is crucial in determining how well a column can dissipate energy and absorb seismic forces. The study delved into critical parameters such as hysteresis behaviour, backbone curves, stiffness degradation, ductility, energy dissipation, and equivalent viscous damping. These parameters are key to evaluating the overall seismic resilience of RC columns, and understanding how they are influenced by corrosion and varying ACRs is essential for accurately predicting the columns' behaviour during seismic events.

4. The findings from this research underscore the critical need to incorporate considerations of ACR and corrosion into the design, assessment, and maintenance of RC columns. This integrated approach is essential to improving the seismic performance and structural reliability of RC columns, particularly in areas subject to corrosive environments or seismic activity. By identifying the specific ways in which corrosion and varying ACR impact the performance of these columns, engineers can make better-informed decisions about their remaining strength and service life. This research provides a robust framework for improving safety, guiding maintenance strategies, and developing retrofitting solutions for structures located in seismically active or corrosive regions. The knowledge gained from this study will contribute to the optimization of design and maintenance practices, ultimately enhancing the longevity and safety of RC infrastructure

1.4 Research Significance

The significance of this study lies in its focused exploration of the combined effects of reinforcement corrosion and varying ACRs on the seismic behaviour of RC columns, which are critical structural components in buildings. While corrosion and axial load variations are individually recognized as factors that influence the structural integrity of RC columns, their combined impact on seismic performance has not been thoroughly investigated. This research aims to fill that gap, providing a deeper understanding of how corrosion and ACR influence the stiffness, ductility, energy dissipation, and overall seismic resilience of both ductile and non-ductile columns.

The findings of this study are highly significant for the design and safety of structures, as they highlight the need for a comprehensive approach in considering ACR and corrosion in the design, assessment, and maintenance of RC columns. Current seismic design codes and guidelines have largely overlooked the impact of ACR in the context of ductile detailing for columns. By quantifying and illustrating how different levels of corrosion and axial load ratios affect the seismic response, this research will provide critical insights that can be used to update existing building standards. The knowledge gained can directly inform the development of more resilient and reliable infrastructure, especially in regions prone to corrosion and seismic activity.

In essence, this study will contribute to the advancement of safer structural designs by addressing a critical knowledge gap, improving the resilience and longevity of buildings, and ultimately enhancing the safety of occupants and the overall sustainability of infrastructure.

1.5 Outline of the thesis

This thesis is meticulously structured into five comprehensive chapters, each of which systematically addresses a specific aspect of the research. The organization reflects a logical progression from the introduction and review of foundational studies to the detailed analyses and final synthesis of findings. Throughout the chapters, relevant background information, existing research, and pertinent literature are seamlessly incorporated, providing a robust framework for the study and enriching the narrative with a solid theoretical and methodological foundation. Each chapter begins with an overview and introduction that contextualizes its content within the broader scope of the thesis, ensuring clarity and coherence in the discussion.

Chapter 1: Introduction

The first chapter provides a comprehensive introduction to the research, outlining the background and context of the study. It elaborates on the critical issues addressed by the research, emphasizing the significance of understanding the combined effects of corrosion and ACRs on the seismic performance of RC columns. The objectives of the study are clearly articulated, and the significance of the work is discussed in detail, highlighting its potential to inform seismic design standards and improve the resilience of RC structures.

Chapter 2: Development and Validation of Numerical Models

This chapter details the development of 3D numerical models to simulate the seismic behaviour of RC columns. The methodology employed for model creation, calibration, and validation is extensively discussed. A systematic validation exercise is conducted by comparing the model predictions with experimental results, ensuring the reliability of the simulations. The limitations of the numerical models are also addressed, providing a transparent account of their applicability and scope.

Chapter 3: Seismic Response of Uncorroded Ductile and Non-ductile Columns

Chapter 3 presents a parametric study to evaluate the seismic response of uncorroded ductile and non-ductile RC columns under varying ACR levels. The chapter explains the methodology for calculating performance indices and presents a comparative analysis to highlight the seismic response differences between ductile and non-ductile columns. The insights gained from this analysis provide a foundational understanding of how ACR and the absence of ductility provisions influence the seismic behaviour of RC columns.

Chapter 4: Seismic Response of Corroded Ductile and Non-ductile Columns

This chapter focuses on the seismic response of ductile and non-ductile RC columns subjected to varying levels of corrosion and ACRs. Through an extensive parametric study, the findings reveal how the combination of these factors can lead to significant degradation in seismic performance, even in columns designed according to the latest seismic guidelines. The results underscore the heightened vulnerability of corroded columns under seismic loading, particularly the non-ductile columns that lack design provisions consistent with modern seismic guidelines. The study provides critical insights into the seismic risks associated with aging and inadequately designed structures, underscoring the urgency of implementing targeted retrofitting strategies to mitigate these risks.

Chapter 5: Discussions and Conclusions

The final chapter synthesizes the key findings and conclusions of the research by comparing the seismic performance of all studied specimens across various categories and combinations. A detailed discussion of performance indices and other critical parameters is presented, drawing insightful conclusions about its behaviour under combined corrosion and ACR. Furthermore, practical recommendations are offered to guide future research and engineering practices, particularly in the design, assessment, and retrofitting of RC columns in seismically active and corrosive environments. This chapter underscores the study's contributions to advancing knowledge in the field and its potential to inform safer and more resilient infrastructure designs.

Through this structured and methodical organization, the thesis provides a holistic understanding of the research topic, addressing critical gaps in the literature and offering valuable insights for academia and industry alike.

Chapter 2

Development and Validation of Numerical Model

2.1 Introduction

Modelling RC members is inherently complex due to the nonlinear behaviour of concrete and its intricate interaction with steel reinforcement. Concrete, a brittle material, exhibits distinct behaviours under tensile and compressive stresses, including cracking, crushing, and strain softening. Steel, on the other hand, behaves elastoplastically and works synergistically with concrete to resist loads. Capturing these interactions required advanced material models like the Concrete Damaged Plasticity (CDP) model for concrete and bilinear or multilinear stress-strain relationships for steel reinforcement. Furthermore, the bond-slip interaction between steel and concrete added another layer of complexity, as this relationship significantly influences the load transfer mechanism and failure patterns in RC members. Accurate representation of these factors in finite element (FE) models was achieved through meticulous calibration and validation against experimental data.

When corrosion was introduced, the modelling complexity increased exponentially. Corroded RC members experience degradation not only in material properties but also in the overall structural behaviour. Corrosion of steel reinforcement leads to a reduction in the cross-sectional area of the bars, a loss of bond strength between steel and concrete, and the development of expansive corrosion products. These expansions induce tensile stresses in the concrete cover, resulting in cracking and spalling, which further compromise the structural integrity of the member. Unlike the uniform material properties in uncorroded members, corroded members exhibit highly localized and variable properties due to nonuniform corrosion along the reinforcement length. This spatial variability made the modelling of corroded RC members significantly more challenging.

In addition to the complexities of uncorroded modelling, the simulation of corroded members included degradation mechanisms such as material models for corroded steel accounting for reductions in yield strength, ductility, and stiffness, and material models for concrete accounting for cracking due to expensive stresses.

Crushing and bond deterioration caused by corrosion must be incorporated into the model. Advanced bond modelling techniques, such as cohesive zone models and interface elements, are often required to replicate the deteriorated bond behaviour accurately. Furthermore, the interaction between corrosion-induced cracking and the nonlinear load-deformation response of the member necessitates a dynamic and iterative modelling approach.

Overall, transitioning from modelling uncorroded to corroded RC members involves addressing additional layers of complexity, including spatial variability in material degradation, the mechanical effects of corrosion products, and the influence of these factors on bond behaviour. These challenges underscore the need for comprehensive finite element modelling frameworks, validated by experimental data, to reliably simulate the behaviour of corroded RC members under various loading conditions. Such models are critical for assessing the remaining service life, safety, and performance of deteriorating RC structures and developing effective strategies for their rehabilitation.

To address these challenges, this chapter delves into a comprehensive FE modelling approach tailored to simulate the behaviour of uncorroded and corroded RC columns with a high degree of accuracy and reliability. The proposed methodology integrates advanced material models for both concrete and steel reinforcement to capture their nonlinear behaviours under varying stress conditions. For concrete, the CDP model is employed, which allows for the simulation of tensile cracking and compressive crushing, taking into account the progressive damage and stiffness degradation due to loading and corrosion. This model is crucial for replicating the brittle behaviour of concrete under tensile stresses and its ductile response under compression, both of which are significantly altered in the presence of corrosion-induced damage

For steel reinforcement, the modelling considers the effects of corrosion on mechanical properties, such as reduced yield strength, ductility, and cross-sectional area. A bilinear stress-strain relationship is used, with adjustments made to account for the reduction in load-bearing capacity due to corrosion. To simulate the interaction between steel and concrete, various bond modelling techniques are explored, including cohesive zone modelling, bond-slip relationships, and embedded element methods. These approaches are critical for capturing the degradation of the bond between steel and concrete, a key factor in the structural integrity of corroded RC members.

The chapter also highlights the importance of calibration and validation of the FE model using experimental data. Experimental studies provide valuable insights into the load-displacement behaviour, crack propagation patterns, and ultimate failure modes of uncorroded and corroded RC columns, which are used to refine the numerical model and ensure its reliability. The integration of advanced material models with experimental validation ensures that the proposed FE modelling approach can accurately predict the behaviour of corroded RC structures under real-world conditions.

By addressing these complexities and leveraging state-of-the-art modelling techniques, this chapter provides a robust framework for analyzing and understanding the structural performance of uncorroded and corroded RC columns, contributing to the development of effective strategies for their assessment, maintenance, and retrofitting.

2.2 Model Development

This research utilized ABAQUS, a widely used finite element analysis software, to develop a nonlinear FE model tailored for RC structures. The package offers practical tools for modelling the complex behaviours of RC structures, making it a suitable choice for this study.

The software allowed for the incorporation of constitutive models like the CDP model, which was helpful in capturing the nonlinear behaviour of concrete under various loading conditions, including cracking and crushing. Similarly, it provided options to model steel reinforcement, accounting for elastoplastic behaviour and interactions between steel and concrete. The ability to define boundary conditions, loading scenarios, and reinforcement configurations supports a comprehensive approach for simulating all types of RC members.

While ABAQUS is just one of several available tools for such applications, its flexibility in mesh generation, material modelling, and result interpretation aligned well with the requirements of this research. The focus was on utilizing these features to develop a practical and efficient modelling strategy that could be validated against experimental data, ensuring reliability and relevance to the study objectives.

2.2.1 Geometry Creation and Meshing

2.2.1.1 Uncorroded State

A full-scale RC column is modeled, incorporating realistic dimensions as per experimental specifications (Rajput & Sharma, 2018). The concrete is represented as a solid 3D continuum using C3D8R (8-node linear brick elements with reduced integration) elements for computational efficiency. The longitudinal and transverse reinforcements are modeled as discrete entities using T3D2 (2-node 3D truss) elements to simulate the steel bars effectively.

2.2.1.2 Corroded State

For corroded conditions, the steel reinforcement diameter is reduced according to the experimentally observed corrosion loss. Furthermore, surface irregularities are introduced in the concrete-reinforcement interface section in order to account for bond degradation.

2.2.1.3 Meshing

The concrete and steel are meshed separately, ensuring a finer mesh near the reinforcement to capture stress concentrations. A compatible mesh size is adopted to maintain the interaction accuracy while optimizing computation time.

2.2.2 Material Property Assignment

2.2.2.1 Concrete

The CDP model in ABAQUS is employed to simulate the nonlinear behaviour of concrete under compression and tension. Parameters such as dilation angle, compressive strength, tensile strength, and damage evolution are defined based on experimental data.

2.2.2.2 Reinforcement Steel

A bilinear stress-strain model is adopted for steel, incorporating strain hardening. For corroded states, the reduction in yield strength and ductility due to corrosion is included.

2.2.3 Boundary Conditions and Loading

2.2.3.1 Boundary Conditions

Fixed support conditions are applied at the base of the column to replicate the experimental setup. Symmetry and contact conditions are defined at the reinforcement-concrete interface using embedded constraints or cohesive interactions for bond behaviour.

2.2.3.2 Loading

Axial and lateral loads are applied incrementally to mimic the experimental loading protocol. A static, general step is used to ensure stability in convergence during simulation.

2.2.4 Corrosion Modelling

2.2.4.1 Steel Loss

Experimental corrosion loss data is used to define the cross-sectional reduction of rebars and the corresponding reduction in their mechanical properties.

2.2.4.2 Bond Degradation

The bond-slip relationship is modified to reflect the weakened interaction between steel and concrete due to corrosion, implemented through user-defined subroutines if needed. The following highlights the effects of corrosion on the mechanical properties of RC structures.

1. **Reduction in Bond-Slip Properties**: Corrosion weakens the bond between reinforcement and surrounding concrete, directly impacting its load transfer.

2. **Loss of Steel Cross-Sectional Area**: Reduction in the rebar diameter due to corrosion directly affects the structural capacity.
3. **Degradation in Mechanical Properties of Steel**: Corrosion impairs yield strength, ultimate strength, strain capacities, and the modulus of elasticity of reinforcement.
4. **Cracking of the Concrete Cover**: Corrosion-induced expansion of steel reinforcement results in cracks in the concrete cover, compromising structural integrity.

Hence, to ensure an accurate representation of corroded structural behaviour, the following steps were undertaken using ABAQUS software:

1. **Selection of Material Models**: Suitable concrete and steel behaviour models were selected and incorporated to capture the uncorroded Column's properties.
2. **FE Model Development for a Control Column**: An FE model was created for a reference uncorroded Column with a perfect bond condition between the reinforcement and concrete.
3. **Comparison of Bond Modelling Approaches**: Various bond modelling methods, such as the Surface-Based Mechanical Contact and Surface-Based Cohesive behaviour approach, were evaluated, and the most suitable approach showcasing accurate results was chosen.
4. **Validation Against Experimental Data**: The FE model's performance was validated using available experimental data about the structural behaviour of the column.
5. **Numerical Modelling of Columns**:
    - Uncorroded Columns: A bond modelling approach yielding load-deflection behaviour closest to the perfect bond case was applied.
    - Corroded Columns: Modifications to steel, concrete, and bond strength were implemented based on the degree of corrosion.
6. **Validation of Corroded Columns**: The FE model's accuracy was further validated against experimental results for both the ductile and non-ductile corroded columns.

2.3 Model Development of Uncorroded Ductile and Non-ductile Columns

This research utilized ABAQUS, a well-established and widely used FE software, to develop numerous nonlinear FE models. ABAQUS is highly versatile, making it ideal for modelling RC structures. Through FE modelling, the capacity of RC columns was estimated with high accuracy, offering a substantial reduction in both the time and costs typically associated with experimental testing. The primary distinction between ductile and non-ductile columns lies in the spacing of their transverse reinforcements. In ductile columns, the transverse reinforcements are spaced at 75 mm center-to-center (c/c), whereas non-ductile columns have a wider spacing of 300 mm c/c.

For modelling uncorroded ductile and non-ductile columns, 3D column-stub models were created using (Dassault Systems, 2022) and with the help of Abaqus-Standard (A/S) solver. This solver, which employs the Newton-Raphson algorithm for implicit time integration, was chosen to manage the complexity of nonlinear problems. Concrete was modeled using C3D8R elements, effectively capturing the concrete behaviour, including compression, tensile cracking, and steel yielding. The longitudinal and transverse reinforcements were represented using 2-node linear 3D truss elements (T3D2).

For the uncorroded columns, the reinforcement was modeled as being perfectly embedded into the surrounding concrete, ensuring an idealized interaction between the two materials. The analysis was conducted using the "Dynamic Explicit" method, which is particularly well-suited for addressing quasi-static problems involving complex contact conditions. This method, recognized for its numerical stability, was selected to mitigate convergence challenges, as highlighted by (Dassault Systems, 2022).

2.4 Material Modelling for Uncorroded Columns

Selecting the appropriate material models for concrete and steel ensures the accuracy of nonlinear analysis simulation results. These factors are thoroughly explained in detail in the following sections:

2.4.1 Concrete Behaviour Model

In ABAQUS, three different techniques are available for modelling the nonlinear behaviour of concrete: the Smeared Cracking (SC) model, the Concrete Damaged Plasticity (CDP) model, and the Brittle Cracking model. For this investigation, the CDP model was chosen to simulate concrete behaviour, as it combines isotropic damaged elasticity with isotropic tensile and compressive plasticity to capture the inelastic response of concrete. Initially proposed by (Lubliner. J, 1989) and further developed by (J. Lee et al., 1998). The CDP model assumes that the two primary failure mechanisms are tensile cracking and compressive crushing of the concrete. While some default parameters from (Dassault Systems, 2022) were adopted, the stress-strain relationship of concrete in compression and tension was determined experimentally for numerical calculations and validation purposes.

2.4.1.1. CDP Parameters

To set up the CDP model, several inputs are required, including Poisson’s ratio, which was assumed to be 0.3 for concrete, the elastic modulus, compressive, and tensile behaviour; additionally, defining the plastic damage in concrete necessitates five key parameters. These parameters are: dilatation angle (ψ), flow potential eccentricity (ε), the ratio of initial equibiaxial compressive yield stress to initial compressive yield stress (f_{b0}/f_{c0}), the ratio of the second stress invariant on the tensile meridian (K_c) and the viscosity parameter (μ) as clearly explained in Fig. 2.1. A dilatation angle of 37° was used, which is a typical value for concrete as suggested by (Y. Fujita & R. Ishimaru, 1994) while the remaining parameters were set to the default values recommended by ABAQUS and is further explained in Table 2. 1.

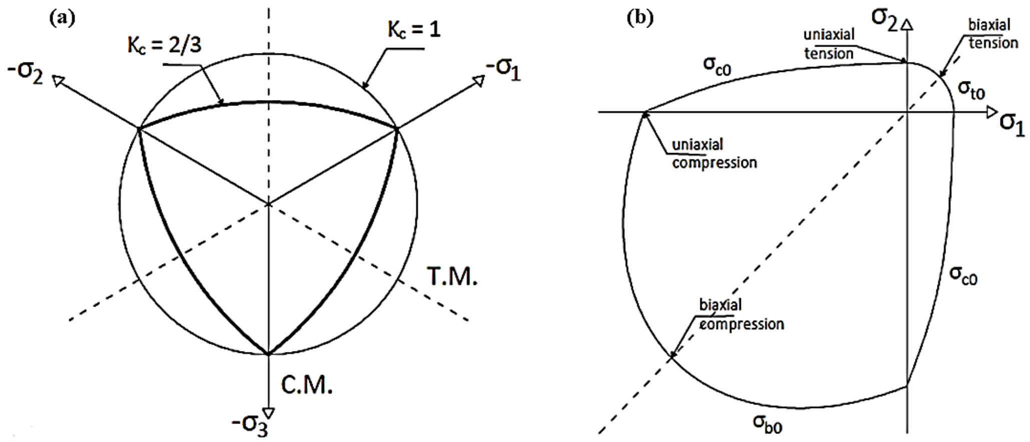

Fig 2. 1 Projection of CDP Yield Surface (a) In Deviatoric Plane (b) Into the σ_1-σ_2 plane (Abaqus, 2021)

Table 2. 1 Plastic Damage Parameters Used for Concrete Modelling

ψ	ε	f_{b0}/f_{c0}	K_c	μ
37	0.1	1.16	0.66	0

2.4.1.2. Concrete Behaviour in Compression

The CDP model requires input data for the stress-inelastic strain behaviour of concrete under both compression and tension, which are typically obtained from uniaxial compression and tension tests. In this study, the hardening and softening behaviour of concrete in compression was implemented in the FE model based on the (CEB-FIP Model code, 2010) as illustrated in Fig 2. 1 and described by equations (2.1) to (2.3). The linear portion of the compression curve was assumed to up to 0.4 of the peak compressive strength. Here, σ_c represents the compressive stress, f_{cm} is the mean compressive strength of concrete cylinders, and k and η are factors calculated using equations (2.2) and (2.3). E_{c1} is the secant modulus of elasticity, representing the slope from the origin to the peak compressive stress, while E is the elastic modulus of concrete, calculated using the standard ACI-318 equation. ε_c denotes the concrete strain, and ε_{c1} is the strain at peak stress.

$$\frac{\sigma_c}{f_{cm}} = \frac{k\eta - \eta 2}{1+\eta(k-2)} \tag{2.1}$$

$$\eta = \frac{\varepsilon_c}{\varepsilon_{c1}} \tag{2.2}$$

$$k = \frac{E}{E_{c1}} \tag{2.3}$$

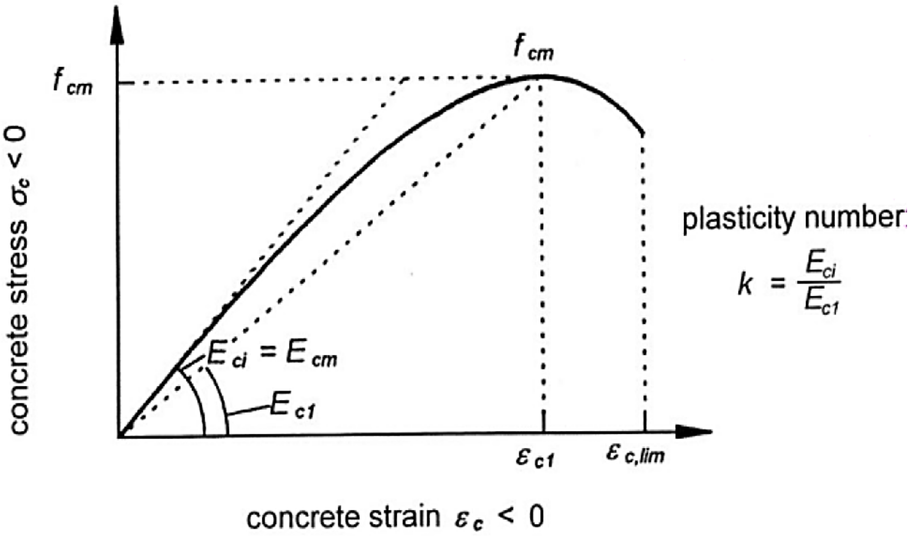

Fig 2. 2 Stress-Strain Relation for Uniaxial Compression (CEB-FIP Model Code, 2010)

2.4.1.3 Concrete Behaviour in Tension

The relationship between stress and crack width in concrete under tension was determined using Equation (2.4) by (Hordijk & Arend, 1991). To implement this relationship, the displacement control method was utilized in Abaqus, where stress-displacement variables were applied. Typically, the crack width (W_c) value, as defined in (CEB-FIP Model code, 2010) ranges from 0.1 mm to 0.3 mm. However, in this study, a higher W_c value of 0.3 mm was adopted in Equation (2.4) along with $c_1 = 3$ & $c_2 = 6.93$ to account for the tension-stiffening effect in the concrete material model.

The stress-crack width curve was based on experimental observations from standard tests such as tension tests on notched beams and direct tensile tests, as suggested in guidelines like the ACI 446R-08 (American Concrete Institute, 2008) and Eurocode 2 (CEN, 2004). These provide empirical expressions that relate the crack width to stress in the post-cracking regime. Among the various tension softening models available, a bilinear tension model was employed in this study, adhering to the (CEB-FIP Model code, 2010) for defining the stress-crack opening relationship, as depicted in Fig 2. 2. The crack opening values were converted to strain by dividing them by the characteristic length (l_c), which was assumed to be equal to the element size, following the approach of (Ou & Nguyen, 2014) Consequently, the stress value does not drop to zero at the corresponding W_c value. Additionally, the fracture energy (G_f) was calculated using Equation (2.5) to ensure consistency with the material behaviour under tensile stress as clearly explained Fig. 2.3.

$$\sigma_t = f_t \left[1 + \left(\frac{c_1 w}{w_c}\right)^3\right] e^{-c_2\frac{w}{w_c}} - \frac{w}{w_c}\ (1 + c_1^3)e^{c_2} \tag{2.4}$$

$$w_c = \frac{5.14G_f}{f_t} \tag{2.5}$$

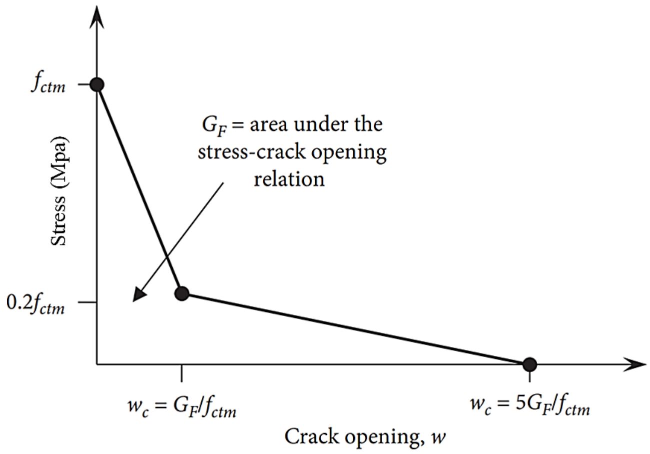

Fig 2. 3 Stress vs. Crack Opening for Uniaxial Tension (CEB-FIP Model Code, 2010)

2.4.1.4. Concrete Damage Evolution

The degradation of the elastic modulus of concrete in the adopted CDP model is characterised by calculating the concrete's damage initiation and evolution. It is analysed by observing the post-peak regime of load-deflection curves in tension and compression. The damage variable ranges from zero to one, where zero is no damage, and one is maximum. This model was proposed by (Lubliner. J, 1989) which has been utilised in this present FE analysis during CDP calculations and modelling. Equation 2.6 explain the yield damage variable (*d*) which is as follows:

$$\mathrm{d} = 1\text{-}\ \frac{\sigma}{f} \tag{2.6}$$

2.4.2 Steel Behaviour Model

The material model for steel reinforcement significantly impacts the plastic behaviour and ultimate deflection of the structure. In this study, an elastic-plastic model incorporating strain hardening was employed for the steel reinforcement of columns. Within ABAQUS, this behaviour is initially characterized by defining the elastic properties through the modulus of elasticity (Es = 200,000 N/mm²) and Poisson's ratio (ν = 0.3). Subsequently, the plastic behaviour is modeled by inputting tabulated data of true stress versus plastic strain.

To accurately predict the ultimate deflection of a RC Column, the stress-strain curve beyond the ultimate stress is represented by a gradual decline in stress. If experimental data for the stress-strain curve of uncorroded steel bars is unavailable, the curve can be approximated using (Mander et al., 1988) steel stress-strain model. Since ABAQUS requires true stress-strain input, conversion from nominal stress-strain values was performed using Equation (2.7) and Equation (2.8).

$$\sigma_{\mathrm{true}} = \sigma(1+\varepsilon) \tag{2.7}$$

$$\varepsilon_{\mathrm{true}} = \sigma(1+\varepsilon) \tag{2.8}$$

2.4.3 Concrete-Steel Interface Model

This study utilized uncorroded (control) and corroded specimens, with separate bond modelling techniques adopted for each type. For FE modelling of the uncorroded specimens, a perfect concrete-rebar bond condition was assumed, leading to highly accurate results. In contrast, a bond degradation model was implemented for the corroded specimens to account for the effects of corrosion. Furthermore, this research also explores the various surface interaction techniques available in ABAQUS to simulate the bond behaviour for both corroded and uncorroded specimens.

Since the influential study by (Eligehausen et al., 1983) introduced a segmental bond-slip model (relating shear stress at the interface to bar slip) based on extensive testing of various parameters, subsequent researchers have focused on further refining this model (Y.F. Wu & Zhao, 2013). Eligehausen's model has become a foundational basis for bond-slip behaviour, as illustrated in Fig 2.4 (a). In this research, the bond-slip model from (CEB-FIP Model code, 2010) was adopted, along with the traction-separation behaviour proposed by (Henriques et al., 2013) for modelling all the specimens.

Various FEA methods were utilised by numerous researchers in various literature to simulate the concrete-steel bond which are explained as follows:

1. The first approach for modelling bond behaviour involves using interface or spring elements to transfer stress between steel and concrete. One advantage of this method is its compatibility with 2D modelling, where steel rebars are represented by two-node truss elements, and the spring element's nonlinearity is captured through the load-displacement relationship. However, this method is time-consuming and inefficient for modelling large 3D structures. Nevertheless, researchers such as (Xiaoming & Hongqiang, 2012) (Val & Chernin, 2009) and (Murcia-Delso & Benson Shing, 2015) have successfully employed spring interface and four-node interface elements for bond modelling in ABAQUS.

2. The second approach modifies the properties of either concrete or steel elements to simulate bond effects. For instance, (Ziari & Kianoush, 2014) altered the material properties of a small concrete region, known as the Bond Zone, in contact with the reinforcing bar to better capture bond interaction. In this zone, fracture energy and tensile strength were reduced.

3. The third approach models bond as an interaction between two 3D surfaces, which can be implemented in various ways in ABAQUS for both concrete and steel elements. (Amleh & Ghosh, 2006) used this method in finite element pullout tests for both corroded and uncorroded

specimens, utilizing mechanical contact properties in ABAQUS to describe tangential and normal behaviour between the contacting surfaces of concrete and steel.

In this study, surface-based interaction methods (option 3) were employed for bond modelling, using two main approaches which are available in ABAQUS. The first is surface-based mechanical contact, and the second is surface-based cohesive behaviour which is a mechanical model based on traction-separation behaviour. The cohesive behaviour allows the bond between surfaces to be described by a linear elastic relationship between traction (t) and separation (δ) as illustrated in Fig 2. 4(b). Both approaches—mechanical contact and cohesive behaviour—were explored to simulate bond behaviour in uncorroded RC Columns. The method that produced the best validation results was subsequently applied to the corroded columns. These surface-based approaches are further explained as follows:

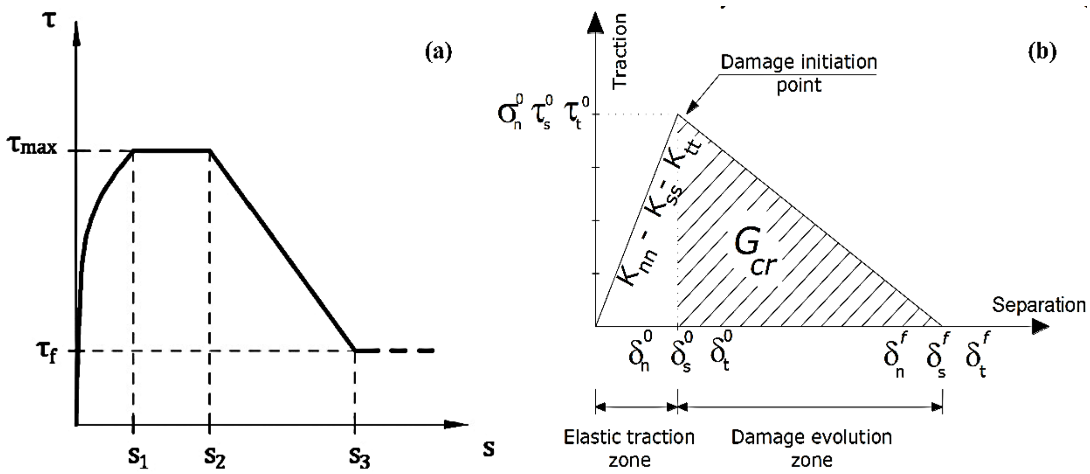

Fig 2. 4 (a)Bond–Slip Model in (CEB-FIP Model code, 2010); (b) Traction–Separation Behaviour in ABAQUS (Henriques et al., 2013)

2.4.3.1 *Approach One: Surface-Based Mechanical Contact*

In this approach, the contact behaviour (Contact property) is defined in two directions: the normal direction and the tangential direction relative to the contacting surfaces. The normal behaviour is characterized by a pressure-overclosure relationship, where the gap between the two surfaces relatively becomes zero. This is referred to as "hard" contact, the default pressure-overclosure method in ABAQUS. However, for the tangential behaviour, both shear stress and normal stress are transmitted across the contact surfaces. As a result, frictional forces resisting the relative slip between the surfaces must be considered. Given the complexity of modelling perfect friction, a penalty friction formulation was calculated in most cases.

ABAQUS uses a pure master-slave contact system, where the nodes of the slave surface cannot penetrate the master surface. In RC simulations, the rebar typically serves as the slave surface, and the concrete as the master surface (Amleh & Ghosh, 2006). The mechanical contact approach can be further refined by inputting specific properties, such as friction and pressure, for both the normal and tangential directions.

2.4.3.2 Approach Two: Surface-Based Cohesive Behaviour

The surface-based cohesive behaviour in ABAQUS is a mechanical modelling method based on traction-separation behaviour. It describes the bond between two surfaces as a linear elastic relationship between traction (t) (bond stress) and separation (δ) (slip) as explained in Fig 2. 4 (b). ABAQUS offers two main methods for simulating bonded interface behaviour using traction-separation models: cohesive elements and surface-based cohesive behaviour with negligible thickness. In this research, the surface-based cohesive method was chosen because of its convenience and effectiveness. (Henriques et al., 2013) applied this method in 3D Column modelling, though without considering bond loss.

In ABAQUS, the traction-separation model consists of two phases: the first represents linear elastic behaviour, and the second highlights the plastic phases which relates to bond initiation and evolution damage phases. The elastic behaviour is defined by an elastic constitutive matrix that relates the shear and normal stresses to their corresponding separations across the interface (Dassault Systems, 2022). The elastic behaviour can be either uncoupled or coupled, as shown in Equation 2.9 and Equation 2.10, respectively.

$$T = \begin{pmatrix} t_n \\ t_s \\ t_t \end{pmatrix} = \begin{pmatrix} k_{nn} & 0 & 0 \\ 0 & k_{ss} & 0 \\ 0 & 0 & k_{tt} \end{pmatrix} \begin{pmatrix} \delta_n \\ \delta_s \\ \delta_t \end{pmatrix} = \mathrm{K}\delta \tag{2.9}$$

$$T = \begin{pmatrix} t_n \\ t_s \\ t_t \end{pmatrix} = \begin{pmatrix} k_{nn} & k_{nn} & k_{nn} \\ k_{nn} & k_{ss} & k_{nn} \\ k_{nn} & k_{nn} & k_{tt} \end{pmatrix} \begin{pmatrix} \delta_n \\ \delta_s \\ \delta_t \end{pmatrix} = \mathrm{K}\delta \tag{2.10}$$

Where t_n, t_s and t_t = nominal stresses in normal, shear and tangential directions, δn, δs and δt are the displacements in normal, shear and tangential directions, respectively and K_{ij} represents the stiffness coefficients.

For this research, the uncoupled approach was used, following the recommendations of several researchers. This required defining only the terms K_{nn}, K_{ss}, and K_{tt}, which represent bond stiffness. The challenge of this elastic model lies in estimating appropriate values for the K matrix that accurately reflect the steel-concrete bond. The unit of these constants in the K matrix is [Force/Length²/Length], representing bond stiffness. The second phase of the cohesive behaviour involves the initiation and evolution of bond damage. Damage refers to the point at which the interface stops behaving elastically. To characterize damage initiation, the bond-slip relationship is approximated using a bond damage criterion, where damage begins when any of the three normal stresses (t_n, t_s, and t_t) exceeds a maximum allowable value. To ensure that the stress primarily governs the behaviour, a large value is assigned to the normal stress (t_n). In ABAQUS, the maximum bond strength (τ_{max}) is represented by t_s, while t_t has minimal impact because the transverse stress is found to be negligible. Furthermore, Damage evolution follows a linear response, where the bond is fully degraded at maximum effective separation (δ_m). In this study, δ_m was defined as the maximum slip in the longitudinal tangential direction (δ_s), as slip in the other two directions is minimal. This linear damage evolution was chosen for its simplicity and sufficient accuracy.

2.5 Model Development of Corroded Ductile and Non-ductile Columns

The development of models for corroded ductile and non-ductile columns began by constructing both column types using the same procedure outlined in Sections 2.2 and 2.3. However, these initial models were later modified to account for corrosion-induced damage by incorporating empirical reduction models from the literature into the simulation. This damage leads to a significant reduction, which is addressed in this study and described as follows:

1. A decrease in concrete strength within the cover region
2. Reduction in rebar cross-sectional area, yield strength, and modulus of elasticity
3. Degradation of bond strength.

The corroded rebars and concrete are connected to each other using a surface-based cohesive behaviour technique. As per varying corrosion, the concrete-steel bond strength reduction is calculated separately for different levels of corrosion. These calculated values are then used into the simulation model accordingly.

The modified FE models provide valuable insights into the local behaviour of corroded RC Columns, such as variations in spalling stress and bond stress. To accurately capture the bond strength degradation, the effect of concrete spalling was incorporated into the analysis. An outward normal pressure was applied at the concrete surface near the rebar-concrete interface. Incorporating all these techniques resulted in modelling the corroded structures for reliable and precise results.

2.6 Material Modelling for Corroded Columns

The selection of appropriate material models for degraded concrete and corroded steel is crucial to ensuring the accuracy of nonlinear analysis simulations. The subsequent subsections describe the methods employed to incorporate corrosion-induced damage in ABAQUS, thereby ensuring a comprehensive representation of these effects in the analysis.

2.6.1 Reduction of Concrete Strength in the Cover Region

Corrosion in steel reinforcement leads to cracking of the concrete cover near the affected bar, which significantly influences the overall behaviour of the specimen, particularly in the compression zone. The most widely adopted model to account for this effect was introduced by (Coronelli & Gambarova, 2004). They demonstrated that corrosion-induced rust results in volume expansion, creating splitting stresses within the concrete that can lead to cracking of the surrounding cover. In areas with high confinement, the concrete may crack, but the uncracked portions between these cracks still contribute to the Column's stiffness and load-bearing capacity. To account for this degradation, the Equation 2.11 was proposed to reduce the strength of cracked concrete in the compression zone due to corrosion.

$$\mathrm{f_{cc}} = \frac{\mathrm{f_c}}{1+\mathrm{k}\frac{\varepsilon 1}{\varepsilon c}} \tag{2.11}$$

Where, f_c = maximum compressive strength of uncorroded concrete, k = parameter that relies on diameter and roughness of reinforcement, taken as 0.1 based (Coronelli & Gambarova, 2004), ε_c = concrete strain at peak load, ε_1 = average tensile strain in cracked concrete which is normal to the direction of applied compression.

The value of ε_1 is correlated with the width of concrete cracks caused by corrosion. It is affected by two primary factors: the amount of corroded reinforcement bars and the severity of the corrosion in terms of depth, as well as the ratio of volumetric expansion of the corroded steel.

$$\varepsilon_1 = \frac{(b_f - b_o)}{b_o} \tag{2.12}$$

where: b_f is the member width increased by corrosion cracking, and b_o is the undamaged member section width. The increase in Column width (b_f - b_o), can be approximated as:

$$(b_f - b_o) = n_{bar}\, \mathrm{W}_{cr} \tag{2.13}$$

W_{cr} can be estimated by using the crack width proposed by (Molina et al. 1993):

$$\Sigma w_{cr} = 2\pi\, (v_{r/s} - 1)\, P_r T \tag{2.14}$$

where n_{bar} is the amount of rebars in compression zone, w_{cr} is the crack width for a given corrosion penetration P_rT, T = time corrosion period. $v_{r/s}$ is the ratio of volumetric expansion of the oxides with respect to the virgin material. From the previous FE corroded concrete modelled structures, the value of vr/s was taken as 2.0 and the same was chosen for this study.

This study adopts the stress-crack opening model proposed by (Hordijk & Arend, 1991) to explain the experimental peak tensile strength and fracture energy of concrete. The effect of corrosion on the tensile strength of the concrete cover is incorporated based on the methodology outlined in (Zandi Hanjari et al., 2011). Specifically, Equation 2.15 describes a proportional reduction in the tensile strength of concrete (f_{tt}) corresponding to the reduction in compressive concrete strength.

$$f_{tt} = \frac{f_{cc}}{f_c} \times f_t \tag{2.15}$$

Where, f_{cc} = Reduced compressive strength, f_c = maximum compressive strength of uncorroded concrete,

f_t = maximum tensile strength of uncorroded concrete.

2.6.1.1. Modelling of Spalling Stresses on Concrete Cover

Rust, also known as corrosion by-products, forms as a result of rebar corrosion. The volume of these by-products expands, generating outward pressure around the entire structure. This volume increase in the corroded reinforcement is typically assumed to be twice that of the original steel volume (El Maaddawy & Soudki, 2007). Due to its close proximity to the rust, the concrete cover becomes highly susceptible to these forces, often leading to spalling. The calculation of concrete cover spalling is provided in the Eqns. 2.16 to 2.18.

$$P_{cor} = \frac{m\, E_{ef}\, D}{90.9\,(1+\vartheta+\psi)\,(D+2\delta 0)} - \frac{2\delta 0\, E_{ef}}{(1+\vartheta+\psi)\,(D+2\delta 0)} \tag{2.16}$$

$$\psi = \frac{(D+2\delta 0)2}{2C\,[C+(D+2\delta 0)]} \tag{2.17}$$

$$E_{ef} = \frac{E}{1+\theta} \tag{2.18}$$

Where, P_{cor}= radial pressure caused by corrosion, m= Corrosion percentage, E_{ef} = Effective elastic modulus (MPa), D = diameter of steel reinforcing bar (mm), ϑ = Poisson's ratio, δ_0= Thickness of porous zone i.e., 0.001 (mm), C = clear concrete cover (mm), ψ = factor depends on D, C and δ_0

Once the spalling stress is evaluated, it is applied to the reinforcement bars by selecting the relevant bars and applying an outward pressure, effectively simulating the spalling pressure on the concrete for more accurate results.

2.6.2 Reduction in Rebars Properties

It is widely recognized that corrosion leads to a reduction in the cross-sectional area of reinforcing steel bars, but this reduction is not uniform along the length of the bar. The average reduction in cross-sectional area corresponds to the amount of mass loss (X_p) in the same bar. Therefore, the average reduced cross-sectional area after corrosion can be described by Equation 2. 19. According to the literature, as corrosion progresses, the residual yield (F_{yc}) and ultimate (F_{uc}) forces of the reinforcement decrease more rapidly than the average cross-sectional area (A_s), resulting in a reduction in yield stress (f_y) alongside the decrease in area (Clark et al., 2005). This reduction is primarily attributed to pitting corrosion, a localized form of corrosion that leads to the formation of small, deep pits on the surface of the reinforcing steel. This phenomenon has been detailed by (Ou & Nguyen, 2014) and is mathematically represented in Equation 2.20.

$$A_s = (1-0.01X_p)\, A_{s0} \quad (2.19)$$

$$f_y = \frac{F_{yc}}{A_s} \text{ (with corrosion)} < f_y = \frac{F_{y0}}{A_{s0}} \text{ (no corrosion)} \quad (2.20)$$

The inclusion of pitting corrosion on the reinforcement bars introduced highly non-linear geometries, which significantly complicated the analysis and resulted in convergence issues. Pitting corrosion, characterized by localized and irregular material loss, posed challenges in achieving stable numerical solutions due to the complex stress concentrations and geometric irregularities it creates. To address these challenges and ensure computational efficiency, a simplified approach was adopted by applying uniform corrosion to the reinforcement bars. This approach assumes an even reduction in the cross-sectional area of the reinforcement, providing a more manageable representation of corrosion effects while maintaining the overall accuracy of the simulation results.

The corroded steel bars, subjected to varying levels of corrosion, are extracted from the specimens to perform a gravimetric test, which determines their percentage of corrosion. This method involves measuring the mass loss of the corroded steel bars, providing a quantitative assessment of corrosion levels. Notably, most studies indicate that accelerated corrosion processes typically result in more uniform section loss compared to the non-uniform corrosion patterns observed under natural service conditions.

The recorded mass loss values for each specimen are used to compute the corresponding corrosion percentages. These percentages serve as a basis for calculating the reduced mechanical properties of corroded steel, such as its yield strength, tensile strength, and modulus of elasticity. This approach enables the estimation of the degraded material characteristics of reinforcement bars at various corrosion levels. These reduced properties are subsequently incorporated into the finite element model by simulating the corroded rebar as 3D elements, ensuring that the analysis captures the actual behaviour of the corroded steel accurately. To support this modelling approach (Cairns et al., 2005) proposed equations that allow the modification of steel properties based on the degree of corrosion.

$$f_{yc} = (1.0 - \alpha_y \cdot Q_{corr})\, f_{y0} \quad (2.21)$$

$$f_{uc} = (1.0 - \alpha_u \cdot Q_{corr})\, f_{u0} \quad (2.22)$$

$$\varepsilon_u = (1.0 - \alpha_1 \cdot Q_{corr})\, \varepsilon_0 \tag{2.23}$$

Where f_{uc}, f_{yc} are ultimate and yield stress based on the original cross-section, and εu is the ultimate strain, $f y0$, $f u0$, and $\varepsilon 0$ represent the initial values of yield strength, ultimate strength, and ultimate elongation, respectively. Q_{corr} represents the average section loss expressed as percentage of original section (which is the same as mass loss percent X_p). α_y, α_u and α_1 are denoted as the empirical parameters.

Table 2. 2 Empirical Coefficients for Strength Reduction of Reinforcement (Cairns et al., 2005)

Authors		Exposure	Q_{corr} %	α_y	α_u	α_1
Palsson and Mirza[4]	Concrete	Service, chlorides	0 to 80*	0.0	0.0	NS
Castel, Francois, and Airliguie[7]	Concrete	Chlorides, 0.0 mA/cm^2	0 to 20	0.0	NS	0.035
Du[8]	Bare	Accelerated, 0.5 to 2.0 mA/cm^2	0 to 25	0.014	0.014	0.029
	Concrete	Accelerated, 1.0 mA/cm^2	0 to 18	0.015	0.015	0.039
Maslehuddin et al.[9]	Bare	Service, marine	0 to 1	0	0	0
Allam et al.[10]	Bare	Service Arabian coast	0 to 1	0	0	0
Morinaga[11]	Concrete	Service, chlorides	0 to 25	0.017	0.018	0.06
Zhang, Lu, and Li[12]	Concrete	Service, carbonation	0 to 67	0.01	0.01	0
Andrade et al.[13]	Bare	Accelerated, 1.0 mA/cm^2	0 to 11	0.015	0.013	0.017
Clark and Saifullah[14]	Concrete	Accelerated, 0.5 mA/cm^2	0 to 28	0.013, 0.012	0.017, 0.014	NS
Lee, Tomosawa, and Noguchi[15]	Concrete	Accelerated, 13.0 mA/cm^2	0 to 25	0.012	NS	NS
Present study	Concrete	Accelerated, 0.01 to 0.05 mA/cm^2	0 to 3	0.012	0.011	0.03

From Table 2. 2, the values of α_y and α_u are calculated which ranges from 0 to 0.015 while the value of α_1 ranges from 0 to 0.0035 (Cairns et al., 2005). Hence, in this FE model, this approach was employed to calculate the reduced values at varying levels of corrosion. By investigating various previous research works, the α_y and α_u values are taken as 0.011 and 0.007, respectively. Hence, final equations used to calculate the strength and elasticity reduction of rebars are as follows:

$$F_{yc} = (1 - 0.011 X_p) F_y \tag{2.24}$$

$$E_{sc} = (1 - 0.007 X_p) E_s \tag{2.25}$$

Where F_{yc} is reduced yield strength, and E_{sc} explains the reduced secant modulus of elasticity and X_p the percentage of corrosion.

2.6.3 Concrete-Steel Bond Degradation Model:

The use of a perfect bond interaction is inadequate for modelling RC Columns with corroded steel bars, as corrosion significantly affects the bond between reinforcement and concrete. To accurately capture the bond behaviour in corroded bars, 3D surface interaction techniques available in ABAQUS were employed. A cohesive surface bonding method was adopted to simulate the bond between the corroded steel reinforcement and surrounding. This approach utilizes a surface-based cohesive behaviour which models the linear elastic relationship between the two surfaces and is considered both effective and efficient (Al-Osta et al., 2018; Amini & Rajput, 2022). Furthermore, a traction-separation behaviour was also adopted to model the initial linear elastic behaviour followed by a post-elastic behaviour, where bond degradation initiates and evolves.

The relationship between bond stress and slip in corroded steel bars can be used to model the post-elastic behaviour, marked by the initiation and progression of bond degradation. Bond damage is triggered when the stresses exceed a specified maximum allowable limit. This stress value serves as a key factor in approximating the bond-slip relationship. In this study, parameters were carefully defined to accurately capture the bond-slip behaviour between the two 3D surfaces. The shear and normal stiffness components were estimated using the equations provided, and these values were incorporated into the simulation to ensure accurate results.

$$K_{ss} = K_{tt} = \tau_{max} / S_{max} \tag{2.26}$$

$$K_{nn} = 100K_{tt} \tag{2.27}$$

Where K_{nn}, K_{ss} and K_{tt} represent the stiffness coefficients in normal, shear and tangential directions respectively. τ_{max} represents the maximum bond strength of corroded rebars, and S_{max} is the slip corresponding to maximum bond stress.

As noted by (Gan, 2000), the stiffness coefficient K_{nn} is substantially greater than the corresponding in the shear and tangential directions, as outlined in Equation 2.27. The maximum bond strength (τ_{max}) proposed by (El Maaddawy & Soudki, 2007) can be applied to determine the (τ_{max}) or both corroded and uncorroded reinforcement bars in reinforced concrete (RC) elements. The Equation (2.28) consists of two key components: the first accounts for the influence of the concrete, while the second addresses the effect of shear stirrups.

$$\tau_{max} = R\ (0.55 + 0.24\ \frac{C_c}{d_b})\ \sqrt{f_c} + 0.191\frac{A_t f_{yt}}{S_s\ d_b} \tag{2.28}$$

Where, R defines the reduction factor due to bond loss, Cc explains the smaller of one-half of precise spacing between the clear concrete cover and rebars, d_b shows the diameter of anchored steel bars. F_c is the concrete compressive strength. Ss is spacing between shear stirrups. A_t is the cross-sectional area of stirrups within S_s and f_{yt} is yielding stress of stirrups.

The maximum slip at maximum bond stress (S_{max}) and the bond strength in well-confined concrete (τ_1) can be computed using Equation 2.29 and Equation 2.30, as proposed by (Kallias & Imran Rafiq, 2010).

$$S_{max} = 0.15C_o \frac{10}{3} \ln\left(\frac{\tau_{max}}{\tau 1}\right) + S_o \ln\left(\frac{\tau 1}{\tau_{max}}\right) \tag{2.29}$$

$$\tau_1 = 2.57\sqrt{f_c} \tag{2.30}$$

Where C_0 is the rib spacing of the reinforcing bars, and the value of S_0 is equal to 0.15 and 0.4 mm for plain and steel-confined concrete, respectively.

During the modelling of corroded bars, the calculation of τ_{max} involves a reduction factor R, which explains the reduction in bond strength with varying corrosion percentage (Maaddawy et al., 2005) as explained in Equation 2.31 and in Table 2. 3.

$$R = [A_1 + A_2X_p] \tag{2.31}$$

Where, A_1 and A_2 represent fixed parameters that are contingent upon corrosion current density employed during accelerated corrosion procedure. X_p denotes percentage of mass reduction observed in the RC bars.

Table 2. 3 A_1 and A_2 for Computation of Bond Reduction Factor (Maaddawy et al., 2005)

Current density, μA/cm²	A1	A2
40	1.003	-0.037
90	1.104	-0.024
50	1.152	-0.021
250	1.163	-0.011
500	0.953	-0.014
1000	0.861	-0.014
2000	0.677	-0.009
4000	0.551	-0.01

In conclusion, a concrete-steel bond degradation model was developed using the formulas presented, providing a robust framework for simulating the effects of corrosion on the bond between corroded steel bars and concrete. The use of cohesive surface bonding and traction-separation behaviour allowed for an accurate representation of the bond-slip relationship and the initiation of bond degradation under corrosion. By incorporating carefully defined parameters and stiffness coefficients, the model effectively captured bond strength reduction and the progression of bond damage. This approach ensures precise simulation results, enhancing the reliability of structural analyses for corroded reinforced concrete elements.

2.7 Meshing and Convergence Analysis

The foundation of any FE numerical analysis lies in discretizing the model into a network of elements. A mesh, consisting of interconnected lines and nodes, is used to numerically solve problems under external loads, allowing for accurate calculation of internal forces such as axial, shear, and bending forces. The accuracy of these calculations depends on the number of nodes and the degrees of freedom at each node. The continuum medium can be discretized into various element types, including 1D, 2D, and 3D finite element models. In this study, a 3D FE model was developed to capture the detailed behaviour of corroded RC columns, as shown in Fig 2. 5 (a).

The concrete column is discretized using C3D8R elements, an 8-node linear brick element with a single integration point. The steel reinforcement is modeled with T3D2 2-node linear 3D truss elements Fig. 2.5 (b). To balance mesh size and simulation time, A mesh sensitivity analysis was performed using cubic element sizes of 50 × 50 mm, 75 × 75 mm, and 100 × 100 mm. As expected, smaller element sizes (50 × 50 mm and 75 × 75 mm) increased computational time, but the cracking behaviour due to steel corrosion showed minimal variation across different meshes. The load-deflection results indicated negligible dependence on mesh size, leading to adopting a uniform 100 × 100 mm element size for optimal simulation efficiency.

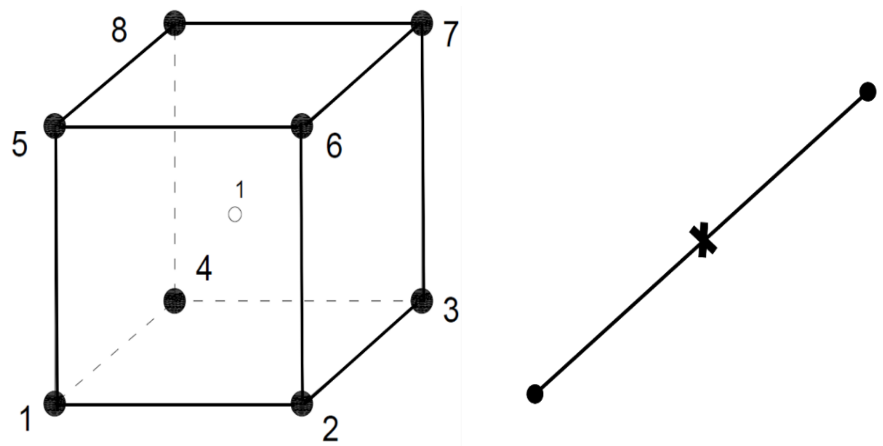

Fig 2. 5 (a) C3D8R Hexahedral Element, (b) T3D2 Element

2.8 Validation of Numerical Models

2.8.1 Summary of Experimental Study Employed for Validation

The experimental study adopted for validation involved seven full-scale RC columns, each with a height of 1800 mm and a cross-sectional dimension of 300 x 300 mm. Among these, four columns were cast as ductile specimens with varying corrosion levels of 0%, 10%, 15%, and 20% incorporating both peripheral and diamond-shaped transverse reinforcement spaced at 75 mm c/c, yielding a reinforcement ratio of 1.31%. The remaining three columns were non-ductile specimens constructed with corrosion levels of 0%, 15% and 30%. These are reinforced with peripheral stirrups spaced at 300 mm c/c, resulting in a lower reinforcement ratio of 0.33%.

To replicate structural discontinuities, such as joints or footings, and to account for flexural, shear, and axial force transfer from the column, a stub with dimensions of 1000 × 520 × 600 mm was cast alongside each specimen. A 40 mm protective concrete cover was applied to enhance the durability. All columns were reinforced with uniform longitudinal bars (#8, Ø16 mm) and cast using M30-grade concrete in accordance with (Bureau of Indian Standard, 2019). Lateral reinforcement (Ø10 mm) was varied along an 800 mm test length from the stub face. To prevent localized failures due to stress concentrations, the upper 1000 mm of each column was wrapped with two layers of glass fiber-reinforced polymer (GFRP), leaving the lower 800 mm as the designated plastic hinge zone for testing. This reinforcement strategy ensured stability during seismic testing.

The experimental phase began by applying quasi-static lateral displacement loading, which increased incrementally, in conjunction with a constant axial compression load of $0.35P_o$ (941 kN). The lateral load (V) was monitored using a ±500 kN load cell connected to the actuator, while the lateral displacement (δ) at the loading point was measured with high-precision LVDTs.

A slit-and-blade system was developed to facilitate through-bars along the 800 mm test length from the stub-column interface, representing potential hinge zones for testing corroded ductile and non-ductile specimens. Moisture within the hinge region was maintained up to 600 mm to simulate rising dampness while limiting its effect to a maximum of 750 mm. Through-rods were incorporated to secure LVDTs, enabling the measurement of flexural rotation and shear distortion. Additionally, strain gauges were installed on the reinforcement at critical locations to record strain responses during testing.

Corrosion was induced only in the plastic hinge region i.e., 800 mm, of the columns using an accelerated current-based setup with a current density of 200 $\mu A/cm^2$. The specimens were dismantled after achieving the desired level of corrosion. However, prior to the preparation of the reinforcement cage, all stirrups within the potential hinge region were weighed to record their initial uncorroded weights. For the longitudinal bars, which extend from stub to the full column length, approximate weights were determined by weighing an 800mm segment of similar rebar (i.e., 16mm diameter). The corrosion percentage was estimated by calculating the weight loss due to corrosion in relation to the original uncorroded weight. A gravimetric test was used where all longitudinal rebars and stirrups were washed with muriatic acid to remove rust, and their residual weight was compared with the weight of non-corroded rebars of the same length and dimensions. After testing and demolishing the corroded specimens, all eight longitudinal bars from the potential hinge region were extracted and weighed to determine their corrosion percentage.

2.8.2 Validation of Numerical Model for Uncorroded Ductile and Non-Ductile Columns

Based on the experimental results, the validation of uncorroded ductile and non-ductile columns was conducted. Three-dimensional numerical models for both column types were developed using ABAQUS, as depicted in Fig. 2.6 (a) and (b), respectively. The models include intricate details such as reinforcement configurations, loading scenarios, boundary conditions, and meshing strategies. This information is crucial as it directly influences the mechanical properties and performance characteristics of the columns, particularly their strength, ductility, and overall resilience under seismic or other dynamic loads. Additionally, the loading scenarios depicted in Fig 2. 6 (a) and (b) elucidate the forces and moments applied to the columns during the simulation processes. The boundary conditions outlined in these models are essential for defining the interaction between the columns and their supports or adjoining structural elements. Properly established boundary conditions ensure that the simulations reflect realistic constraints and support conditions, which significantly impact the structural response and failure mechanisms of the columns. These models are designed to replicate real-world conditions, including static and dynamic loading, to assess the column's responses to real seismic conditions accurately.

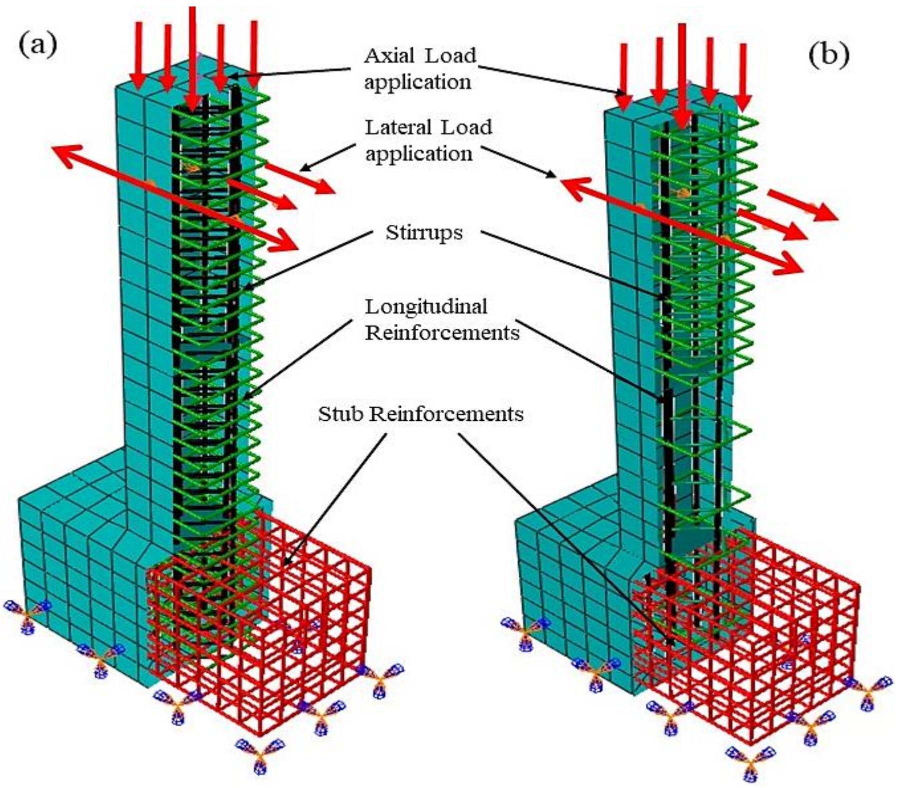

Fig 2. 6 Schematics of 3D numerical models (a) Ductile column (b) Non-ductile Column

Furthermore, the comparison of hysteresis responses between ductile and non-ductile columns, as recorded during both experimental testing and numerical modelling, is depicted Fig 2. 7 (a) and (b), respectively. Hysteresis response refers to the behaviour of materials and structures under cyclic loading conditions, where the relationship between applied load and resultant displacement is characterized by energy dissipation during loading and unloading cycles. In Fig 2.7 (a), the experimental and numerical hysteresis curves for the ductile columns are presented, highlighting their capacity to absorb and dissipate energy through inelastic deformation mechanisms. These columns, designed with higher ductility, exhibit a pronounced ability to undergo large deformations while maintaining structural integrity, which is crucial for their performance during seismic events.

Conversely, Fig 2. 7 (b) illustrates the experimental and numerical modelling results for the non-ductile columns, which are typically characterized by a brittle response under similar loading conditions. The hysteresis curves for non-ductile columns reveal a distinct behaviour, with limited energy dissipation and a more abrupt loss of load-carrying capacity once peak strength is reached. By comparing the experimental data with the numerical modelling results in Fig. 2.7 (a) and (b) significant insights can be gained regarding the effectiveness of the modelling approach used in this study. The close alignment between the experimental and numerical hysteresis responses for ductile and non-ductile columns suggests that the numerical model accurately captures the complex interactions and non-linear behaviours exhibited by these structures.

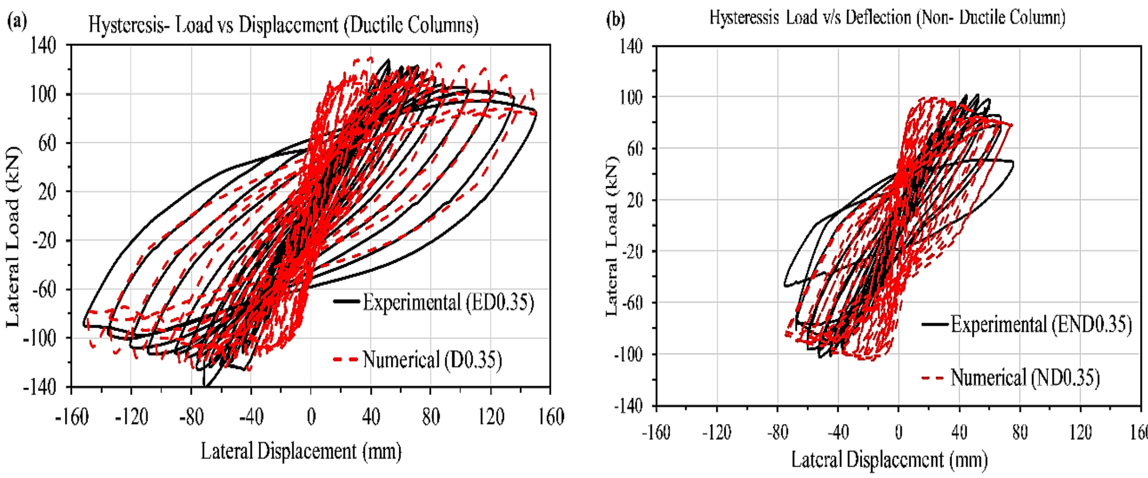

(a) Ductile Column　　　　(b) Non- Ductile Column

Fig 2. 7 Hysteresis Response Comparison of Experimental Results and Numerical Models

Moreover, Fig. 2.8 (a) and (b) present a comparative analysis of the envelope curves derived from the hysteresis responses of both ductile and non-ductile columns. These curves are essential for visualizing the overall performance of columns, as they summarize the maximum load-carrying capacity and the associated displacements throughout the loading cycles. Notably, the numerical model exhibits a strong correlation with the experimental results, thereby validating its accuracy and reliability in predicting the structural behaviour of the columns.

It is observed that in Fig. 2. 8 (a) and (b), the initial stiffness predicted by the numerical model was greater than that observed in the experimental setups. This discrepancy can be attributed to the lack of adequate fixity at the base during the initial phases of experimentation. Consequently, a slight rotation at the base occurred during the early cycles of lateral load application, which led to a reduction in stiffness. However, after a few initial cycles of loading, the column sustained some damage and became fully engaged, which resulted in a more stable and consistent response.

Notably, after reaching a 2.5% drift level, the stiffness of both the experimental and numerical models converged and followed a similar trajectory, indicating that the numerical model had successfully captured the evolving behaviour of the columns as they transitioned from an initial elastic response to a post-peak behaviour. In subsequent tests, the issue of base fixity was addressed, enhancing the reliability of the experimental results. Additionally, dial gauges were employed to monitor base displacement accurately, and the negligible readings obtained from these gauges confirmed that adequate fixity had been achieved.

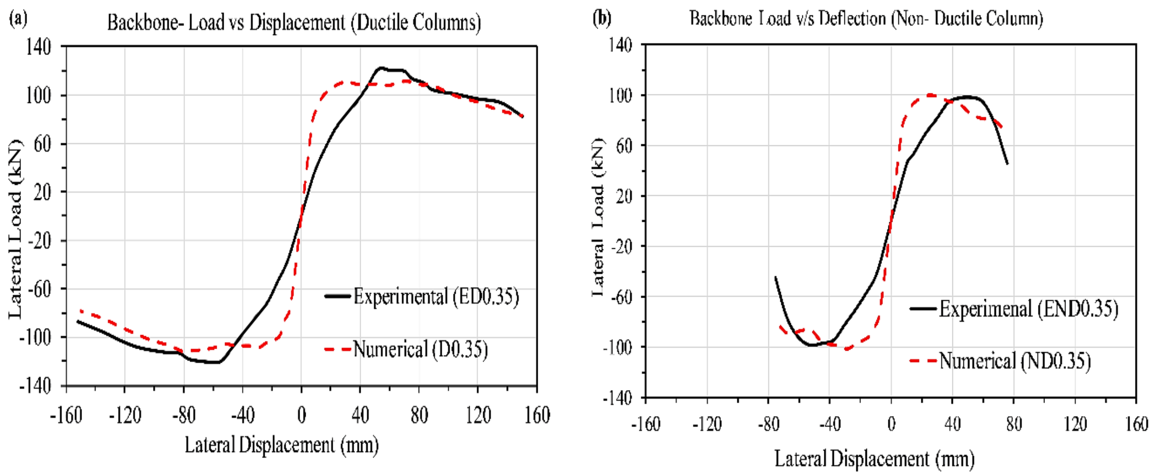

(a) Ductile Column (b) Non- ductile Column

Fig 2. 8 Backbone Response Comparison of Experimental Results and Numerical Models

Additionally, Table 2.4 provides a detailed comparative analysis of the flexural strength capabilities between the numerical model and the experimental results for both column specimens. This aspect is particularly important in seismic design, where structures must endure repeated loading cycles without catastrophic failure. This comprehensive comparison highlights the effectiveness of the numerical modelling approach and its relevance to understanding the behaviour of the RC structures under various loading conditions.

For further clarity, Fig. 2. 9 depicts the hinge failure observed at a drift level of 4% for both the experimental and numerical specimens. This figure serves as a critical visual representation, effectively illustrating the mechanisms of failure that occurred in the tested columns. By highlighting the specific points of failure,Fig 2. 9 allows for a deeper understanding of the failure patterns exhibited by ductile and non-ductile columns under cyclic loading conditions.

Table 2. 4 Comparison of Numerical and Experimental Results

Specimen Description	Specimen ID	Flexural Strength (kN)	Flexural Strength (kN)
Experimental Ductile Specimens	ED0.35	121.81	-120.75
Numerical Ductile Specimens	D0.35	111.28	-112.16
Experimental Non-Ductile Specimen	END0.35	98.05	-98.65
Numerical Non-Ductile Specimens	ND0.35	99.16	-101.84

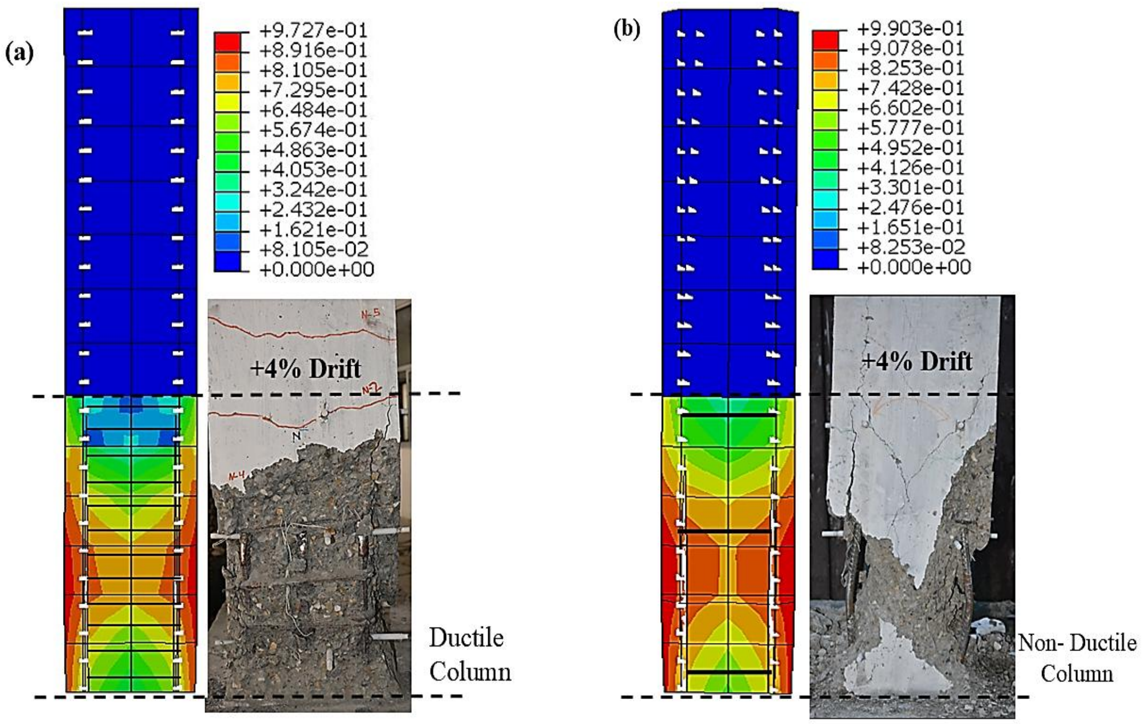

(a) Ductile Column (b) Non- Ductile Column

Fig 2. 9 Crack Pattern Comparison at 4% Drift Levels

2.8.3 Validation of Numerical Model for Corroded Ductile and Non-Ductile Columns

Following the validation of uncorroded specimens, the corroded ductile and non-ductile specimens were validated using the modified 3D numerical model, with the details outlined separately as follows:

2.8.3.1 Ductile Corroded Columns

Upon completing the validation of uncorroded specimens, the validation of the corroded ductile and non-ductile specimens was conducted using the modified 3D numerical model. Fig. 2. 10 provides a detailed schematic, illustrating the reinforcement layout, loading conditions, boundary parameters, and meshing specifics for the ductile corroded columns. To evaluate the model's accuracy, experimental and numerical results were compared by analyzing hysteresis responses of columns subjected to varying corrosion levels, as explained in Fig. 2.11 and their envelope curves, as presented Fig 2. 12. It is important to highlight that ACR levels were maintained constant at $0.35P_0$ throughout the comparison.

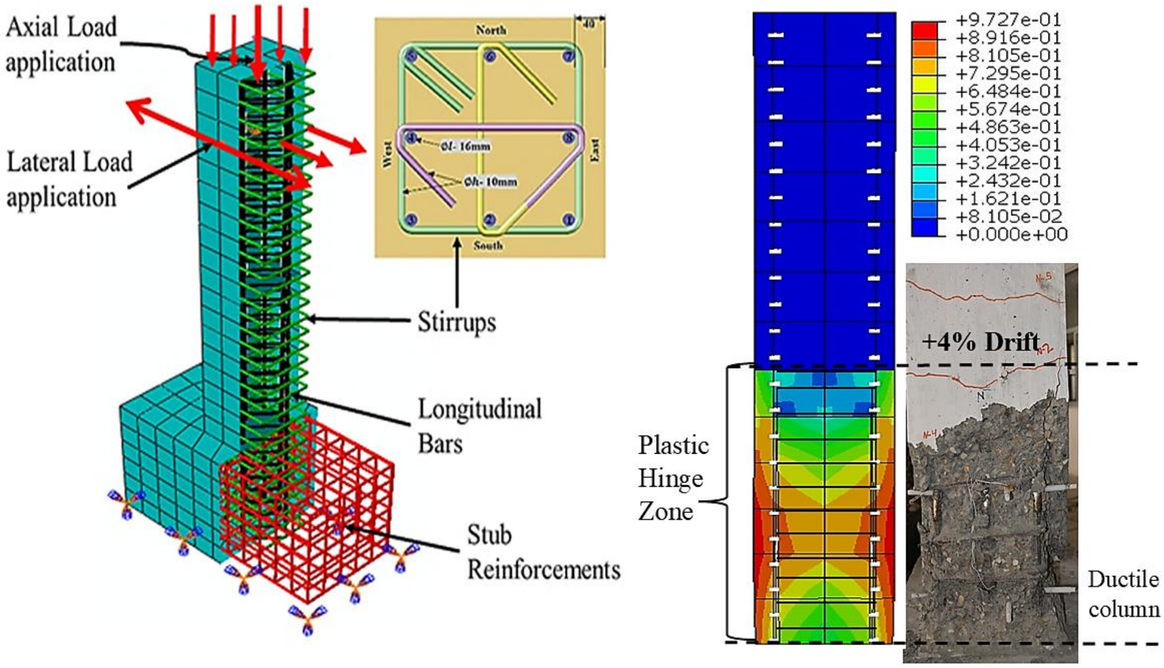

Fig 2. 10 Schematic of 3D Numerical Model Ductile Column with Reinforcement Details

The analysis confirmed a strong correlation between the numerical model and experimental results. It is also observed that the initial stiffness of experimental sound specimens was lower than that of the numerical models. This discrepancy can be attributed to the lack of adequate fixity at the base during the initial phases of experimentation.

Consequently, slight rotation at the base occurred during the early cycles of lateral load application, which reduced stiffness. However, after a few initial loading cycles, the column sustained some damage and became fully engaged, resulting in a more stable and consistent response. Furthermore, the damage observed at 4% drift in the experimental columns aligns well with the failure profile generated by the numerical model.

Table 2. 4 presents a comparative analysis of the peak flexural strength obtained from both the experimental tests and numerical models across all ductile corroded specimens. The column nomenclature includes the letter 'E' to denote Experimental results and 'N' for Numerical outcomes, and the numbers indicate the percentage of mass loss due to corrosion.

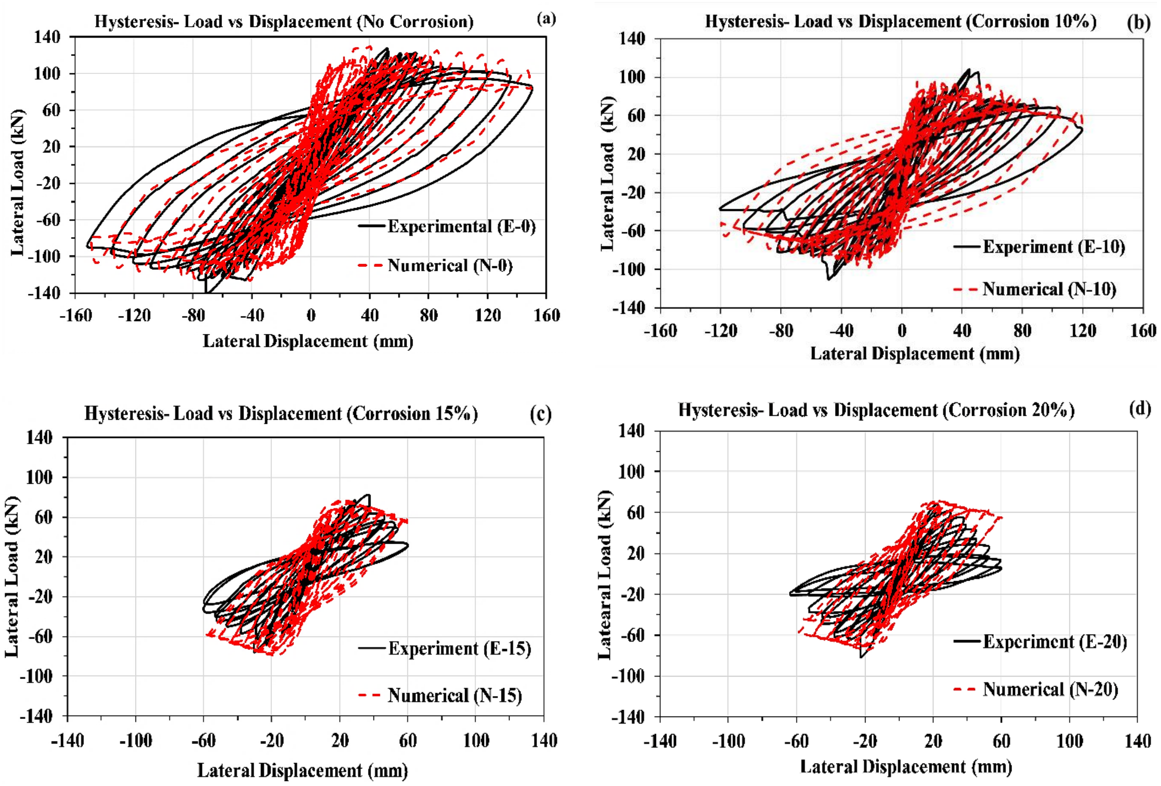

Fig 2. 11 Comparison of Hysteresis Response of Experimental Results and Numerical Model at (a) 0%, (b) 10%, (c) 15% and (d) 20% Corrosion Levels

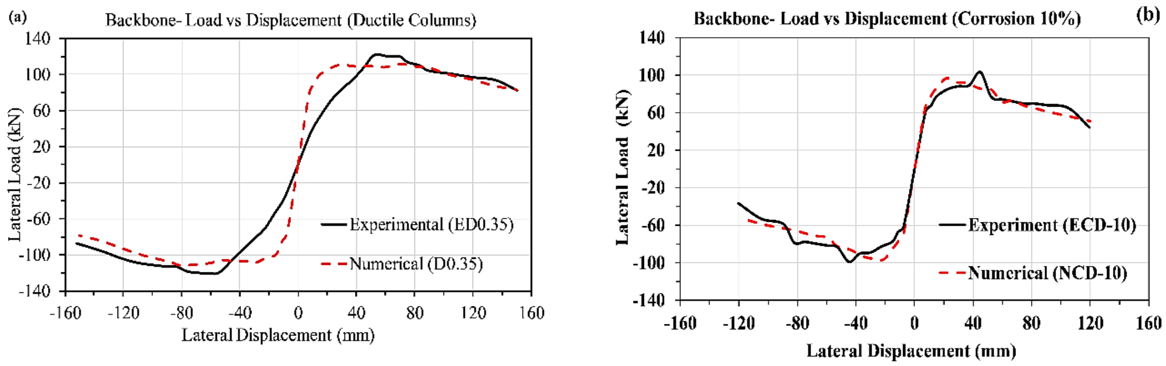

(a) 0% Corrosion

(b) 10% Corrosion

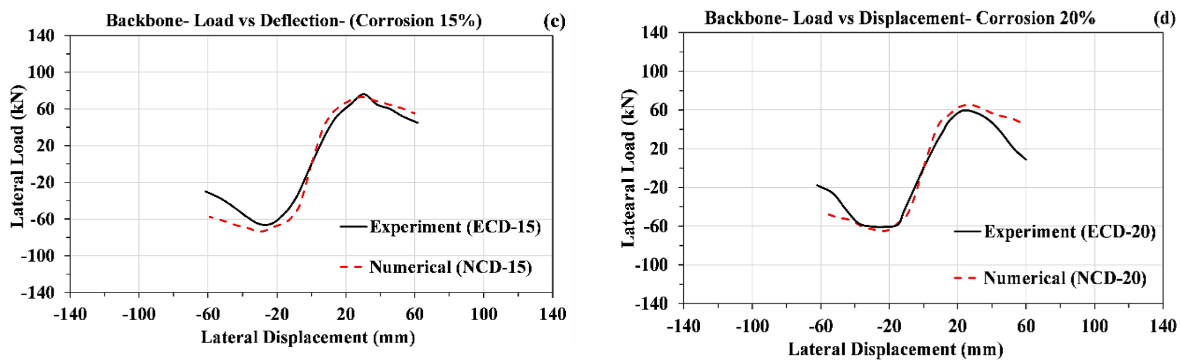

(c) 15% Corrosion

(d) 20% Corrosion

Fig 2. 12 Comparison of Backbone Hysteresis Response of Experimental and Numerical Results

Table 2. 5 Comparison of Past Studies on RC Columns

Specimen Description	Specimen ID	Flexural Strength (+ve)	Flexural Strength (-ve)
Non-Corroded Experimental Specimen	E-0	111.82	109.55
Non-Corroded Numerical Specimen	N-0	111.15	110.23
10% Corroded Experimental Specimen	E-10	102.17	98.94
10% Corroded Numerical Specimen	N-10	99.45	96.58
15% Corroded Experimental Specimen	E-15	71.97	69.95
15% Corroded Numerical Specimen	N-15	73.92	72.71
20% Corroded Experimental Specimen	E-20	62.56	61.34
20% Corroded Numerical Specimen	N-20	64.7	63.42

2.8.3.2 Non- ductile Corroded Columns

To validate the behaviour of non-ductile corroded specimens, 3D numerical models were developed, incorporating detailed reinforcement configurations, loading conditions, boundary constraints, and meshing specifications, as depicted in Fig. 2.13(a). Models clearly demonstrate that a stirrup spacing of 300 mm was maintained to simulate the behaviour of non-ductile column. To mitigate localized failures, stirrup spacing was reduced to 75 mm in column section above the plastic hinge zone.

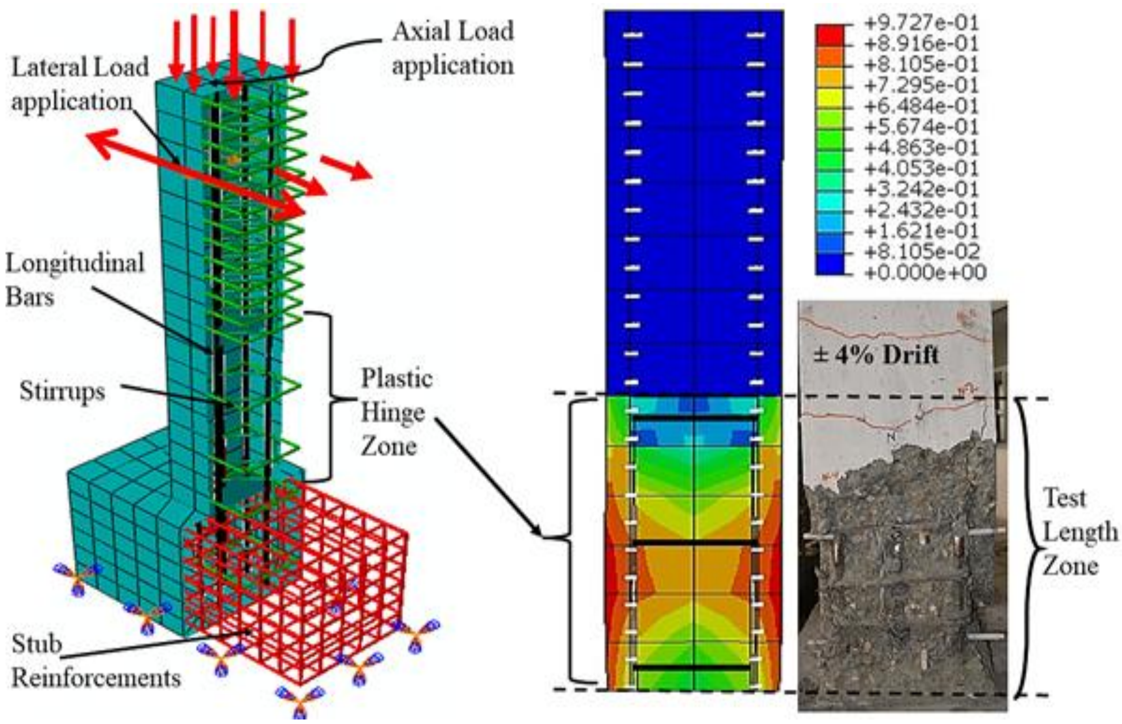

Fig 2. 13 (a) 3D Model Schematic of Non-ductile Corroded Column with Reinforcement Details (b) Experiment and Numerical Models Crack Pattern Comparison at 4% Drift levels

A comparative analysis of damage at a 4% drift level was performed using both experimental and numerical approaches, as illustrated in Fig. 2.13(b). The damage patterns observed in the experimental specimens align well with those predicted by the numerical models. Fig. 2.14 (a-c) and Fig. 2.15 (a-c) provide a comparison of the experimental and numerical hysteresis responses, along with their respective envelope curves. Notably, Fig. 2.15 (a) shows that the initial stiffness of the numerical model exceeded that of the experimental control specimen. This discrepancy can be attributed to a lack of base fixity during the early stages of experimentation, causing slight rotation at the base during initial lateral load cycles and resulting in reduced stiffness. However, once some damage occurred and the column models aligned, following the same trajectory after reaching a 2.5% drift level.

In subsequent tests, modifications were made to enhance base rigidity, and the addition of dial gauges confirmed that adequate fixity had been achieved, as negligible base displacement was recorded. Table 2.6 presents a detailed comparison of the peak flexural strength of NSRC corroded columns under various corrosion levels but with a constant ACR of $0.35P_0$. The results indicate a strong correlation between the numerical models and experimental data for all NSRC corroded columns. In Table 2.5, 'E' refers to Experimental results, 'N' denotes Numerical results, and the number represents the percentage of mass loss due to corrosion.

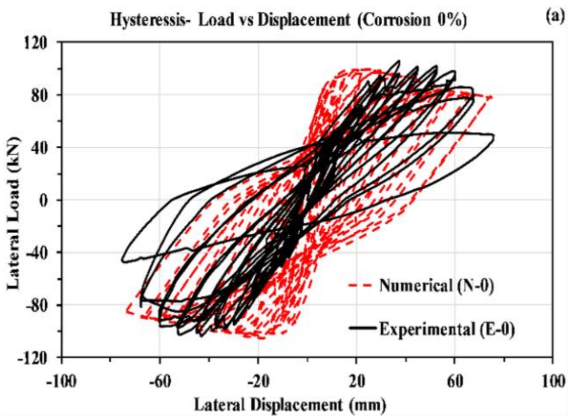

0% Corrosion

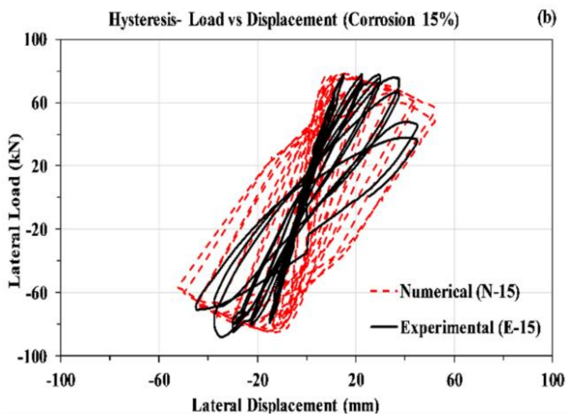

15% Corrosion

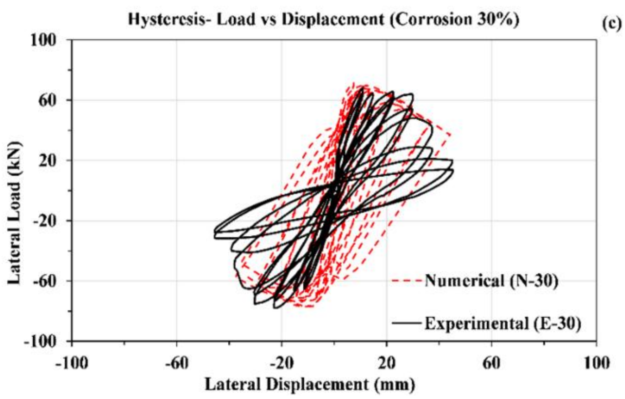

30% Corrosion

Fig 2. 14 Comparison of Hysteresis Response of Experimental Results and Numerical Models

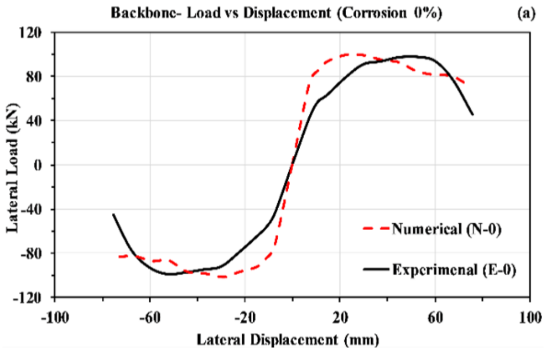

0% Corrosion

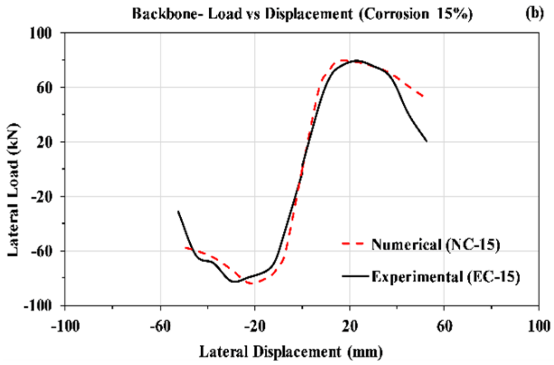

15% Corrosion

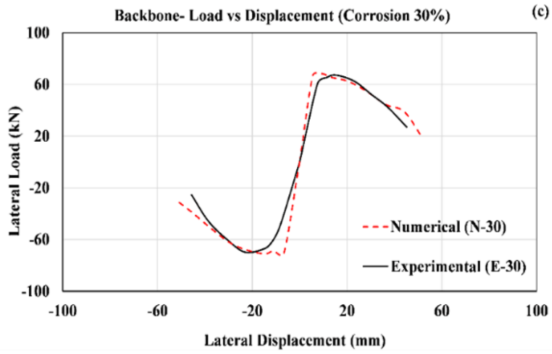

30% Corrosion

Fig 2. 15 Comparison of Backbone Response of Experimental Results and Numerical Models

Table 2. 5 Peak Strength comparison of experimental NSRC columns

Specimen Description	Specimen ID	Flexural strength (+ve)	Flexural strength (-ve)
0% Corroded Experimental Specimen	E-0	98.05	99.85
0% Corroded Numerical Specimen	N-0	98.97	101.84
15% Corroded Experimental Specimen	E-15	79.34	80.51
15% Corroded Numerical Specimen	N-15	79.30	79.74
30% Corroded Experimental Specimen	E-30	64.30	65.4
30% Corroded Numerical Specimen	N-30	68.1	68.65

Following the validation of experimental results for uncorroded and corroded ductile and non-ductile specimens, a comprehensive parametric study was undertaken to gain deeper insights into the structural behaviour under varied conditions. This study incorporated three critical variables: shear reinforcement, corrosion levels, and ACR. By examining a range of scenarios that integrated varying degrees of each parameter, the study aimed to establish a robust understanding of the interaction between corrosion-induced deterioration, shear reinforcement detailing, and axial load variations. The findings, including quantitative data and interpretive insights, are detailed in the following chapters.

Chapter 3

Seismic Performance of Uncorroded Ductile and Non-Ductile RC Columns under Varied ACRs

3.1 Introduction

This chapter presents a detailed investigation of quantifying and comparing the seismic response of uncorroded ductile and non-ductile RC columns subjected to various ACRs under identical quasi-static lateral cyclic loading.

In RC structures, columns play a critical role in maintaining structural stability under both gravitational and lateral loads, including those caused by seismic events. Field investigations have consistently revealed that high ACRs significantly increase the risk of compromised structural integrity and catastrophic failures (Yuan et al., 2023). Such vulnerabilities, combined with a deeper understanding of structural failures during seismic events, have driven substantial advancements in the design and reinforcement detailing of RC columns since the mid-20th century.

Historically, lateral reinforcement in columns was primarily designed to resist shear forces and prevent buckling of longitudinal bars. However, with the evolution of seismic design principles, lateral reinforcement has gained prominence for its role in enhancing the ductility of RC columns. Ductility is a critical property that enables structures to dissipate energy and avoid catastrophic brittle failure during earthquakes. Modern seismic design achieves the required ductility by optimizing both the quantity and configuration of lateral reinforcement. This is typically accomplished by incorporating closely spaced transverse reinforcement, such as closed stirrups or hoops of suitable diameter. These measures effectively confine the concrete core, delay the onset of cracking, and prevent premature buckling of longitudinal reinforcement. This confinement ensures that RC columns can sustain large deformations without significant loss of strength, thereby improving their seismic performance.

The introduction of ductile detailing guidelines in building design codes, beginning in the early 1970s and continuing through the late 1990s, marked a critical shift in seismic design philosophy. These guidelines were developed based on a comprehensive understanding of various parameters that influence the behaviour of RC columns under seismic loading. Key factors considered include cross-sectional dimensions (Z. Li et al., 2019) and confining pressure provided by lateral reinforcement (Zhu et al., 2016). Experimental study on steel-reinforced high-strength concrete columns under cyclic lateral force and constant axial load, material properties, levels of axial compressive load (Yuen & Kuang, 2017), design and placement of longitudinal reinforcement (Shi et al., 2021), hook angles of stirrups (Tanaka & Park, 1993) and the quantity of transverse reinforcement (Azizinamini et al., 1992). These design principles, now embedded in modern building codes, have significantly improved the seismic performance of RC structures. They ensure that columns can sustain large deformations without losing their load-bearing capacity, thereby enhancing the resilience of buildings in earthquake-prone regions. This evolution in design philosophy underscores the importance of integrating empirical findings and research insights into practical engineering solutions to mitigate the risks associated with seismic events.

Several international building design codes, such as the (Canadian Standards Association, 2004) and the (New Zealand Standard, 2006) have incorporated the effects of ACR when determining the required reinforcement for RC structures. These guidelines acknowledge that ACR plays a critical role in the structural integrity of RC columns, particularly under seismic loading. In contrast, other prominent codes, such as the IS13920:1993 (Bureau of Indian Standard, 1993) and the ACI 318:2011 (ACI Committee 318-11, 2011) do not account for ACR levels when calculating lateral reinforcement requirements, potentially leading to differences in the seismic performance of structures designed under these frameworks.

Prior to the adoption of modern ductile detailing provisions, as discussed by (A.W. Taylor et al., 1997) existing stocks of RC columns were not designed with seismic adequacy in mind. These older columns are often referred to using terms such as "shear-critical," "shear-deficient," "lightly reinforced," or "non-ductile," reflecting their susceptibility to brittle failure under seismic stress. In contrast, contemporary RC columns constructed with ductile detailing standards are classified as "ductile columns," reflecting their enhanced capacity to withstand seismic loads through improved energy dissipation and deformation capacity.

To deepen the understanding of the seismic behaviour of non-ductile RC columns, especially those constructed before the introduction of these ductile detailing criteria, several experimental, analytical, and numerical studies have been conducted. These efforts aim to evaluate the influence of various factors—including axial load levels and reinforcement configuration on the seismic response of non-ductile columns (Rajput & Sharma, 2018). The findings from such studies contribute to the broader understanding of how older, non-ductile structures behave during earthquakes and offer insights into potential retrofitting strategies for improving their seismic resilience. Numerous experimental investigations have been conducted on RC columns to evaluate their behaviour under different loading conditions (Rodrigues, 2018; B. Wu et al., 2022; Yuan et al., 2023). These studies provide important insights into how material characteristics impact the structural performance of RC columns.

Moreover, several researchers have specifically explored how ACR influences the seismic response of non-ductile RC columns (B. Wu et al., 2022). These columns, due to inadequate reinforcement detailing, often experience premature longitudinal bar buckling, early concrete crushing, and a reduction in axial load-carrying capacity, as noted by (Rodrigues, 2018). It has been observed that increased axial compression tends to reduce the ductility of RC columns while simultaneously enhancing their flexural strength. For example, (Choi & Lee, 2022) found that the flexural strength of full-scale RC columns increased as ACR approached $0.6P_0$ but began to decrease beyond that point. Importantly, their research demonstrated that closely spaced stirrups effectively mitigated longitudinal bar buckling, which helped improve ductility by reducing stirrup spacing and limiting axial load. Furthermore, (Rajput & Sharma, 2018) have proposed retrofitting techniques to enhance the seismic performance of non-ductile columns, particularly in their test-length regions. However, most research to date has focused on lightly reinforced or shear-deficient columns, with limited studies addressing the seismic response of both ductile and non-ductile columns in relation to ACR levels.

This research work aims to highlight a critical gap in current building codes. Even the most recent revisions of ductile detailing guidelines, such as (IS-13920, 2016) and (ACI Code Committee 318-14, 2014) have not adequately considered the impact of ACR. This omission has led researchers (Narayanan, 2011) to advocate for including ACR effects in modern ductile detailing provisions.

This research thoroughly investigates the seismic behaviour of columns with varying levels of ductility and ACRs, offering insights into their failure mechanisms and providing a basis for refining seismic design practices.

3.1.1 Confinement of Concrete

The configuration of lateral reinforcement played a pivotal role in addressing the confinement effects within RC structures. Confined regions, particularly the hatched areas within the reinforcement cage shown in Fig.3.1, exhibited significantly higher compressive strength and more ductile behaviour after reaching peak load compared to the unconfined concrete regions, represented by the non-hatched portions. This distinction highlights the importance of reinforcement configuration in enhancing the structural resilience of concrete elements. In terms of tensile behaviour, the analysis focused on critical factors such as concrete's tensile strength, post-peak behaviour, and fracture energy.

The (CEB-FIP Model code, 2010) served as the basis for this analysis, offering a comprehensive framework for assessing the tensile performance of concrete under various stress conditions. This model allowed for an in-depth exploration of how concrete responds to tensile forces, especially in the context of post-cracking behaviour and energy dissipation. It specifically examines the load-deflection behaviour in both compression and tension, particularly during the post-peak phase, where the material's structural integrity begins to decline.

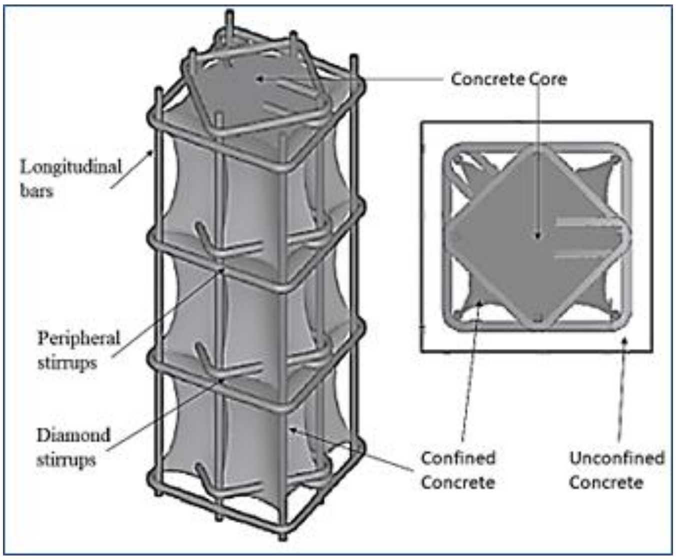

Fig. 3. 1 Explanation of Concrete Zoning in an RC Structure (Narayanan, 2011)

3.1.2 State of Knowledge

This chapter particularly focuses on the seismic response of uncorroded ductile and non-ductile RC columns. It also highlights the significant advancements in understanding their behaviour under various ACR levels. Furthermore, this research underscores the critical role of ductility in enhancing seismic performance achieved through optimized lateral reinforcement configurations. Previous and experimental studies reveal that the ductile columns, designed with closely spaced transverse reinforcement, demonstrate superior energy dissipation and deformation capacity compared to non-ductile columns, which are prone to brittle failure under seismic stress. However, current building codes often neglect the impact of ACR on reinforcement design, presenting a gap in modern seismic guidelines. Addressing this gap, our recent investigations emphasize refining the design practices and retrofitting strategies to improve the resilience of both ductile and non-ductile RC columns.

3.1.3 Significance of the Research

The proposed research addresses a critical gap in understanding the seismic behaviour of RC columns under the influence of different axial load levels or ACR, a factor often overlooked in current structural design codes. Standards such as (IS-13920, 2016) and (ACI Code Committee 318-14, 2014) fail to incorporate ACR's effects in their ductile detailing guidelines. This omission could compromise the seismic safety of RC structures, particularly in regions with high seismic risk. By systematically investigating the influence of ACR on both ductile and non-ductile RC columns, this study offers transformative insights into their performance under seismic loading. Unlike most existing research, which primarily examines lightly reinforced or shear-deficient columns, this work focuses on adequately reinforced or ductile columns, bridging a significant research gap.

The research employs a robust methodology integrating numerical simulations and parametric analyses to quantify the seismic response and identify optimal axial compression levels. The outcomes are expected to inform critical revisions to global ductile detailing standards, addressing current design limitations and enhancing the resilience of RC structures. The broader implications of this work are profound. By accounting for ACR in the design of ductile reinforcements, this research will not only improve seismic performance but also contribute to safer, more resilient infrastructure, ultimately safeguarding lives and reducing economic losses during seismic events.

3.1.4 Research Methodology

3.1.4.1 Specimen Details

Eight three-dimensional FE models were developed, including four ductile and four non-ductile column specimens, to investigate the influence of ACR on their structural performance. The FE models were subjected to varying ACR levels of $0.35P_o$, $0.5P_o$, $0.6P_o$, and $0.7P_o$. Each column measured 1800 mm in height with a cross-section of 300 × 300 mm. A footing or joint was represented by a stub measuring 1000 × 520 × 600 mm and a 40 mm concrete cover throughout the specimen. Longitudinal reinforcement consisted of eight #8 (Ø16 mm) bars, while lateral reinforcement consisted of Ø10 mm, which varied based on ductility requirements. Ductile columns included closely spaced transverse reinforcement at 75 mm c/c, achieving a reinforcement ratio of 1.31%, whereas non-ductile columns lateral reinforcements were widely spaced at 300 mm c/c, resulting in a reduced reinforcement ratio of 0.33%. The plastic hinge region, extending 800 mm from the stub face, was designated as the test length, as it is considered to be the most vulnerable area to damage during seismic events.

3.1.4.2 Study Variables

This study examines two critical variables to evaluate the seismic behaviour of RC columns. The first variable is the spacing of lateral reinforcement, which is set at 75 mm and 300 mm to represent ductile and non-ductile column specimens, respectively. The choice of these reinforcement spacings is focused on their distinct impact on concrete confinement and the column's structural performance under cyclic loading. Second variable is ACR investigated at four discrete levels: $0.35P_o$, $0.5P_o$, $0.6P_o$ & $0.7P_o$.

3.1.4.3 Calculations and Loading Protocol

To replicate the loading protocols used in the experimental setups, a similar approach was implemented in the FE models. Fixed boundary conditions were applied at the base of all specimens in the models, while symmetry and contact conditions at the reinforcement-concrete interface were defined using an embedded region. During the simulations, a constant axial load was maintained throughout, representing the dead or gravitational loads typically experienced by columns. For instance, one specimen was subjected to seismic loading under a constant axial load of $0.35P_0$. Similarly, the axial load was increased to $0.5P_0$, $0.6P_0$, and $0.7P_0$ for additional specimens under identical seismic loading conditions. The calculation of axial capacity of column (P_0) at varying ACR from $0.35P_0$ to $0.7P_0$ was determined using the following formula:

$$P_0 = 0.85 * f_c * A_c * f_y * A_{st} \tag{3.1}$$

Where P_0 represents the axial capacity of the column under concentric axial load, f_c is the compressive strength of the concrete cylinder, A_c is the net area of the concrete, f_Y is the yield strength of the longitudinal reinforcement, and A_{st} is the area of the longitudinal reinforcement.

A quasi-static increasing magnitude lateral displacement loading was applied for the seismic loading scenario. The lateral load history and number of cycles followed the recommendations outlined in ACI 374.2R-13 (2013), which involved two loading cycles up to 5% drift levels, followed by a single cycle once the drift exceeded 5%, as shown in Fig. 3.2. To evaluate the seismic performance of the column specimens, data were gathered on the lateral load-displacement hysteresis response. The loading process continued beyond peak load, extending past point where the lateral load decreased to $0.85V_{max}$ in order to capture the post-peak behaviour and generate envelope curves at higher displacement levels.

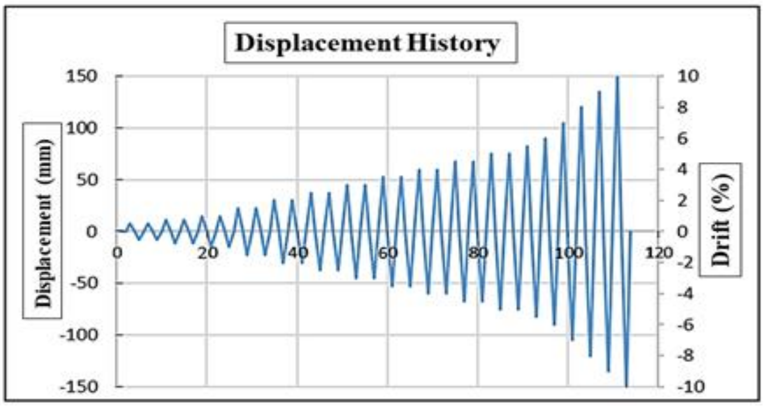

Fig. 3. 2 Quasi-Static Increasing Magnitude Lateral Displacement History

3.2 Results and Analysis

An extensive parametric analysis systematically examined the influence of varying ACR levels on the seismic performance of ductile and non-ductile RC columns by varying ACR levels from $0.35P_0$ to $0.7P_0$. The material properties, boundary conditions, and lateral displacement histories were taken from the experimental setup and were uniformly maintained across all specimens. Seismic responses of all eight numerical models were thoroughly analyzed using a comprehensive set of comparative parameters. These parameters included hysteresis behaviour, envelope curves, stiffness degradation, energy dissipation, equivalent viscous damping ratio, deformability characteristics, and ductility factors. Each of these measures provided valuable insights into the behaviour of RC columns under seismic loading, enabling a detailed understanding of how ACR influences their performance, which are thoroughly explained as follows:

3.2.1 Hysteresis Response and Envelope Curves

The lateral load-displacement hysteresis responses of the eight numerical models, comprising both ductile and non-ductile RC columns with varying ACRs, are presented in Fig. 3.3 (a-d) and Fig. 3. 4 (a-d), respectively. These hysteresis curves are very critical in identifying the common failure mechanisms in the numerical models, such as the initiation of tensile failure in the cover concrete, which corresponds to the flexural cracking observed in experimental setups, and the progression of failure into core concrete, indicative of cover spalling and buckling of longitudinal reinforcement bars.

In the elastic phase of response, the load-displacement relationships across all specimens were found to be linear and uniform, reflecting the unyielding nature of the columns under lower drift levels. However, as the drift increased, the load-displacement trajectories entered the plastic phase, which was influenced by the specific ACR levels and the amount of lateral reinforcement in each specimen. The transition to the plastic response phase was marked by the initiation of cracks in the cover concrete, leading to a significant reduction in stiffness and a widening of the hysteresis loop, primarily due to a

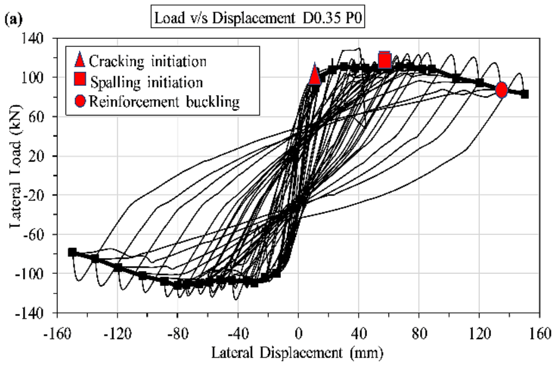

(a) $0.35P_0$

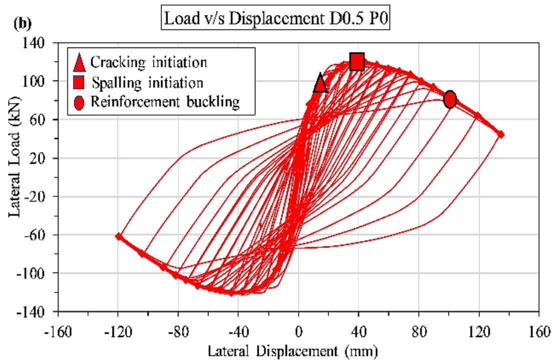

(b) $0.5P_0$

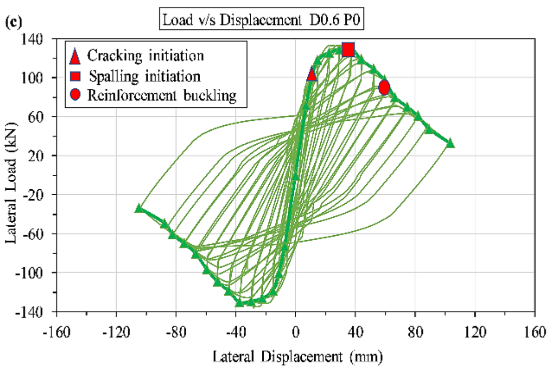

(c) 0.6P0

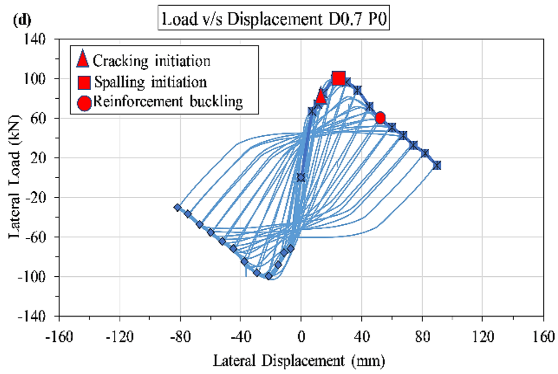

(d) $0.7P_0$

Fig. 3. 3 (a)-(d) Hysteresis Curves of Numerical Ductile Columns at Various ACR and with Different Stages of Failure

weakened unloading path. The point of failure in each model is defined as the point in the post-peak domain where the lateral load reduces to 85% of the peak load. However, the numerical analysis was performed beyond the post-peak domain for both ductile and non-ductile columns at varying ACR to investigate the deterioration pattern critically.

It was observed that, as the ACR was increased from $0.35P_o$ to $0.7P_o$, the hysteresis loops became progressively more constrained in both the column types, hence steeply reducing their energy dissipation and ductility. Envelope (backbone) curves, derived from the hysteresis responses (Fig. 3.5 a-b), further illustrated the comparative performance of the columns with varying ACR levels, highlighting their peak strength and ductility. For ductile columns, the flexural strength increased with ACR levels up to $0.6P_o$ but began to decline sharply beyond this point.

In contrast, the non-ductile columns exhibited a steady decrease in flexural capacity as ACR levels increased, consistent with the findings of earlier studies by (Murat Saatcioglu, 1989). Moreover, the envelope curves regardless of the amount of transverse reinforcement. This deterioration in the post-peak domain underscores the critical role of ACR in influencing the structural resilience of both ductile and non-ductile columns under seismic loading, reinforcing the need for careful consideration of ACR in the design and assessment of RC structures situated in seismic zones.

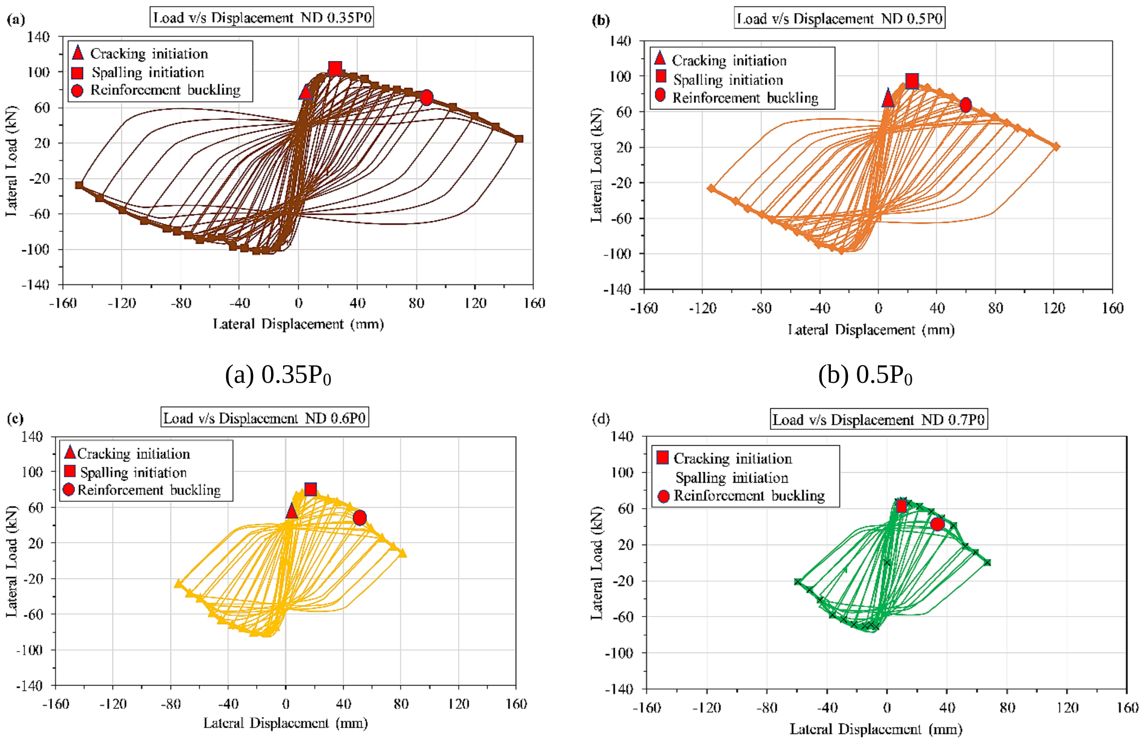

(a) $0.35P_0$ (b) $0.5P_0$

(c) $0.6P_0$ (d) $0.7P_0$

Fig. 3. 4 (a)-(d) Hysteresis Curves of Numerical Non-Ductile Columns at Various ACRs and with Different Stages of Failure

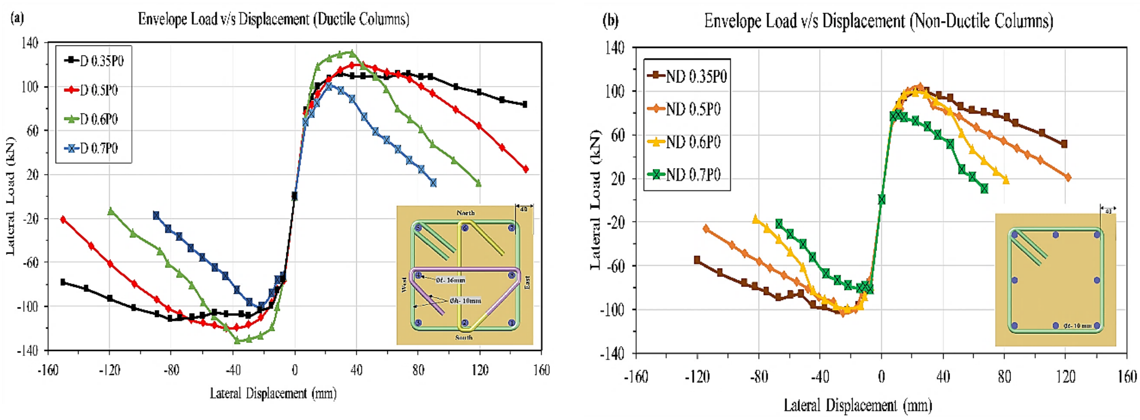

(a) Ductile column (b) Non- Ductile column

Fig. 3. 5 Envelope Load v/s Displacement Profile Comparison

3.2.2 Stiffness Deterioration

The secant stiffness (K_n) for each cycle was evaluated by determining the slope of line connecting the peaks of both positive and negative cycles. When the number of cycles exceeded one (i.e., up to a 5% drift level), an average stiffness value was computed for each drift level. This process is visually represented in Fig. 3.6, which outlines the procedure for calculating the second stiffness during each cycle. The actual stiffness measured during each cycle was plotted against lateral displacement, resulting in stiffness degradation curves. This degradation is a key indicator of structural performance, as stiffness (K) is considered a critical parameter in evaluating the extent and rate of deterioration in a structure. Factors such as cross-sectional loss, buckling of longitudinal rebars, and bond slip between the steel reinforcement and concrete contribute to the observed stiffness degradation. Fig. 3.7(a) and (b) present the stiffness degradation versus displacement responses for both ductile and non-ductile RC columns. It is evident from these figures that increasing the ACR, accelerates the stiffness degradation

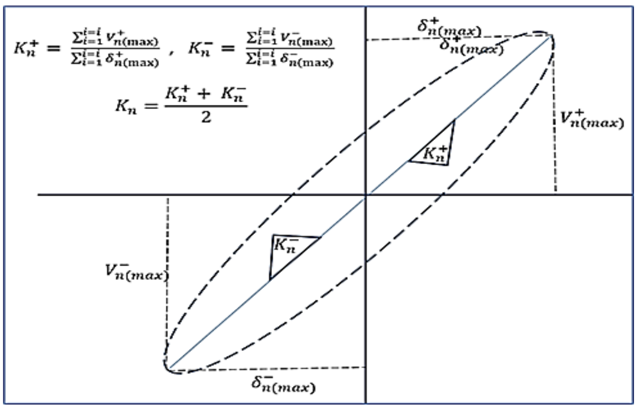

Fig. 3. 6 Tensile Stress-Strain Behaviour of Steel Rebars

Here, V_n represents lateral load, and δ_n denotes the corresponding displacement at the n^{th} drift level. Secant stiffness in the positive half-cycle at n^{th} drift level is labelled as K_n^+, while the stiffness in the negative half-cycle is denoted as K_n^-. The average stiffness (K_n) was calculated across multiple cycles at each drift level.

in both column types. However, the non-ductile specimens exhibited more pronounced stiffness degradation than their ductile counterparts. For a further clearer understanding, Fig. 3. 8 provides a comparison between ductile and non-ductile specimens at the same ACR levels.

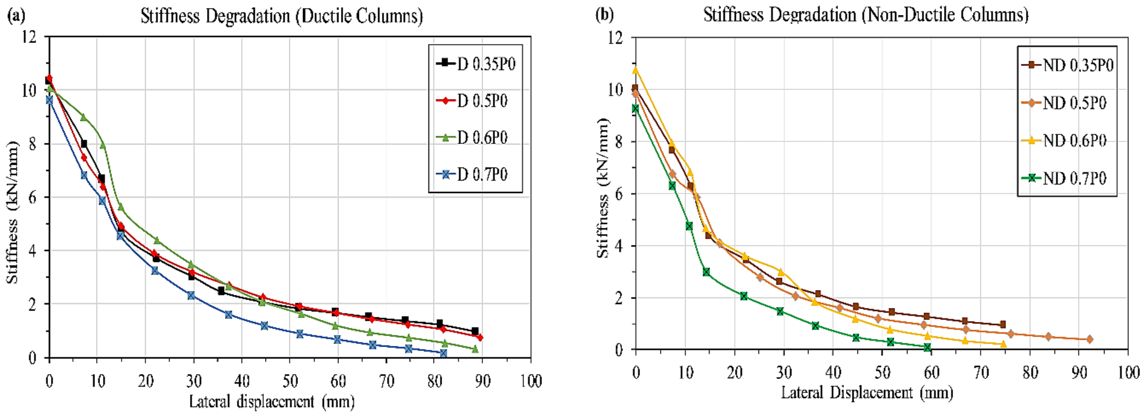

(a) Ductile Column (b) Non- ductile Column

Fig. 3. 7 Stiffness degradation profile comparison

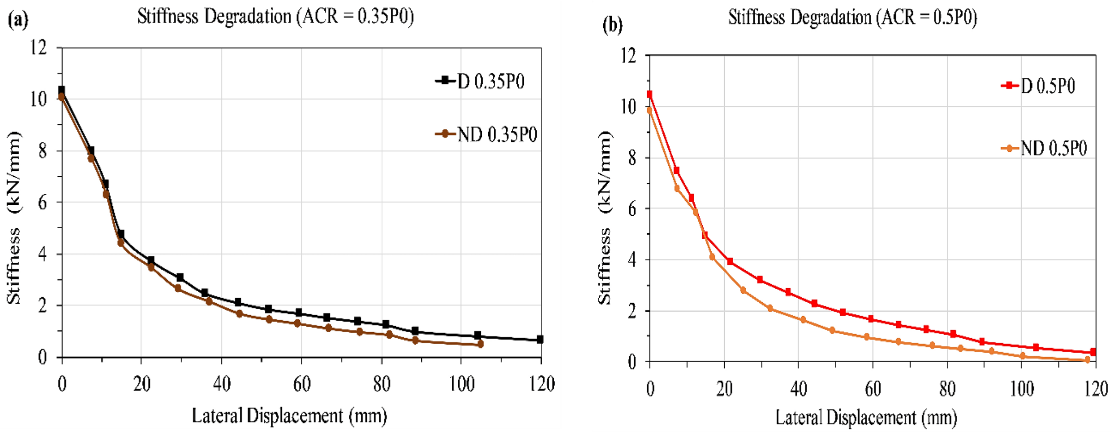

(a) $0.35P_0$ (b) $0.5\ P_0$

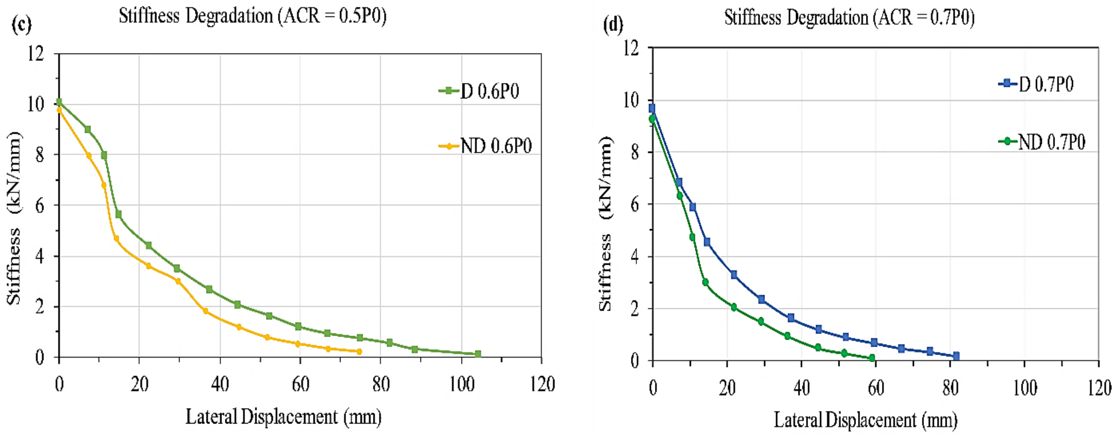

(c) $0.6P_0$ (d) $0.7\ P_0$

Fig. 3. 8 Stiffness Degradation of Ductile and Non-ductile Columns at Constant ACR Levels

At a moderate ACR level of $0.35P_0$, both column types followed a similar stiffness degradation trajectory, as depicted in Fig. 3.8(a). However, at higher ACR levels, a noticeable performance gap emerged, with non-ductile columns showing significantly greater degradation than the ductile columns. This trend is evident in Fig. 3. 8 (b), (c), and (d), which show stiffness degradation at ACR levels of $0.5P_0$, $0.6P_0$, and $0.7P_0$, respectively.

3.2.3 Energy Dissipation Capacity

The energy dissipated in each loading cycle was determined by calculating the area enclosed by the hysteresis loop, as represented by Area ABCDE in Fig. 3. 9. This area was computed using a MATLAB program. To assess the cumulative energy dissipation at a given drift level, the energy dissipated during the current cycle was added to the energy dissipated in all previous cycles. Similarly, the total energy dissipation up to the ultimate failure point (defined as $0.85F_p$), referred to as ultimate cumulative energy dissipation (E_u), was determined by summing the energy dissipated

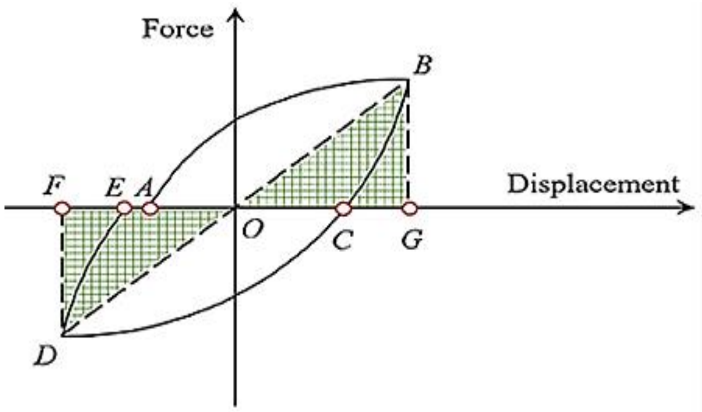

Fig. 3. 9 Calculation of energy dissipation for a given cycle

up to the structure's ultimate response point. Fig. 3.10 (a) and (b) depict the cumulative energy distribution, expressed in kilonewton-meters (kN-m), with respect to lateral drift, measured in millimeters (mm), for both ductile and non-ductile reinforced concrete columns. It is evident that as the axial compression ratio (ACR) increases, the energy dissipation capacity of the columns is significantly reduced. Notably, the performance of columns with an ACR of $0.7P_0$ was found to be lower than half of specimen with $0.35P_0$.

To further investigate the combined effects of reinforcement configuration and ACR levels on energy absorption, Fig.3.11 presents a comparison of ductile and non-ductile columns at equivalent ACR levels. It is clear from this comparison that the cumulative energy dissipation is significantly lower in specimens lacking ductile reinforcement, indicating a weaker post-peak response. The performance gap between ductile and non-ductile columns becomes more pronounced as ACR levels increase, as shown in Fig. 3.11 (a), (b), (c), and (d), which illustrate the cumulative energy dissipation for ACR levels of $0.35P_o$, $0.5P_o$, $0.6P_o$, and $0.7P_o$.

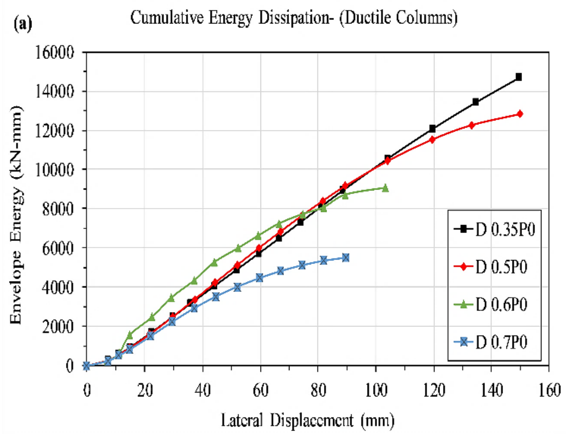

(a) Ductile Column

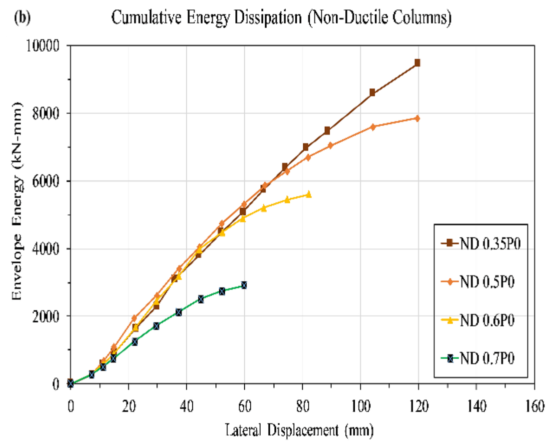

(b) Non- Ductile Column

Fig. 3. 10 Cumulative energy dissipation comparison with the horizontal displacement

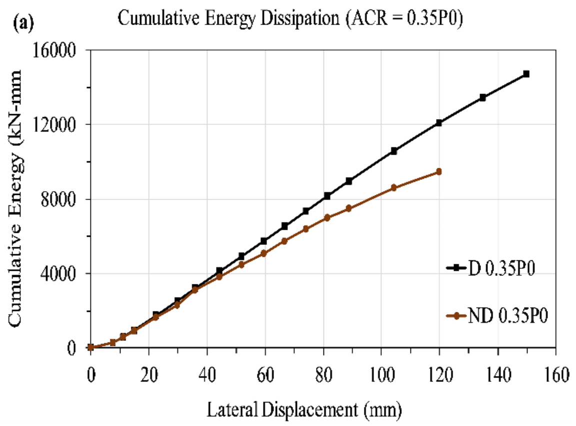

(a) $0.35P_0$

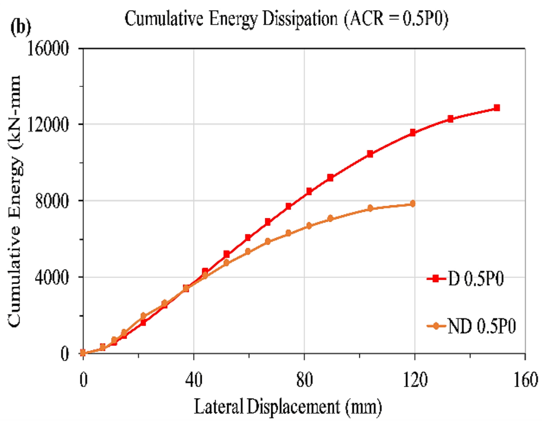

(b) 0.5 P_0

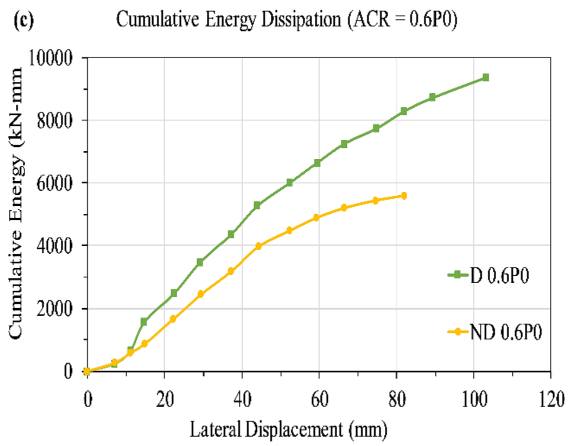

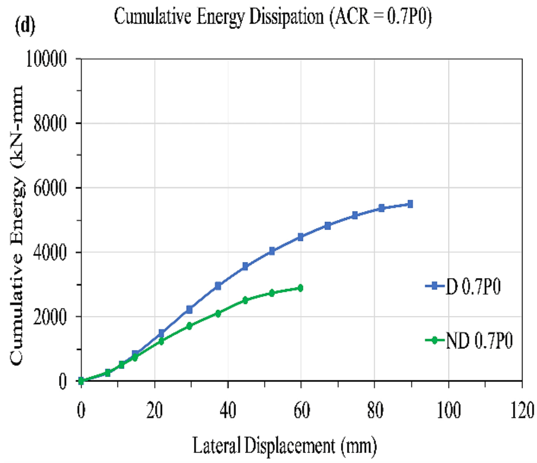

(c) $0.6P_0$

(d) 0.7 P_0

Fig. 3. 11 Cumulative Energy Dissipation Comparison with the Horizontal Displacement at Constant ACR Levels

3.2.4 *Equivalent Viscous Damping Ratio*

The equivalent viscous damping ratio (ξ_{eq}) is a key parameter that quantifies the hysteretic energy dissipation of structural specimens under cyclic loading. This ratio, also referred to as the "dissipation factor," represents the proportion of energy dissipated relative to the energy that would be generated by an elastic body subjected to the same displacement, as defined by (Dai et al., 2020; Mohebkhah & Tazarv, 2021). Fig. 3.9 illustrates a typical hysteresis loop, showing how ξ_{eq} is calculated where the area enclosed by the hysteresis loop (S_{ABCDE}) is compared to the areas of the triangles S_{ODF} and S_{OBG} within the same loop and the same has been explained in Equation 3. 2.

$$\xi eq = \frac{1}{2\pi}\frac{S_{ABCDE}}{S_{ODF}+S_{OBG}} \tag{3.2}$$

The ξ_{eq} values for all eight finite element models, both ductile and non-ductile, with varying ACRs are presented in Fig 3. 12 (a) and (b). Prior to yield displacement, the ξ_{eq} values for ductile and non-ductile columns were found to be relatively similar. However, as the lateral displacement increased, there was a gradual rise in ξ_{eq} values. It was observed that, regardless of the confinement ratio, an increase in ACR consistently led to higher ξ_{eq} values across all specimens.

This trend demonstrates a clear correlation between increased ACR and enhanced energy dissipation capacity. Among the ductile specimens, the D0.35P₀ specimen exhibited the lowest ξ_{eq} value under the same displacement, whereas the D0.7P₀ specimen achieved the highest ξ_{eq} value. Interestingly, in non-ductile specimens, the absence of proper confinement resulted in a significant increase in ξ_{eq} values, highlighting the impact of inadequate reinforcement on energy dissipation performance. Hence, the analysis of ξ_{eq} values reveals that an increase in ACR is directly proportional to the equivalent viscous damping ratio and inversely proportional to the ductility of both ductile and non-ductile columns. This indicates that higher ACR levels contribute to more energy dissipation but reduce the overall ductility of the specimens, particularly in those lacking proper confinement.

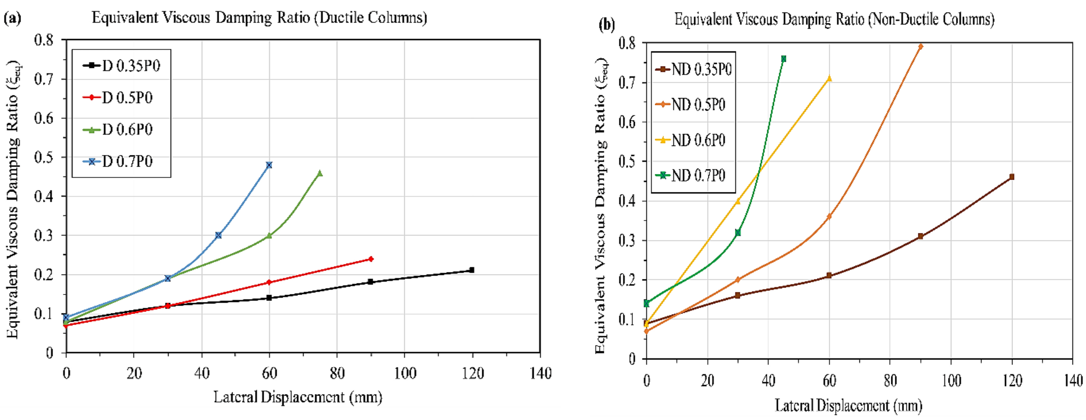

(a) Ductile Columns (b) Non-ductile Columns

Fig. 3. 12 Equivalent Viscous Damping Ratio Comparison

3.2.5 Deformability and Displacement Ductility

The deformability characteristics of the column specimens were assessed by identifying three critical stages in their load-deflection response: yield, peak, and ultimate stages. The yield point on the load-displacement curve was determined using the equivalent elastic-plastic energy method, as outlined by (Park, 1989) and illustrated in Fig. 3. 13.

This method helps identifying the transition from elastic to plastic behaviour in the structure. The peak point corresponds to the maximum lateral force, commonly referred to as the flexural strength of the specimen. The ultimate point was defined as the stage where the lateral force dropped to 85% of the peak value, marking the onset of a significant structural deterioration. In this study, the deformability of the column specimens was evaluated by comparing the yield, peak, and ultimate points across varying ACRs and reinforcement configurations. It was observed that deformability characteristics,

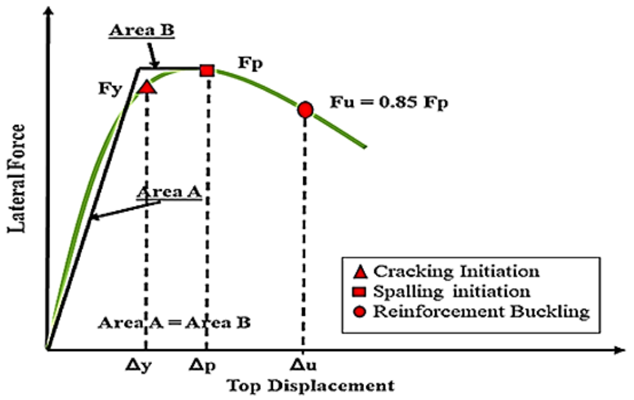

Fig. 3. 13 Illustration of Equivalent Energy Method

particularly in the pre-peak and post-peak response trajectories, were significantly impacted by increases in ACR. The specific values of yield, peak, and ultimate displacements for each specimen are presented in Table 3. 1, which provides a clear overview of how these parameters change with different ACR levels.

A comprehensive visualization of the combined effects of lateral reinforcement configuration and ACR on deformability is shown in Fig. 3.14. The data indicate that an increase in ACR consistently reduced the yield, peak, and ultimate displacements, highlighting the detrimental impact of higher axial loads on the structure's deformability. In addition to deformability characteristics, the study also captured the ductility features of all eight specimens, using the ductility factor/ratio (Δ_μ) and ultimate cumulative energy dissipation (E_u) as key indicators.

Ductility, a critical property in structural design, refers to a structure's capacity to endure deformation without significant loss of strength and stiffness beyond its elastic phase. The ductility

Table 3. 1 Parametric Studies Summary

Specimen ID	Axial load (kN)	Yield force F_y (kN)	Yield Disp. Δ_y (mm).	Peak force F_p (kN	Peak Disp. Δ_p (mm)	Ultimate force Fu (kN) (0.85Fp)	Ultimate Disp. (Δu) (mm)	Ductility factor (μ)	Ultimate Energy Dissipation (kN-m)
Ductile Column									
D0.35	941.0	72.63	8.73	111.74	77.205	95	117.75	13.48	77.52
D0.5	1344.5	77.68	9.62	119.51	40.82	101.6	81.12	8.43	47.7
D0.6	1613.4	84.59	9.94	130.15	37.31	110.2	52.4	5.27	20.8
D0.7	1889.3	64.92	7.61	99.89	21.95	84.9	38.17	5.01	8.3
Non-ductile Column									
ND 0.35	941.0	65.19	5.03	100.3	25.545	85.42	52.13	10.36	22.1
ND 0.5	1344.5	60.71	4.96	93.41	25.32	79.39	46.21	9.32	18.7
ND 0.6	1613.4	52.35	4.97	80.55	14.175	68.47	49.16	9.89	9.0
ND 0.7	1889.3	45.35	4.53	69.78	9.1525	59.31	40.17	8.87	4.5

factor is calculated as the ratio of ultimate displacement (Δ_u) to the yield displacement (Δ_y), i.e., $\Delta_\mu = \Delta_u/\Delta_y$. Meanwhile, E_u represents the total energy dissipated by the specimen up to its ultimate point. The importance of the ductility factor is further highlighted by its inclusion in design codes such as the (New Zealand Standard, 2006) and the (Canadian Standards Association, 2004) which incorporate the influence of ACR into the design formulas for confining reinforcement.

Table 3. 1 lists the ductility parameters for the eight specimens, illustrating how increases in ACR led to a pronounced reduction in both Δ_μ and E_u. Fig. 3.15 further highlights this reduction in ductility, showing a consistent decline in ultimate cumulative energy dissipation for both ductile and non-ductile columns.

However, an unexpected trend was observed in the non-ductile columns at higher ACR levels, where the ductility factor increased. This finding contradicted previous research (Cheng et al., 2020) and was traced to a severe reduction in the yield displacement (Δy), which serves as the denominator in the ductility ratio calculation. As Δy decreases, the value of the ductility factor increases, leading to an increased perception of ductility. A detailed discussion of this anomaly and its implications is provided in the following discussion section.

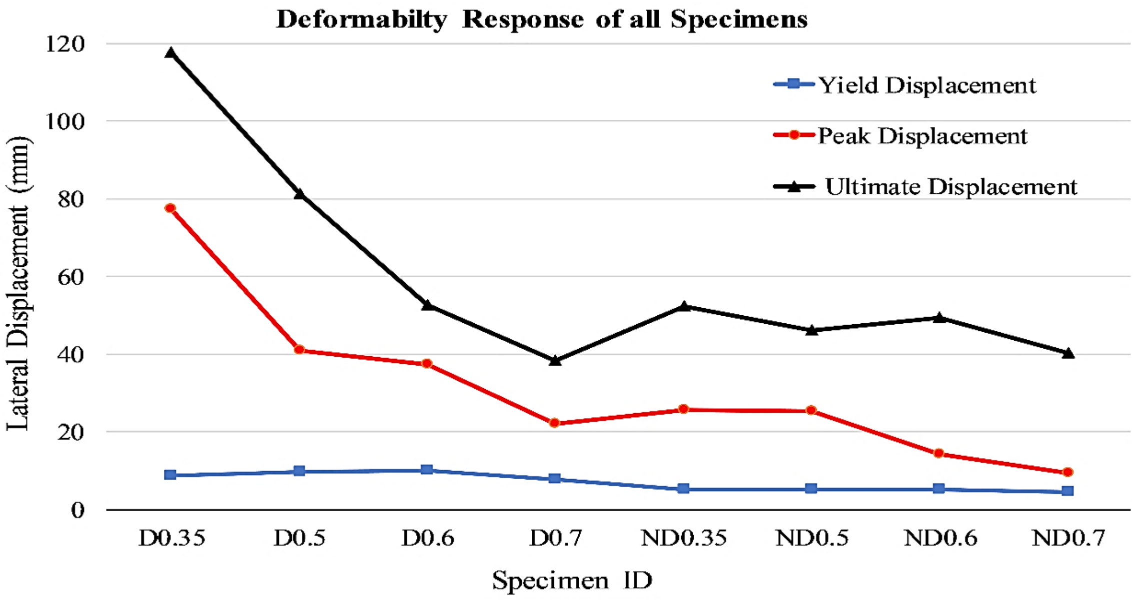

Fig. 3. 14 Deformability Response of all Specimens

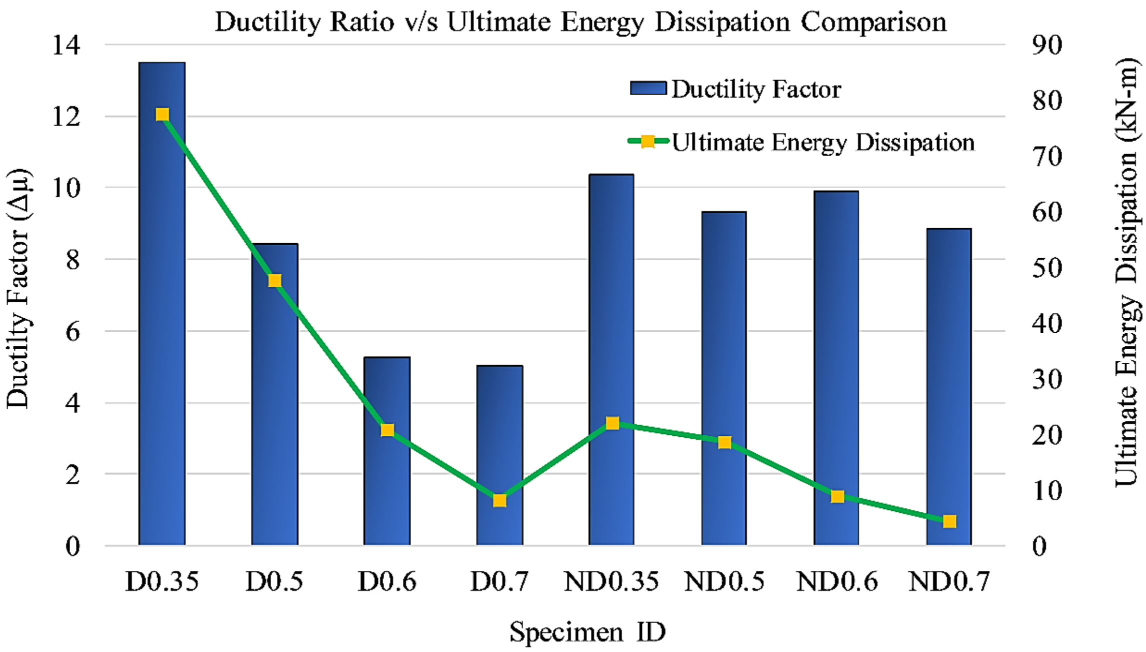

Fig. 3. 15 Ductility Characteristics of all Specimens

3.3 Discussion

3.3.1 Effect of ACR and Amount of Lateral Reinforcement on 'Pre-Peak Response Domain'

3.3.1.1. Ductile Columns

The structural response of the eight numerical models examined in this study is summarized in Table 3. 1 Among these models, the column specimen with ductile reinforcement and an axial compression ratio of $0.35P_0$, denoted as 'D0.35' was selected as the control specimen. The control specimen exhibited an initial stiffness (K_0), corresponding to the first loading cycle, of 10.3 GPa and achieved a peak flexural strength of 111.74 kN. When axial load was increased by 43% in specimen D0.5 (while maintaining the same reinforcement configuration as the control), the flexural strength improved by approximately 7%.

A further increase in ACR resulted in specimen D0.6, which experienced a 71.5% higher axial load than the control, producing 14.12% greater flexural strength. This increase in flexural strength can be attributed to the higher lateral forces required to deform columns subjected to higher axial compressive loads. As axial compression levels rise, the column's resistance to lateral deformation strengthens, which explains the observed increase in flexural strength. However, at even higher axial compression levels, a significant drop in flexural strength was observed. For example, specimen D0.7, subjected to twice the axial compression as the control specimen (a 100% increase), exhibited an 11% reduction in flexural strength. This reduction is due to the increased influence of secondary stresses caused by the P-Δ effect at higher axial loads. The P-Δ effect refers to the moment generated by the multiplication of axial compression and lateral displacement, which acts in the same direction as the moment induced by lateral forces. At elevated axial compression levels, the contribution of the P-Δ moment becomes more pronounced, leading to a degradation in the pre-peak behaviour of the column. This degradation manifests in column buckling, concrete crushing, and a sudden decline in structural strength.

An important observation is that the detrimental impact of increased axial compression on the pre-peak response is not limited to specimen D0.7, which showed a clear reduction in flexural strength, but also extends to specimens D0.5 and D0.6. Although these specimens appeared to benefit from an increase in flexural strength, their pre-peak behaviour was negatively affected by axial compression. For instance, while the control specimen (D0.35) reached its peak response at a drift level of 5.1%, specimens D0.5, D0.6, and D0.7 reached their peak responses at much lower drift levels—2.7%, 2%, and 1.5%, respectively. This indicates a significant reduction in deformability as axial compression increases. When comparing the deformability results, it becomes clear that a 43% increase in axial compression (D0.5) led to a 7% increase in flexural strength but also caused a 47% reduction in deformability (Δ_p). Similarly, specimen D0.6, with a 71.5% higher axial load, achieved 14.12% more flexural strength but suffered a 61.9% reduction in deformability. Specimen D0.7, which experienced a 100% increase in axial compression, showed an 11% reduction in flexural strength and a 71.6% decrease in deformability.

In summary, increasing ACR levels may enhance or reduce the flexural strength of RC columns depending on the load level. However, one consistent outcome of increasing axial compression is a significant reduction in deformability. This reduction in deformability triggers a premature post-peak response, which has a detrimental impact on the seismic performance of the structure. Columns subjected to higher axial loads are more prone to brittle failure, compromising their ability to sustain lateral deformations and withstand seismic forces effectively.

3.3.1.2. Non-Ductile Columns

The non-ductile specimens were found to experience even more severe degradation under increased ACR levels compared to their ductile counterparts. The non-ductile specimen (ND0.35), which was subjected to ACR levels similar to the control specimen (D0.35), demonstrated comparable initial stiffness but exhibited approximately 10% lower flexural strength. This reduction in flexural strength can be primarily attributed to the premature buckling of the longitudinal reinforcement bars, a consequence of the sparse placement of lateral reinforcement (spaced 300mm apart). This observation aligns with findings from previous studies by (Saatcioglu M & Ozcebe G, 1989) which highlighted the adverse effects of inadequate lateral confinement on the flexural performance of columns.

In addition to reduced flexural strength, the deformability of specimen ND0.35 was significantly compromised. Specifically, it exhibited a 67% reduction in peak displacement and a 17.2% decrease in yield displacement compared to the control specimen. As ACR levels continued to increase, all non-ductile columns exhibited a consistent decline in both flexural strength and deformability. For instance, specimen ND0.5 showed a 22% reduction in flexural strength and a 38% reduction in deformability compared to its ductile counterpart (D0.5). When evaluated against the control specimen (D0.35), ND0.5 experienced a 16.4% reduction in flexural strength and a dramatic 67.2% decrease in deformability.

Similarly, non-ductile specimens ND0.6 and ND0.7 showed significant reductions in deformability when compared to their ductile counterparts (D0.6 and D0.7). Specifically, ND0.6 exhibited a 52% reduction in deformability, while ND0.7 showed a 59% reduction. When compared to the control specimen, the deformability reductions were even more pronounced, with ND0.6 and ND0.7 showing 82% and 89% lower deformability, respectively, as illustrated in Fig. 3. 14. This substantial decline in deformability highlights the serious implications of insufficient ductile detailing in columns, particularly when subjected to higher axial compression levels. The absence of adequate lateral confinement leads to premature failure mechanisms, such as the buckling of longitudinal bars and crushing of concrete, which severely undermine the columns' ability to undergo large deformations without significant loss of strength. This finding underscores the critical importance of ductile detailing in ensuring the structural resilience of reinforced concrete columns, particularly in regions prone to seismic activity where columns are subjected to high axial loads and large lateral displacements.

3.3.2 Effect of ACR and Amount of Lateral Reinforcement on 'Post-Peak Response Domain'

3.3.2.1. Ductile Columns

The failure of specimens was defined as the point at which the load dropped to 85% of their peak flexural strength during the post-peak response, referred to as the 'Ultimate' point. As previously discussed, critical ductility parameters, such as the ductility ratio and cumulative envelope energy, were assessed at this stage. In earlier sections, it was observed that an increase in ACR levels led to a reduction in the deformability of columns. This trend continued into the post-peak region, where the effects on ultimate displacement and other structural parameters were observed.

For the control specimen, the ultimate displacement was recorded at 117.75 mm, corresponding to approximately a 7.8% drift level. This specimen exhibited a ductility factor of 13.48 and a cumulative envelope energy (E_u) of 77.52 kN-m. However, as ACR levels increased, significant reductions were observed in both ultimate displacement and ductility indicators across the specimens. For instance, specimen D0.5, which was subjected to 43% higher axial compression but maintained the same reinforcement configuration as the control specimen, experienced a substantial 31.2% reduction in ultimate displacement. In addition, this specimen showed a 38.5% decrease in cumulative envelope energy and a 51.5% drop in the ductility factor compared to the control specimen. Similarly, specimen D0.6, with an even greater axial load, exhibited a nearly 60% reduction in ultimate displacement, a dramatic 73% decrease in cumulative energy, and a 67% decline in its ductility factor. Specimen D0.7, subjected to the highest axial compression in the study, also followed the same trend. It experienced a 67.6% reduction in its ultimate displacement, a nearly 70% drop in its ductility factor, and a massive 90% reduction in cumulative energy.

These results underscore the detrimental effects of increased axial compression levels on the post-peak behaviour of reinforced concrete columns. As axial loads rise, the ability of the columns to sustain deformations and dissipate energy diminishes significantly. The drastic reductions in ductility and cumulative energy observed in specimens subjected to higher axial compression highlight the importance of carefully considering axial load levels in the design and detailing of columns, especially in regions susceptible to seismic events. This ensures that the columns can maintain adequate deformability and energy dissipation capacity, which are crucial for structural resilience during and after peak loading conditions.

3.3.2.2. Non-Ductile Columns

The non-ductile columns exhibited similar qualitative trends when analyzed for their post-peak behaviour under varying ACR. These columns, which inherently had lower ductility due to the absence of proper reinforcement detailing, were further compromised as ACR levels increased. For instance, specimen ND0.35, which had axial compression levels equivalent to the control specimen, demonstrated a 47.2% reduction in ultimate displacement, a 36.3% lower ductility factor, and a significant 71.5% decrease in cumulative energy dissipation. As the axial compression was increased, the non-ductile specimens suffered even more severe degradation.

Specimen ND0.5, subjected to 43% higher axial compression than the control, experienced a 59% reduction in ultimate displacement, a 55.4% decline in ductility factor, and a 72% decrease in cumulative energy. This downward trend persisted for specimens ND0.6 and ND0.7, where the higher axial loads led to further reductions in structural performance. Specifically, ultimate displacement was reduced by 69% and 75% for specimens ND0.6 and ND0.7, respectively, consistent with earlier observations.

Interestingly, despite these severe reductions in ultimate displacement, the ductility factor for ND0.6 and ND0.7 was found to be marginally better than that of ND0.5. This apparent anomaly is attributed to the sharper reduction in yield displacement in these two specimens compared to ND0.35 and ND0.5, where the yield displacement reduction was more gradual. This highlights the limitation of the ductility factor as an indicator, as it can sometimes yield misleading results in certain conditions. In contrast, the cumulative energy parameter consistently showed a more reliable measure of post-peak response, with reductions of 76%, 88.3%, and 94.2% in cumulative energy for specimens ND0.5, ND0.6, and ND0.7, respectively.

A notable observation emerges when comparing the ductility characteristics of ductile columns at high ACR levels with non-ductile columns at lower ACRs. Ductile columns, despite being designed to exhibit superior deformability, sometimes performed comparably or even worse than non-ductile columns when subjected to higher axial compression. For instance, ductile columns with an ACR of $0.6P_0$ and $0.7P_0$ exhibited significantly lower ductility performance than non-ductile columns under moderate compression, such as ND0.35.

This trend is particularly evident when comparing the ultimate displacement and energy dissipation. For example, ductile columns with an ACR of $0.7P_0$ had 39% lower ultimate displacement, 53% lower ductility factor, and 61% less energy dissipation compared to the non-ductile specimen ND0.35, which was subjected to moderate axial compression. These findings suggest that while ductile reinforcement detailing generally improves performance, its effectiveness can be severely compromised under high axial compression, underscoring the importance of accounting for axial load levels in design to ensure reliable post-peak and seismic performance.

3.4 Conclusions

A comprehensive parametric study was undertaken to evaluate the effects of varying ACR on the seismic performance of ductile and non-ductile RC columns. The findings underscore the need for revisions in current design guidelines to better align with the performance demands of contemporary building standards. Several critical observations can be drawn from this study:

1. Both ductile and non-ductile columns exhibited substantial reductions in strength, deformability, and ductility as ACR levels increased. Notably, the decline in ductility indices, particularly energy dissipation, was found to be 5 to 7 times greater than the reduction in strength. This highlights the greater vulnerability of columns to ductility loss under elevated axial loads compared to strength degradation.

2. Increased ACR levels significantly compromised pre- and post-peak response behaviours, leading to earlier peak responses. As a result, columns, regardless of their ductile detailing, may enter the post-elastic failure phase at lower drift levels when subjected to higher ACRs. This indicates that conventional performance-based safety criteria, typically assessed by drift levels, may not be fully applicable in scenarios involving high ACRs.

3. An increase in ACR from $0.35P_0$ to $0.6P_0$ resulted in a 14.34% increase in flexural strength. However, further increasing the ACR to $0.7P_0$ led to premature buckling, accompanied by concrete crushing, significantly reducing the column's strength. This suggests that while moderate increases in ACR can enhance strength, excessive axial loads can trigger sudden structural failures.

4. Non-ductile columns were found to be more adversely affected by higher ACRs than their ductile counterparts. However, an intriguing observation was made when comparing the ductility performance of ductile columns at high ACR levels with non-ductile columns at lower ACR levels. Ductile columns, designed to exhibit superior ductility characteristics, actually performed worse than non-ductile columns under moderate axial loads. This indicates that the benefits of ductile detailing diminish as ACR levels rise, challenging the conventional assumption of the superiority of ductile columns in all scenarios.

5. Energy dissipation emerged as a more reliable measure of post-peak response, demonstrating a consistent trend across specimens. In contrast, the ductility factor, which is inversely related to pre-peak behaviour, sometimes yielded misleadingly higher values due to the severe damage experienced by weaker specimens. For example, non-ductile specimens with elevated ACR showed an increase in the ductility factor due to a drastic reduction in yield displacement, which serves as the denominator in ductility ratio calculation.

The study's findings stress the critical importance of considering ACR levels when designing confining reinforcement, especially for structures exposed to seismic activity. To ensure adequate ductile detailing and seismic resilience, it is essential to incorporate axial load considerations into design calculations. Furthermore, the application of external strengthening measures, particularly in the hinge regions of columns, becomes crucial when these structures are subjected to high ACRs.

Chapter 4

Seismic Response Assessment of Ductile and Non-ductile Reinforced Concrete Columns Affected by Corrosion and Axial Load Variations

4.1 Introduction

The present chapter extends the scope of the study by incorporating the impact of an additional variable, i.e. corrosion levels. This new variable is examined alongside those previously discussed, namely ACRs and lateral reinforcement configurations. By integrating corrosion levels, the chapter provides a more holistic understanding of how these factors collectively influence the seismic response of RC columns.

Reinforcement corrosion is widely regarded as one of the primary causes of premature deterioration and aging in RC structures across the globe. Through our extensive field investigations, we identified several contributing factors that accelerate corrosion in RC structures, including substandard construction practices, the use of defective or poor-quality materials, exposure to harsh environmental conditions, and inadequate maintenance. These issues lead to the initiation and progression of corrosion, which substantially undermines the structural integrity of RC systems.

Specifically, corrosion reduces the mechanical properties and cross-sectional area of embedded steel reinforcement bars (rebars), as suggested by numerous researchers such as (Clark et al., 2005; Kashani et al., 2015; H. S. Lee & Cho, 2009; Ou et al., 2016). As corrosion advances, it not only diminishes the effective cross-sectional area of the rebars but also generates expansive iron oxide products commonly known as Rust. This rust expansion causes cracking and spalling of the surrounding concrete cover, further weakening the structure as explained by (Cabrera, 1996; Capozucca, 1995; Palsson & Mirza, 2002). Furthermore, the combined loss of both rebar and concrete cross-sections severely impairs the durability and structural performance of RC members (Bru et al., 2018; Çağatay, 2005; Dizaj et al., 2018; Ge et al., 2020; Qu et al., 2021).

Several studies have explored the structural response of corroded ductile RC columns under monotonic compression, revealing significant reductions in strength and post-peak behaviour due to corrosion (C. Lee et al., 2000; Revathy et al., 2009). For example, (X. H. Wang & Liang, 2008) highlighted the catastrophic risks posed by corrosion to the load-bearing capacity of structures, noting that increasing corrosion rates make structures more vulnerable, even under normal axial or gravity loads. (Yang et al., 2016) conducted experimental tests on five square RC columns to examine the impact of different corrosion levels on the column's seismic performance. Their results indicated that up to 13.25% corrosion, there was no significant decline in flexural strength.

However, at a corrosion level of 16.28%, the columns experienced a sharp 20% reduction in flexural strength.

Furthermore, (D. Li et al., 2018) extended this analysis to cyclic loading tests on six damaged RC columns, considering non-uniform corrosion of the reinforcement. Their findings revealed that non-uniform corrosion significantly affects the post-peak behaviour of columns, with flexural strength reductions of 8.94%, 12.10%, and 13.68% at corrosion levels of 11.49%, 16.8%, and 19.7%, respectively. An interesting study by (Yuan et al., 2018) which demonstrated through shaking table experiments that the corrosion in bridge columns can alter the natural period and damping ratio, amplifying the dynamic response of the structure.

When we inspect the non-ductile corroded columns, it is observed that due to distantly spaced lateral stirrups, these columns frequently experience premature concrete crushing, longitudinal bar buckling, and consequent degradation in axial load-carrying capacity when subjected to seismic forces (Paultre & Légeron, 2008; Qu et al., 2021; Sakai K & Shamim A, 1989). Numerous studies were conducted to assess the performance of corrosion-damaged non-ductile structural elements under seismic loads. In this context, (Ou & Nguyen, 2016) explored the influence of corrosion location on the seismic behaviour of columns. Their findings demonstrated that the location of reinforcement corrosion plays a pivotal role in altering the failure mode of the Columns. To further investigate this phenomenon, (Kashani et al., 2015) analyzed the cyclic behaviour of corroded reinforcement bars and discovered that corrosion significantly affected the buckling characteristics of the rebars under cyclic loading. Specifically, the tension-induced fracture of corroded rebars occurred prematurely after compression-induced buckling, even though the bars were designed in compliance with code provisions.

Additionally, (Ma et al., 2012) examined the seismic performance of non-ductile columns with varying degrees of reinforcement corrosion and ACR. Their results showed that higher levels of corrosion led to a marked deterioration in both ductility and stiffness. Specifically, flexural strength reductions of 9.3% and 14.7% were observed at corrosion levels of 10.82% and 18.16%, respectively. A related study assessed the impact of corroded longitudinal bars on the non-ductile corroded square columns. The results indicated a substantial 20% reduction in lateral load-carrying capacity and a 50% decrease in displacement capacity at approximately 20% corrosion levels (Lavorato et al., 2020).

During our multiple field investigations, we observed a common phenomenon that even the columns that were designed and constructed according to modern seismic design standards such as (IS-13920: 2016), were affected by severe corrosion (>15%) and their ductility is affected.

For clarity, Fig. 4. 1 shows an example of such a column, which, despite meeting ductility requirements, exhibited extensive corrosion damage. Although these columns were theoretically expected to possess adequate strength and ductility, corrosion degradation severely compromised their seismic and structural performance.

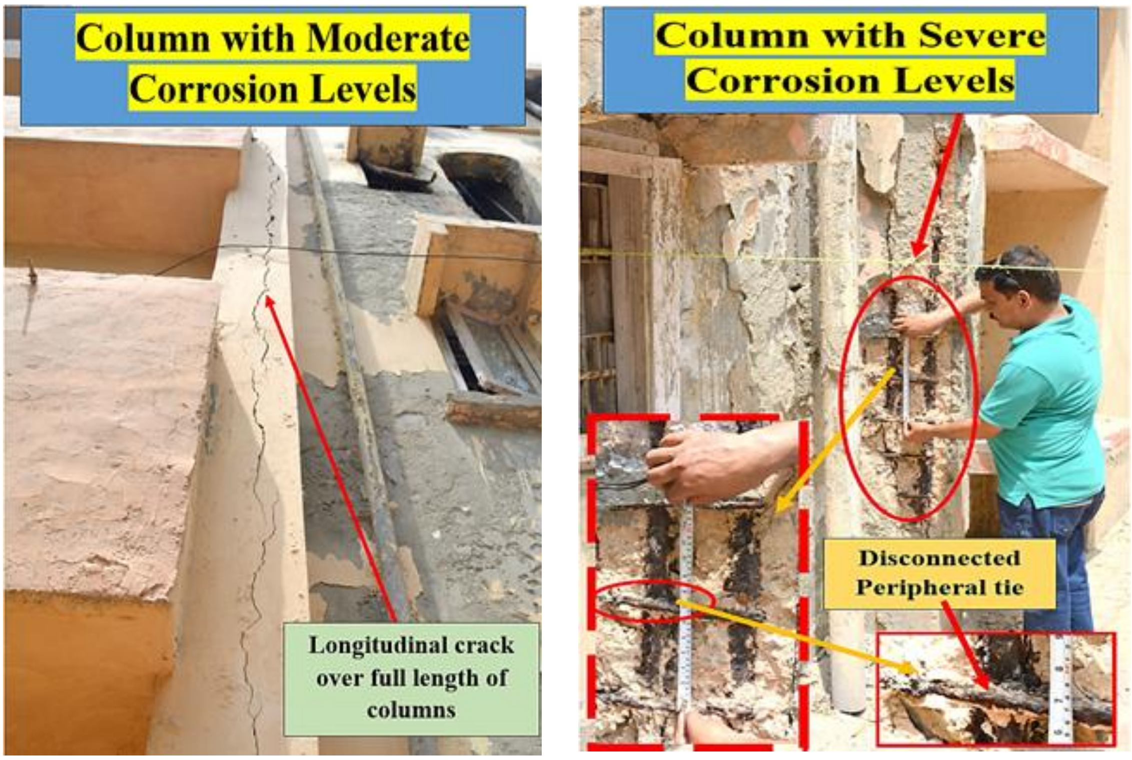

Fig. 4. 1 Visuals of Ductile RC Columns with Severe Corrosion Levels Observed During our Field Visit

Another critical factor influencing the seismic response of columns is the axial load they experience during service. This load is commonly represented by the ACR, which is the ratio of the applied load to the maximum theoretical capacity of the column. The importance of ACR is well-documented in previous research, which shows that it significantly affects the seismic behaviour and failure mechanisms of both uncorroded columns (Anh Huy et al., 2022) and corroded columns (Dai et al., 2021). This factor is so crucial that it is explicitly considered in major design codes, such as (New Zealand Standard, 2006) and (Canadian Standards Association, 2004), which adjust the required lateral reinforcement based on the ACR levels.

Our current work builds upon these prior efforts, aiming to comprehensively evaluate the combined effects of various corrosion and ACR levels on the seismic performance of ductile RC columns. The accuracy of numerical models in predicting these behaviours largely depends on the material properties and the bond/interface characteristics between the steel reinforcement and the surrounding concrete. Earlier studies have significantly contributed to developing models that assess material (Coronelli & Gambarova, 2004) and steel-concrete bond degradation (Bhargava et al., 2008; Stanish, 1997; Vu et al., 2016; Zhang et al., 2020) caused by corrosion.

These insights were utilized by (Maaddawy et al., 2005) to evaluate the maximum bond strength of corroded reinforcement. In particular, we employed the Traction-separation law in Abaqus to model the bond behaviour between corroded steel and concrete. To enhance the model's accuracy, stiffness coefficients were calculated for the normal, shear, and tangential directions, and internal stresses resulting from rust expansion were also incorporated. These refinements ensure that our numerical models can more precisely simulate the degradation mechanisms in corroded RC columns, offering improved predictive capabilities for their seismic performance.

4.1.1 State of Knowledge

This part of our research emphasizes the critical influence of reinforcement corrosion and ACR on the seismic performance of RC columns i.e., both ductile and non-ductile. Reinforcement corrosion reduces the cross-sectional area and mechanical properties of steel rebars while inducing cracking and spalling of concrete cover through the expansive formation of rust. This degradation compromises the structural integrity and load-bearing capacity of RC columns.

For ductile RC columns, corrosion creates major challenges for the structures built as per modern seismic standards. Despite their intended robustness and confinement provided by closely spaced lateral reinforcement, these columns can still experience significant performance degradation when subjected to moderate or severe corrosion. Field investigations reveal that even well-designed ductile columns often suffer from reduced structural performance, indicating a need for targeted retrofitting strategies to restore their resilience. In contrast, non-ductile RC columns, commonly found in aged structures, are inherently more vulnerable. These columns typically lack sufficient lateral reinforcement, resulting in poor confinement and inadequate ductility. When affected by corrosion, non-ductile columns exhibit premature failure modes, such as longitudinal bar buckling, concrete crushing, and significant reductions in lateral load-carrying capacity.

Hence, this research underscores the importance of evaluating the combined effects of corrosion and ACR on both ductile and non-ductile RC columns. While ductile columns require enhanced retrofitting measures to mitigate corrosion-related degradation, non-ductile columns demand urgent intervention due to their inherent seismic deficiencies. Advancing this knowledge is crucial for developing effective design modifications and retrofitting strategies to improve the seismic resilience of RC structures under real-world conditions.

4.1.2 Research Significance

Accurately quantifying the gap between the desired and actual seismic response is essential to develop effective retrofitting strategies for deteriorated structures. This study addresses this critical need by focusing on both ductile RC columns, typically assumed to provide sufficient seismic performance, and non-ductile RC columns, which lack adequate seismic detailing. It examines the cumulative effects of reinforcement corrosion and ACR, two key factors influencing structural vulnerability.

For ductile RC columns designed to modern seismic standards, the research highlights how varying degrees of corrosion and ACR significantly impact their seismic behaviour, often undermining the expected performance. The study provides a comprehensive parametric analysis to identify optimal ACR ranges for these columns by combining experimental and numerical approaches. The findings emphasize the need for revisions in global seismic detailing standards, including those in India, to address the effects of ACR and corrosion on ductile reinforcement design effectively.

In contrast, for non-ductile columns, the study systematically quantifies seismic performance degradation due to moderate to severe corrosion under varying ACR conditions. These columns, often found in older structures, are characterized by insufficient confinement and poor ductility due to inadequate lateral reinforcement. The research evaluates critical response parameters, revealing reductions in strength, ductility, and failure patterns. Such insights are crucial for developing tailored retrofitting strategies to mitigate the seismic vulnerability of non-ductile columns.

By addressing these gaps, the research represents a significant contribution to the field, providing valuable data for structural engineers and retrofitting experts. It advances the understanding of how corrosion and ACR collectively influence the seismic performance of both ductile and non-ductile corroded RC columns, paving the way for more effective repair and retrofitting solutions.

4.1.3 Research Methodology

4.1.3.1 Specimen Details

To investigate the influence of ACR on the structural behaviour of RC columns, twelve ductile corroded and eight non-ductile corroded 3D FE models were developed. These models were subjected to ACR levels of $0.35P_0$, $0.5P_0$, $0.6P_0$, and $0.7P_0$. Each column measured 1800 mm in height with a cross-section of 300 × 300 mm, while the base or joint was represented by a stub with dimensions of 1000 × 520 × 600 mm and a uniform concrete cover of 40 mm. Longitudinal reinforcement consisted of eight Ø16 mm (#8) bars, and lateral reinforcement arrangements differed according to ductility requirements. Ductile columns utilized closely spaced transverse reinforcement at 75 mm c/c, achieving a reinforcement ratio of 1.31%, whereas non-ductile columns incorporated widely spaced transverse reinforcement at 300 mm c/c, leading to a reduced reinforcement ratio of 0.33%. The plastic hinge region, extending 800 mm from the stub interface, was designated as primary test zone, as it is the most susceptible to damage during seismic events.

4.1.3.2 Study Variables

Three major variables were adopted, and they were divided into twenty 3D FE-developed models that were based on the column type. The first variable pertains to the degree of corrosion, expressed as a percentage. The second variable involves the spacing of lateral reinforcement, defined as 75 mm for ductile specimens and 300 mm for non-ductile specimens. The third variable is the axial compression ratio levels, analyzed at four distinct levels. Detailed specifications for these variables and a number of modeled specimens are provided in Table 4.1.

Table 4. 1 Types of Variables and Modelled Columns

Sr. No	Modelled Columns	Corrosion (%) (Variable 1)	Shear Reinforcement (Variable 2)	Axial Compression Ratio (Variable 3)	Total Modelled Columns
1	Ductile Corroded Columns	10	1.31 %	$0.35P_0$, $0.5P_0$, $0.6P_0$, $0.7P_0$	4
		15			4
		20			4
2	Non-Ductile Corroded Columns	15	0.33 %	$0.35P_0$, $0.5P_0$, $0.6P_0$, $0.7P_0$	4
		30			4

4.1.3.3 Calculations and Loading Protocol

For the modelling of all twenty FE specimens, fixed boundary conditions were applied at the base, while the symmetry and contact conditions at the steel-concrete bond interface were defined using the cohesive surface bonding method, as detailed in Section 2.6. During the simulations, the axial load was kept constant, and a quasi-static, incrementally increasing lateral displacement was applied to simulate seismic loading conditions. For example, one specimen was subjected to quasi-static seismic loading with an axial load of $0.35P_o$. Similarly, additional specimens were analyzed under the same seismic loading conditions with increased axial loads of $0.5P_o$, $0.6P_o$, and $0.7P_o$. The axial capacity of the column (P_o) and the seismic loading conditions are consistent across the specimens, with further explanation mentioned in Section 3.1.4.

4.2 Results of Ductile Corroded Column

A detailed parametric study was undertaken to investigate the combined influence of varying corrosion levels and ACRs on the seismic behaviour of ductile RC columns. All specimens shared uniform material properties, reinforcement detailing, interactions, lateral displacement history, and boundary conditions. The seismic performance of twelve numerical models was comprehensively analyzed and compared across various parameters. These parameters included hysteresis response, stiffness degradation, energy dissipation, envelope curves, equivalent viscous damping ratio, ductility factor, and deformability characteristics, providing an in-depth understanding of the corroded column’s behaviour under variable seismic loading conditions.

4.2.1 Hysteresis Response and Envelope Curves

The hysteresis responses of the twelve FE ductile models, representing 10%, 15%, and 20% corrosion levels at varying ACRs, are presented in Fig. 4. 2(a-d), Fig.4. 3(a-d), and Fig. 4. 4(a-d), respectively. Within the elastic range, the relationship between load and displacement remained linear and consistent across all specimens.

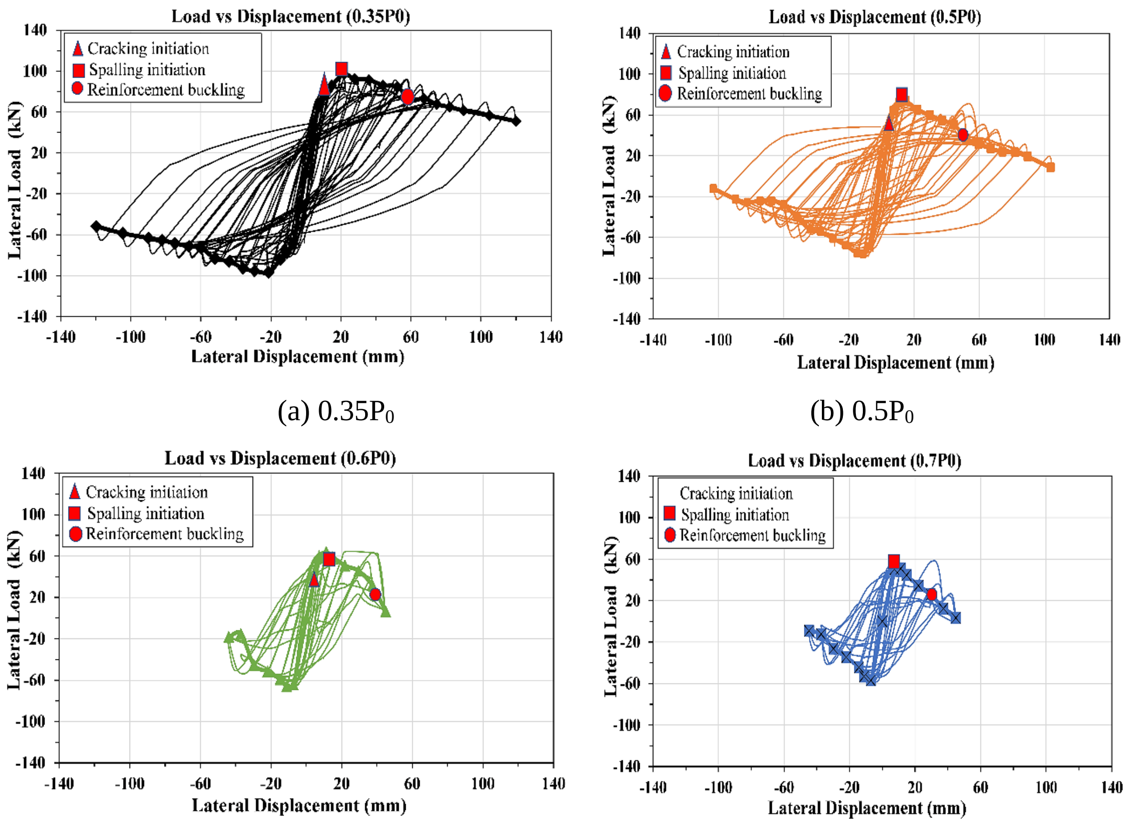

(a) $0.35P_0$

(b) $0.5P_0$

(c) $0.6P_0$

(d) $0.7P_0$

Fig. 4. 2 Hysteresis Curves of 10% Ductile Corroded Columns at Varying ACR Levels

However, as the seismic drift and ACR levels increased, the load-deflection behaviour exhibited significant changes. The plastic response of the structure was initiated by cracking in the concrete cover, signalling failure in the cover region. This process resulted in a reduction in stiffness and an expansion of the hysteresis loops, attributed to weaker unloading paths.

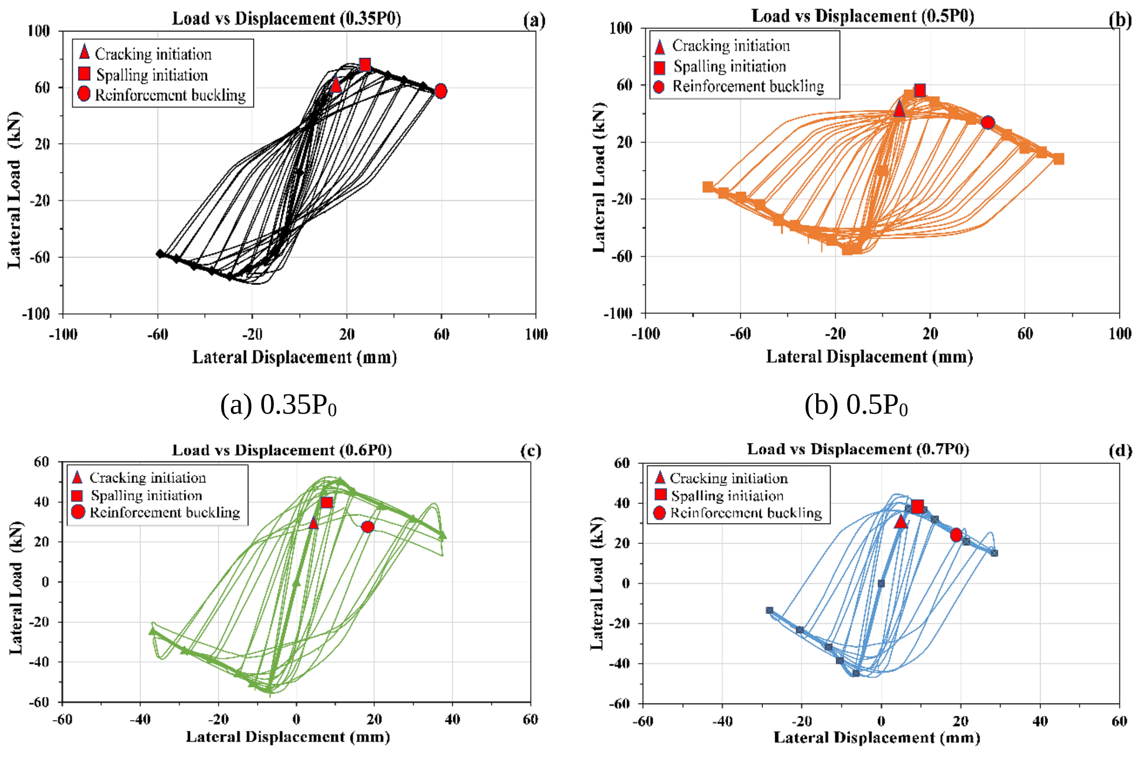

(a) $0.35P_0$ (b) $0.5P_0$

(c) $0.6P_0$ (d) $0.7P_0$

Fig. 4. 3 Hysteresis Curves of 15% Ductile Corroded Columns at Varying ACR Levels

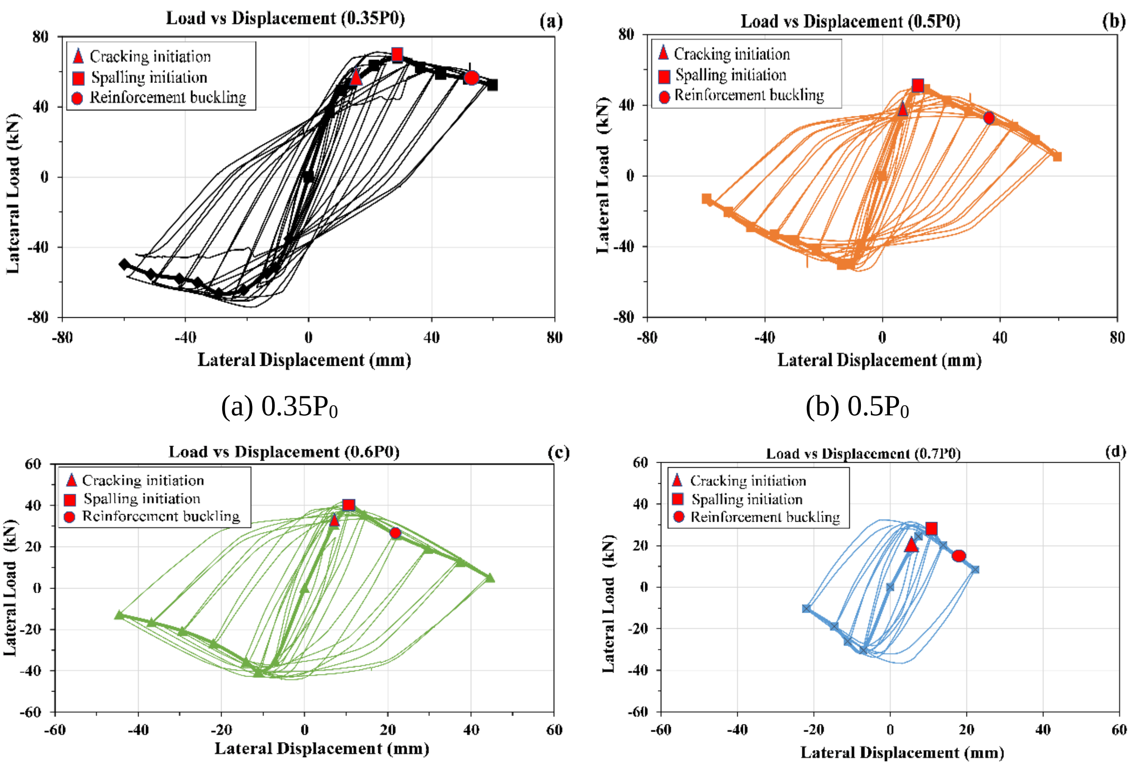

(a) $0.35P_0$ (b) $0.5P_0$

(c) $0.6P_0$ (d) $0.7P_0$

Fig. 4. 4 Hysteresis Curves of 20% Ductile Corroded Columns at Varying ACR Levels

As previously defined, the failure point occurred when the lateral load dropped to 85% of the peak load in the post-peak region. The tests were extended beyond this point to investigate the effects at higher drift levels further. Fig.4. 5(a-d) depicts the envelope curves for all columns under different corrosion levels.

Notably, increasing the ACR from $0.35P_o$ to $0.7P_o$ in control (non-corroded) specimens led to increased flexural strength up to $0.6P_o$, as observed and relates with the previous research by (Saatcioglu M & Ozcebe G, 1989). In contrast, all corroded models consistently showed reduced flexural capacity regardless of the corrosion level.

The data from these envelope curves provide a comparative analysis of the corroded columns, offering detailed insights into how increasing ACR affects their maximum strength and ductility. Additionally, it was observed that higher ACR levels significantly compromised the post-peak behaviour of all specimens, irrespective of the amount of transverse reinforcement.

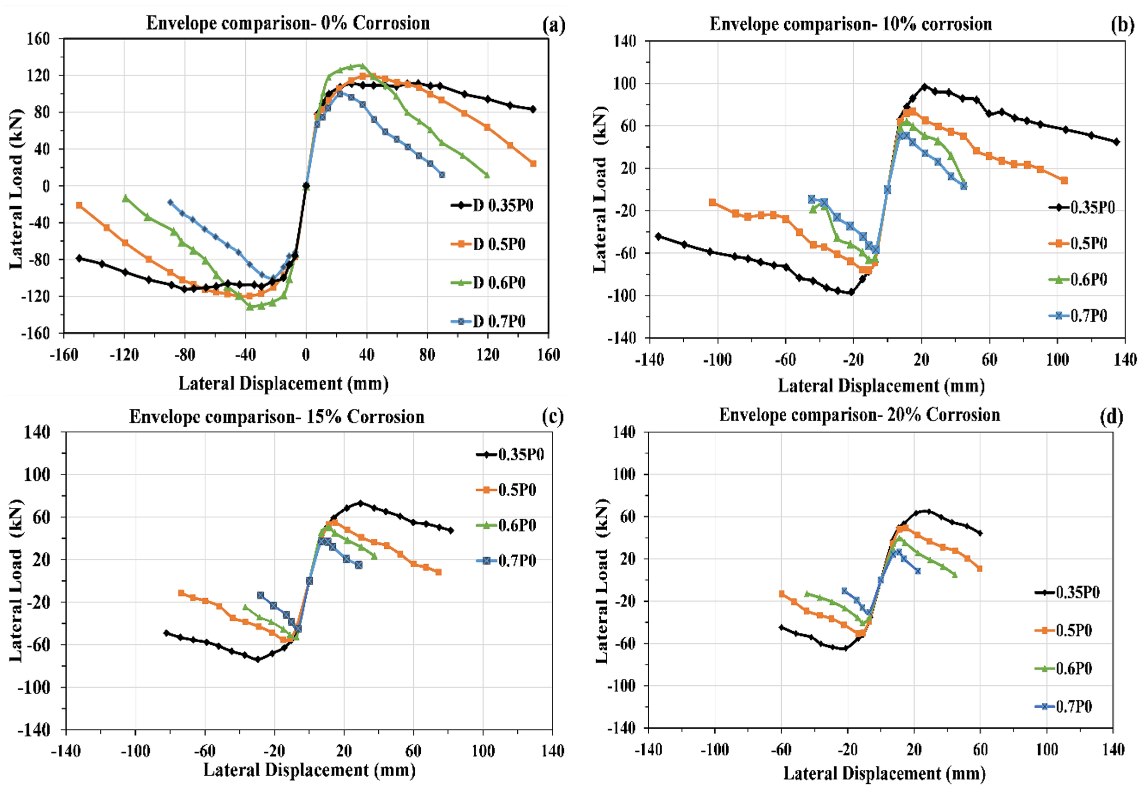

Fig. 4. 5 Envelope Profile of Columns at (a) 0%, (b) 10%, (c) 15% and (d) 20% Corrosion

4.2.2 Stiffness Deterioration

The secant stiffness (K_n) of a structure is a critical parameter for assessing both the magnitude and rate of structural degradation. It is determined by calculating the slope of the line connecting the peaks of the positive and negative cycles of a structure's response, as explained in previous section 3.2.2. Stiffness for each cycle was plotted against the corresponding lateral displacement, producing stiffness degradation curves. Several factors contribute to this degradation, including the reduction in cross-sectional area, deformation of longitudinal reinforcement under compression, and bond deterioration between steel and concrete. Fig 4.10 (a-d) explains the relationship between stiffness degradation and drift ratios in ductile columns at various corrosion levels.

An interesting observation is that, as ACR levels increased, the stiffness of the non-corroded (control) specimens initially increased up to $0.6P_o$, as shown in Fig 4. 6(a). Beyond this point, a marked decrease in stiffness was observed. In contrast, for corroded columns subjected to different ACR levels, the increase in ACR significantly accelerated the rate of stiffness degradation, regardless of the corrosion level. To provide further clarity, Fig 4. 7(a-d) compares ductile columns with equivalent ACR values but at different levels of corrosion.

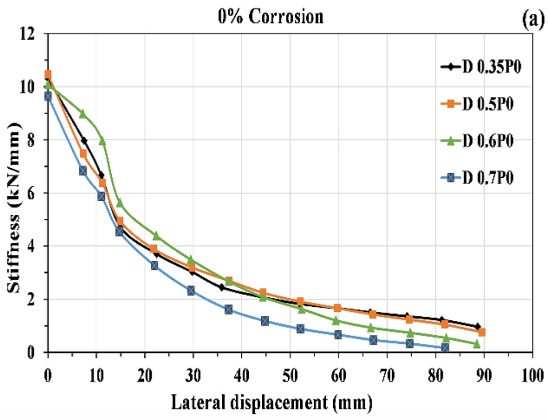

(a) 0% Corrosion

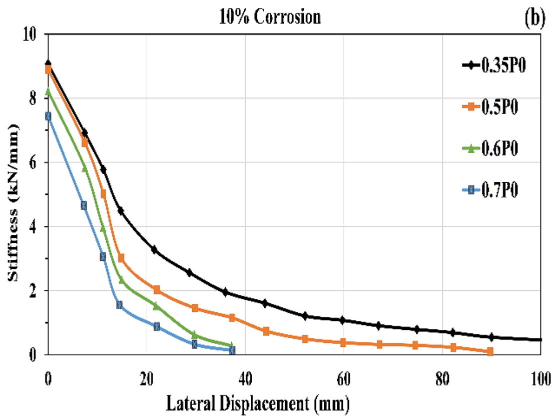

(b) 10% Corrosion

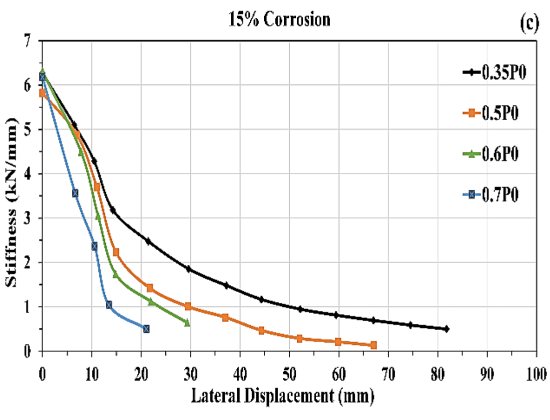

(c) 15% Corrosion

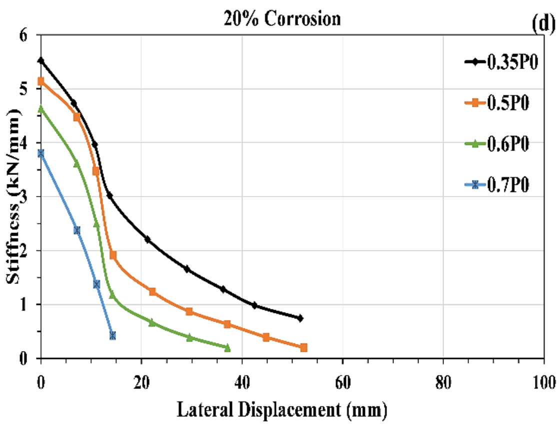

(d) 20% Corrosion

Fig. 4. 6 Stiffness Degradation of Columns at Various Corrosion Levels

Interestingly, when the ACR was set at $0.35P_o$, the stiffness degradation profiles for ductile columns exhibited similar trajectories, as shown in Fig. 4. 7(a). However, as the ACR increased, the differences in performance became more pronounced, regardless of corrosion level, as depicted in Fig. 4. 7 (b), (c), and (d) for ACR levels of $0.5P_o$, $0.6P_o$, and $0.7P_o$, respectively.

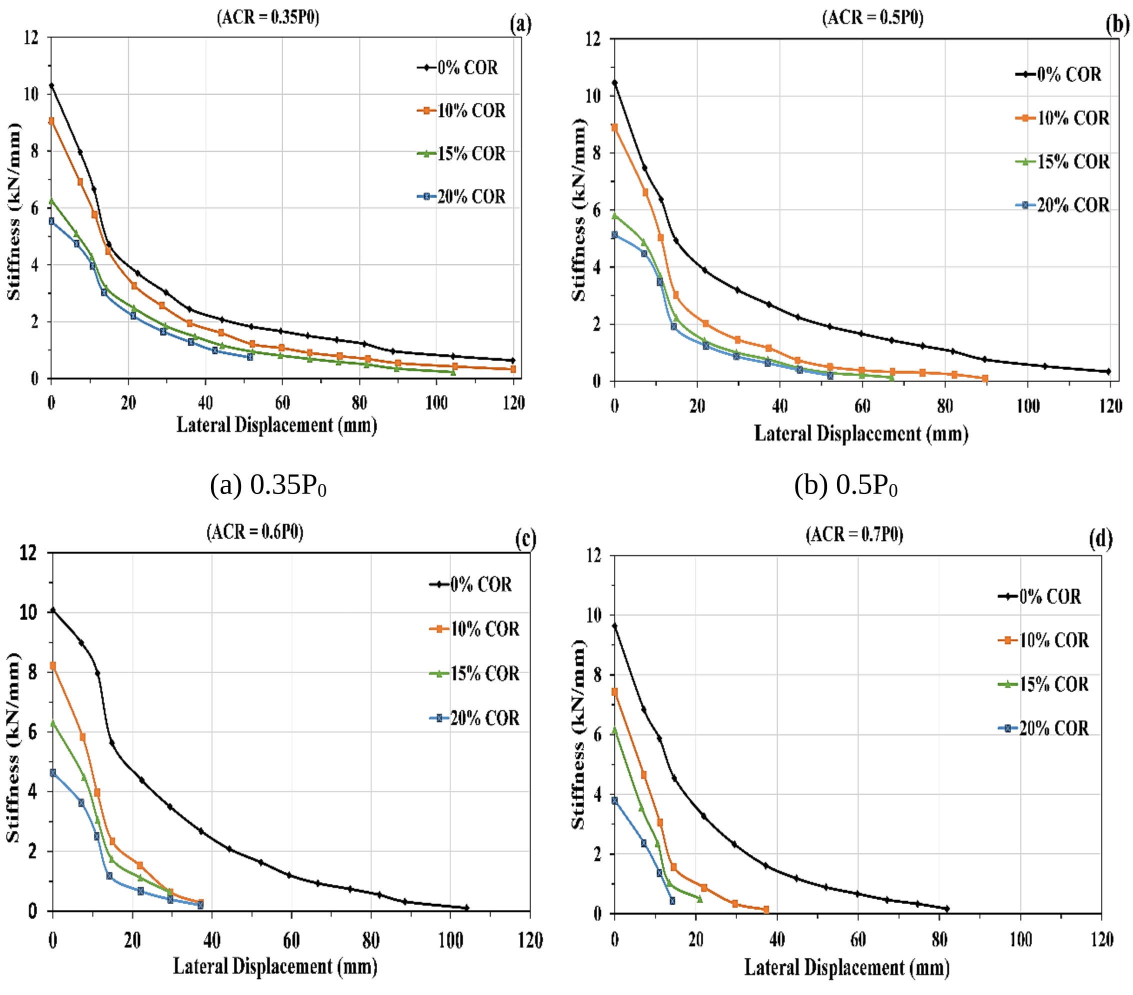

(a) $0.35P_0$ (b) $0.5P_0$

(c) $0.6P_0$ (d) $0.7P_0$

Fig. 4. 7 Stiffness Degradation of Columns at Constant ACR but Various Corrosion Levels

4.2.3 Energy Dissipation Capacity

The energy dissipated during each loading cycle was calculated by determining the net area under the envelope curve for the corresponding drift level, as explained earlier in Fig. 3. 9. This computation was carried out using MATLAB. The total energy dissipated up to a particular drift level was obtained by summing the energy from the current cycle with that of all previous cycles. Additionally, the cumulative energy dissipated up to the point of failure, defined as the point where the lateral load reduces to 85% of the maximum load ($0.85V_{max}$), also referred to as the ultimate cumulative energy dissipation (E_u), was calculated by summing the energy dissipation up to the ultimate response.

Fig. 4. 8 (a-d) present the cumulative energy distribution (in kN-m) as a function of lateral drift (in mm) for the tested column specimens. The analysis revealed that an increase in ACR levels resulted in a substantial reduction in the energy dissipation capacity of the columns. Specifically,

columns subjected to a load factor of $0.7P_o$ exhibited energy dissipation capacities less than half of these observed in specimens with a load factor of $0.35P_o$.

To further explore these findings, Fig. 4. 9(a-d) compares columns with the same ACR levels but different corrosion percentages, providing insights into the combined effects of ACR and corrosion on energy absorption capacities. It is particularly important to note that as the corrosion levels increased, there was a significant decrease in total energy dissipation, suggesting a weaker post-peak response.

Additionally, at identical ACR levels, the energy dissipation of the structure showed a sharp decline with increasing corrosion levels. This trend is clearly illustrated in Fig. 4. 9(a), (b), (c), and (d) for ACR values of $0.35P_o$, $0.5P_o$, $0.6P_o$, and $0.7P_o$, respectively, highlighting the adverse impact of corrosion on the structure's energy dissipation capacity.

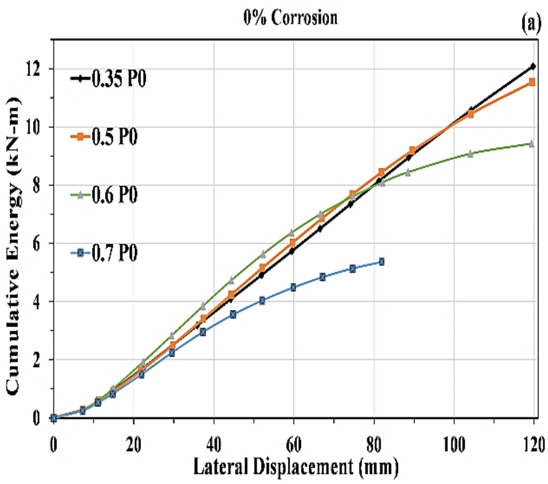

(a) 0% Corrosion

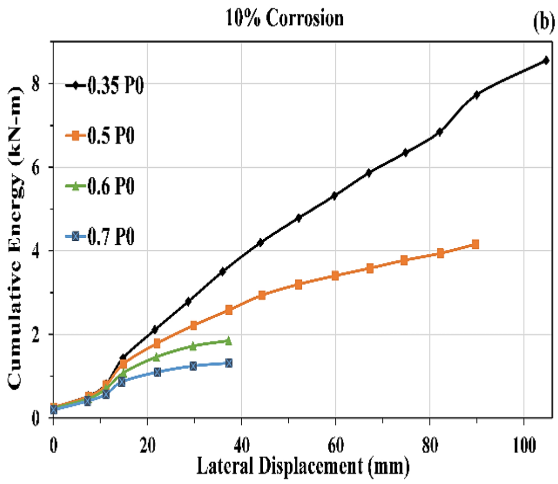

(b) 10% Corrosion

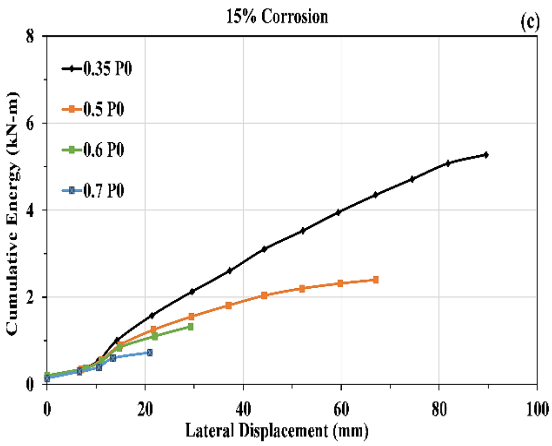

(c) 15% Corrosion

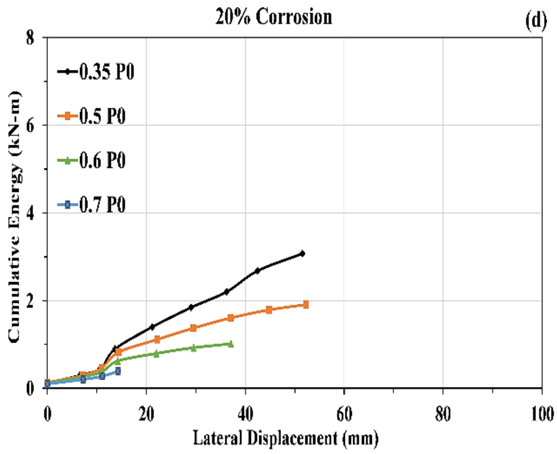

(d) 20% Corrosion

Fig. 4. 8 Cumulative Energy v/s Lateral Displacement for Ductile Columns at Varying Corrosion

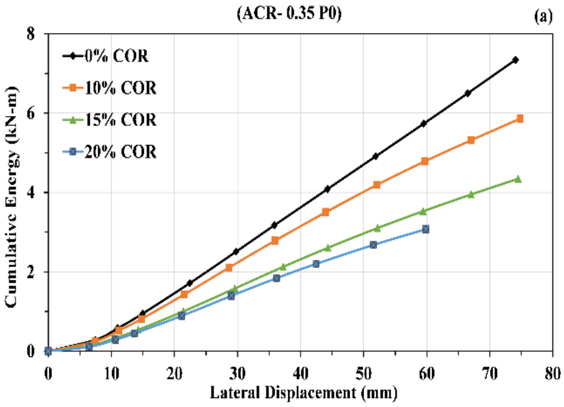

(a) $0.35P_0$

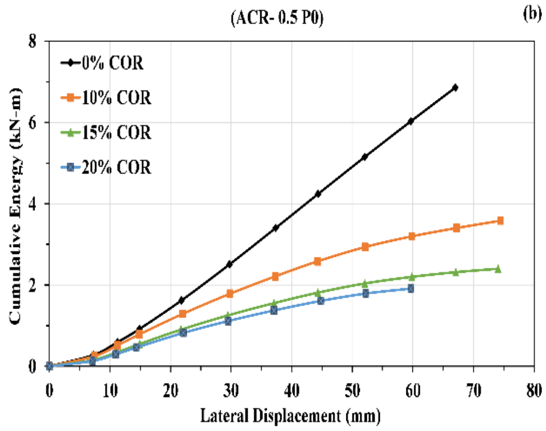

(b) $0.5P_0$

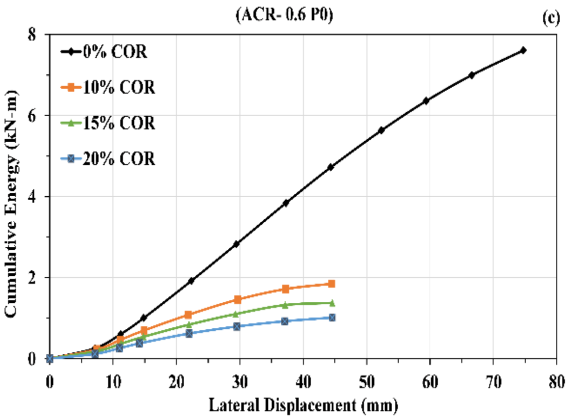

(c) $0.6P_0$

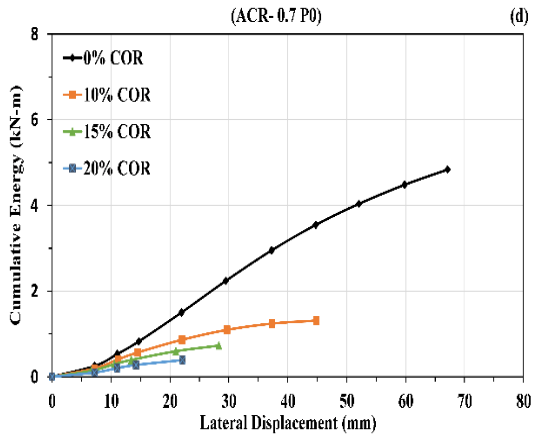

(d) $0.7P_0$

Fig. 4. 9 Cumulative Energy Comparison of Corroded Columns at Varying ACR Levels

4.2.4 Equivalent Viscous Damping Ratio

As explained earlier in section 3.2.4, the equivalent viscous damping ratio (ξ_{eq}) is a key parameter that quantifies the hysteretic energy dissipation of structural specimens under cyclic loading. The ξ_{eq} values for all twelve FE ductile models, subjected to varying corrosion levels and varying ACRs, are presented in Fig. 4 10(a-d). It can be observed that the non-corroded (control) specimens exhibited relatively consistent ξ_{eq} values prior to reaching their yield displacement, as shown in (a). However, as the corrosion levels increased, the ξ_{eq} values progressively rose, particularly at higher ACRs and lateral displacements.

This trend suggests that higher axial compression intensifies energy dissipation, which is reflected in the increased damping ratio. To further explore this impact, a comparative analysis was conducted where ACR values were kept constant, and the corrosion levels were varied, as detailed in Fig. 4. 11 (a-d). Interestingly, among all column specimens, those with an ACR of $0.35P_o$ demonstrated the lowest ξ_{eq} values, irrespective of their corrosion levels. However, as the ACR increased, there was a sharp rise in ξ_{eq} values when compared to specimens at same displacement levels. This steep increase is evident in Fig. 4. 11(b), (c), and (d), where ACR values of $0.5P_o$, $0.6P_o$, and $0.7P_o$, respectively, are shown. These observations reveal a direct relationship between increasing ACRs and rising ξ_{eq} values, indicating that greater axial loads leading to more energy dissipation through damping mechanisms. Conversely, an inverse relationship between ξ_{eq} values and the ductility of the specimens was noted. As the ξ_{eq} values increased, the ductility of columns was subjected to reduction, underscoring the trade-off between damping and ductility in corroded RC ductile columns.

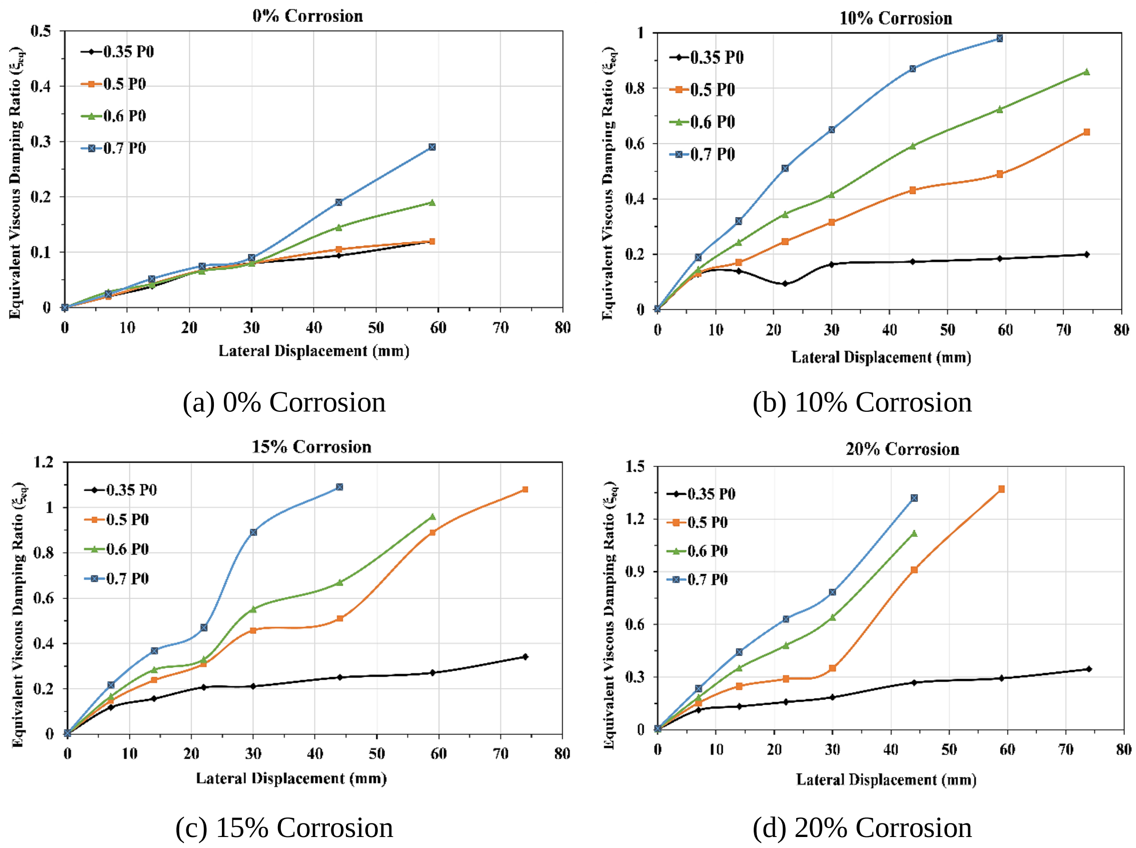

(a) 0% Corrosion (b) 10% Corrosion

(c) 15% Corrosion (d) 20% Corrosion

Fig. 4. 10 Equivalent Viscous Damping Ratio Comparison at Varying Corrosion Levels

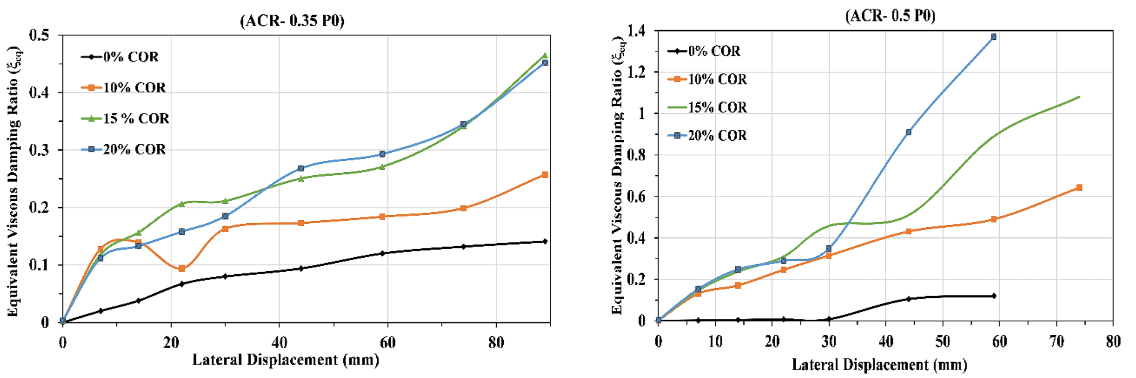

(a) $0.35P_0$ (b) $0.5P_0$

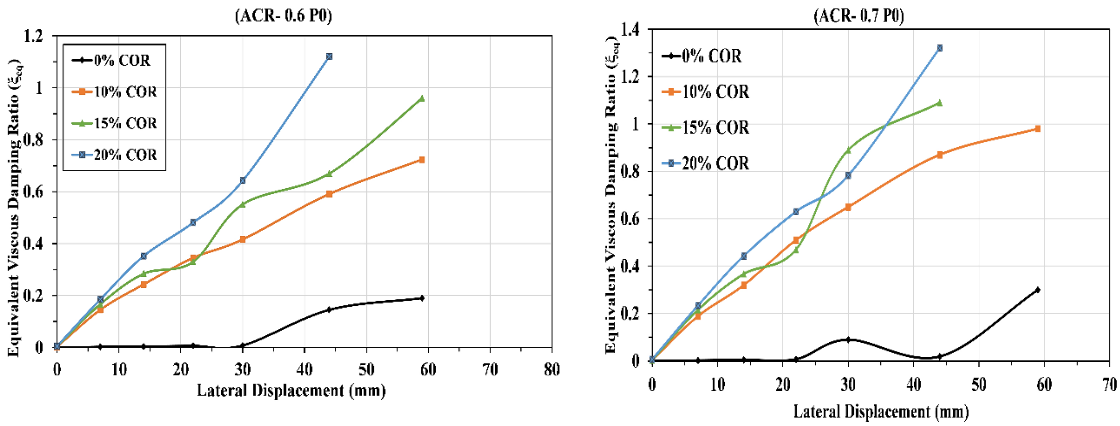

(c) $0.6P_0$ (d) $0.7P_0$

Fig. 4. 11 Equivalent Viscous Damping Ratio Comparison at Varying ACR Levels

4.2.5 Deformability and Displacement Ductility

As discussed in Section 3.2.5, the deformability characteristics of the column specimens were evaluated by identifying the points at which the load-deflection trajectory reached the yield, peak, and ultimate stages. It was observed that increasing the ACR levels had a significant influence on the deformability parameters in both the pre-peak and post-peak response trajectories of all corroded and control specimens. To provide a more detailed understanding, Fig. 4. 12 illustrates how the twelve corroded specimens, each subjected to different ACR levels, affected the yield, peak, and ultimate displacement values of the columns. The results clearly indicate that the rise in ACR had a pronounced negative effect on the deformability parameters, particularly the ultimate, peak and yield displacement, in both corroded and uncorroded specimens. Along with

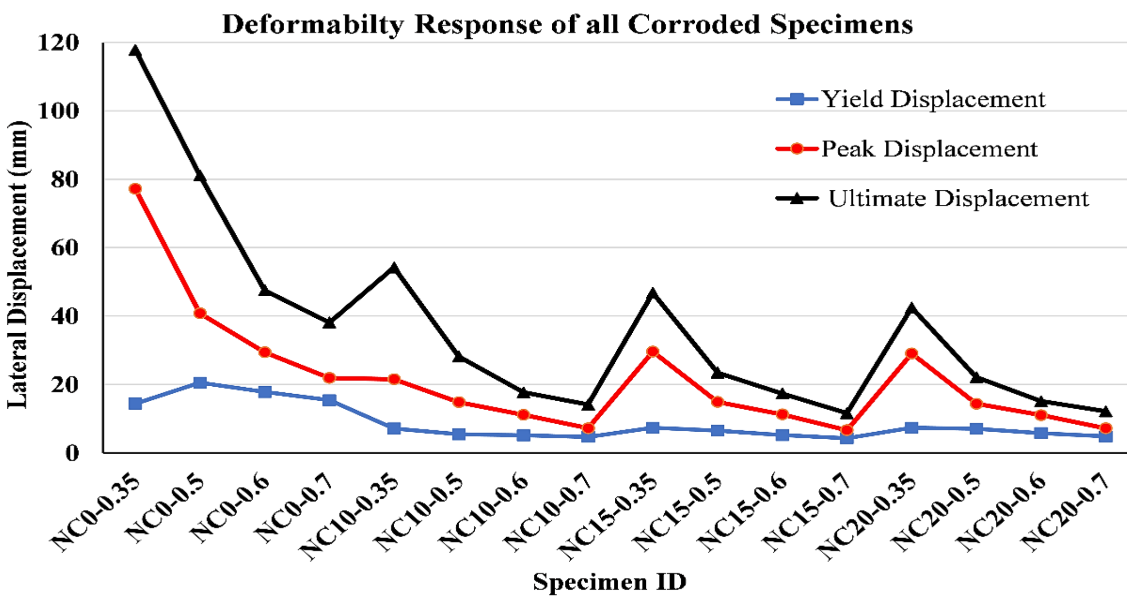

Fig. 4. 12 Deformability Response of Corroded Ductile Columns

deformability, the ductility characteristics of all sixteen FE specimens were analyzed using the ductility factor and ultimate cumulative energy dissipation (E_u).

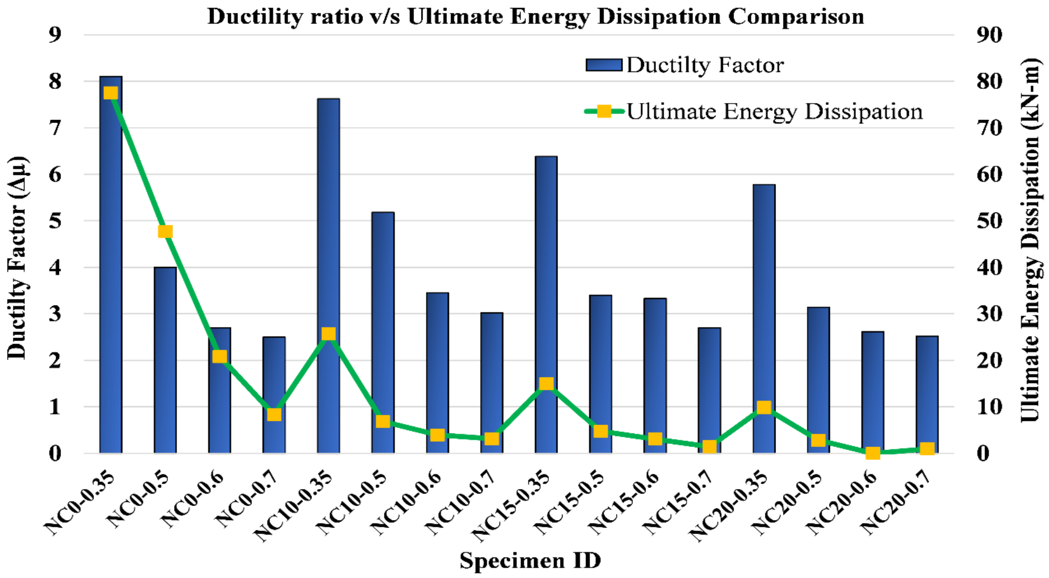

Fig. 4. 13 Ductility ratio v/s Ultimate Energy Dissipation Comparison of Corroded Columns

Table 4. 2 Summary of Seismic Performance of all Columns

Specimen ID	Axial Load (P0)	Yield force F_y (kN)	Yield Disp. Δ_y (mm)	Peak force F_p (kN)	Peak Disp. Δ_p (mm)	Ultimate force Fu (kN) ($0.85F_p$)	Ultimate Disp Δu (mm)	Ductility factor ($\Delta\mu$)	Ultimate Energy Dissipation (kN-m)
N-0-0.35	$0.35P_0$	98.3	14.4	111.7	77.2	95.0	117.8	8.1	77.52
N-0-0.5	$0.5P_0$	105.2	20.5	119.5	40.8	101.6	81.1	4.0	47.7
N-0-0.6	$0.6P_0$	113.1	14.2	130.1	37.3	109	52.4	3.6	20.8
N-0-0.7	$0.7P_0$	87.9	15.4	99.8	21.9	84.9	38.1	2.5	8.3
N-10-0.35	$0.35P_0$	85.01	14.4	96.6	21.74	82.11	54.2	3.76	25.7
N-10-0.5	$0.5P_0$	65.59	8.56	74.54	14.83	63.35	28.14	3.29	6.83
N-10-0.6	$0.6P_0$	57.15	7.3	64.95	11.12	55.2	17.67	2.42	3.94
N-10-0.7	$0.7P_0$	47.14	7.1	53.57	7.2	45.5	14.11	1.99	3.12
N-15-0.35	$0.35P_0$	64.53	20.14	73.33	29.58	62.33	46.77	2.32	14.95
N-15-0.5	$0.5P_0$	48.47	10.24	55.09	14.89	46.82	23.44	2.29	4.74
N-15-0.6	$0.6P_0$	44.43	7.2	50.49	11.24	42.91	16.13	2.24	3.05
N-15-0.7	$0.7P_0$	35.99	6.41	40.90	6.62	34.7	11.57	1.80	1.42
N-20-0.35	$0.35P_0$	56.33	14.1	64.09	29.03	54.47	42.47	3.01	9.86
N-20-0.5	$0.5P_0$	43.87	10.2	49.86	14.34	42.39	22.1	2.17	2.82
N-20-0.6	$0.6P_0$	35.21	7.41	40.02	11.04	34	15.1	2.04	1.69
N-20-0.7	$0.7P_0$	24.08	7.11	27.37	7.19	23.26	12.15	1.71	0.96

Ductility refers to a structure's ability to withstand deformation without a significant loss in strength or stiffness during its post-elastic behaviour. The ductility factor ($\mu\Delta$) is defined as the ratio of ultimate displacement to yield displacement, while Eu is calculated by summing the cumulative energy dissipated up to the ultimate point. The ductility ratio is a critical parameter commonly used to evaluate the post-peak performance of structures.

Table 4.2 presents a comprehensive summary of the seismic performance characteristics for all sixteen finite element (FE) specimens analyzed in this study, encompassing their ductility parameters and other pertinent properties. In this context, "N" denotes numerical simulation, the range "0 to 20" represents the corrosion percentage, and "0.35P_o to 0.7P_o" indicates the ACR levels. The findings reveal that increasing ACR levels leads to a considerable reduction in both $\mu\Delta$ and E_u.

Fig. 4.13 visually compares the decline in ductility and ultimate dissipated energy for all sixteen samples, illustrating the adverse impact of elevated ACR levels on the seismic performance of the columns. A more in-depth analysis of these results is presented in the following section.

4.3 Discussion

4.3.1 Effect of ACR on 'Pre-Peak Response' of Uncorroded and Corroded Ductile Columns

4.3.1.1. Uncorroded Ductile Columns

The structural behaviour of the sixteen FE ductile models analyzed in this study is summarized in Table 4. **2** 2. Among these, the first four specimens represent uncorroded ductile columns. Specimen "N-0-0.35," which features ductile reinforcement and an ACR of 0.35, was designated as the control specimen. This control specimen exhibited an initial stiffness (K0), corresponding to the first loading cycle, of 10.3 GPa, and a peak flexural strength of 111.7 kN. When the axial compression level was increased by 43%, as in specimen "N-0-0.5" (with identical reinforcement to the control), the flexural strength rose by approximately 7%. Further increases in axial compression, as seen in specimen "N-0-0.6" (72% higher axial load), led to a flexural strength of 130.1 kN, marking a 14.42% increase over the control specimen.

The increase in flexural strength can be attributed to the requirement of higher lateral loads to deform the columns under elevated ACR levels, which enhances resistance to lateral deformation. However, at an ACR of 0.7P_0, a decline in flexural strength was observed. For instance, specimen "N-0-0.7," subjected to a 100% increase in ACR compared to "N-0-0.35," experienced an 11% reduction in flexural strength. The reduction in flexural strength for specimens "N-0-0.6" and "N-0-0.7" can be explained by the effect of secondary stresses resulting from the P-Δ effect. As axial load interacts with lateral drift, it generates a P-Δ moment, which acts in the same direction as the primary moment caused by lateral forces. This interaction results in geometrically induced structural nonlinearity, and at higher axial compression levels, the contribution of the P-Δ moment becomes more pronounced, leading to reduced flexural strength during the pre-peak response period.

It is important to note that the decline in pre-peak response due to higher ACR levels affects not only specimen "N-0-0.7," which experienced a reduction in flexural strength, but also specimens "N-0-0.5" and "N-0-0.6," whose higher flexural strengths tend to mask this effect. From a deformability standpoint, it was observed that the control specimen "N-0-0.35" reached its peak response at a 5.1% drift level. In contrast, specimens "N-0-0.5," "N-0-0.6," and "N-0-0.7" exhibited peak responses at drift levels of 3.2%, 2.7%, and 1.5%, respectively.

When comparing the deformability of specimens "N-0-0.5" (with 43% higher axial load) and "N-0-0.6" (with 72% higher axial load) to the control specimen, it was found that these specimens exhibited gains in flexural strength of 7.07% and 14.42%, respectively, along with a 22.22% increase in deformability (Δp). However, specimen "N-0-0.7," with a 100% higher ACR, showed a significant decrease in deformability, with a 25.57% reduction compared to the control specimen.

4.3.1.2 Corroded Ductile Columns

The post-peak performance of the ductile, corroded columns was evaluated by assessing both the ductility ratio and the cumulative energy dissipation at their ultimate stage. A critical finding of this investigation is the continuous decline in ductility and energy dissipation capacity across all corroded specimens, even though their reinforcement detailing adhered to the latest ductile design codes. For example, specimens with a constant corrosion level of 10%, but subjected to varying ACR of $0.35P_0$, $0.5P_0$, $0.6P_0$, and $0.7P_0$, exhibited ductility reductions of 5.92%, 54.72%, 54.81%, and 60.36%, respectively, when compared to the uncorroded specimen. Notably, a 10% corroded specimen under a 43% higher axial load ($0.5P_0$) showed a significant 54.72% drop in ductility, underscoring the catastrophic effects of simultaneously increasing ACR and corrosion levels.

Furthermore, specimens with a corrosion level of 15% subjected to ACR levels of $0.35P_0$, $0.5P_0$, $0.6P_0$ and $0.7P_0$ experienced ductility reductions of 21.23%, 43.57%, 47.80%, and 57.68%, respectively. Similarly, specimens with 20% corrosion level displayed ductility losses of 28.64%, 45.67%, 54.84%, and 56.40% for the same ACR levels. Previous studies have documented the degradation of reinforcement bar ribs and the reduction of their cross-sectional area due to corrosion. The observed reduction in ductility across all corroded specimens can likely be attributed to a significant weakening of the concrete-rebar bond, which leads to rebar slippage and, consequently, major ductility loss. From the perspective of cumulative energy dissipation, a similar pattern of degradation was noted as ACR and corrosion levels increased.

To further explore this, the cumulative energy dissipation was calculated for specimens with varying corrosion levels but constant ACR. For instance, at an ACR of $0.35P_0$, specimens with corrosion levels of 10%, 15%, and 20% exhibited energy dissipation reductions of 66.84%, 80.71%, and 87.28%, respectively. When the ACR was increased by 43% ($0.5P_0$), the reduction in dissipated energy was even more severe, with declines of 85.68%, 90.06%, and 94.08% for the same corrosion levels. Further increases in axial compression by 72% ($0.6P_0$) resulted in similar trends, with dissipated energy reductions of 81.05%, 85.33%, and 91.81% for the 10%, 15%, and 20% corroded specimens, respectively. Finally, when the axial compression was increased to 100% ($0.7P_0$), the reduction in energy dissipation followed the same pattern, with decreases of 64.40%, 82.89%, and 88.43%, respectively, compared to the uncorroded specimens.

4.3.1.3 Previous Research Comparison

Numerous researchers have undertaken experimental investigations into the seismic performance of RC columns, focusing on key variables such as corrosion levels, cross-sectional dimensions, ACR, concrete strength, transverse reinforcement ratios, and stirrup spacing. To summarize the breadth of these studies, Table 4. 3 consolidates their findings, emphasizing the impact of ACR levels on structural seismic behaviour. Notably, the majority of the dataset consists of results derived from small-scale columns with cross-sectional diameters of less than 450 mm, indicating that the size effect plays a critical role in influencing the ductility and energy dissipation capacity of RC columns (Z. Li et al., 2019).

For large-scale RC columns subjected to high axial loads, additional test data, as detailed in (Anh Huy et al., 2022) were used to explore their seismic behaviour. A comparative analysis suggests that while increased ACR levels may induce marginal changes in the flexural strength of columns, these changes tend to be minimal, with only slight increases or decreases observed. More importantly, a notable reduction in the deformability of the columns was observed. This diminished capacity to deform leads to premature failures, both before and after peak load, which severely undermines the columns' ability to withstand seismic forces effectively (Ma et al., 2012; Mo & Wang, 2000; Rajput & Sharma, 2018).

Increased axial compression significantly affects the post-peak behaviour of the specimens, manifesting as sharp reductions in ductility, ultimate drift ratios, and final curvature values (Z. Li & Gan, 2022). Additionally, both corroded and uncorroded columns exhibit a pronounced decrease in post-peak ductility and ultimate curvature as axial compression rises (Dai et al., 2020, 2021; Yang et al., 2016). Researchers have also leveraged advanced non-linear FE simulations to analyze further the decline in seismic resistance caused by corrosion damage, offering critical insights into the seismic vulnerability of RC columns (El-Joukhadar et al., 2023).

Following an extensive investigation into the impact of ACR on corroded ductile columns, the research was subsequently extended to analyze the effect of ACR on corroded non-ductile columns. The detailed observations and results of this analysis are presented in the subsequent section.

Table 4. 3 Comparison of Previous Studies on RC Uncorroded and Corroded Columns

Author	ID	Size (mm)	Specimen height (mm)	Plastic Hinge (mm)	*f'c* (MPa)	Øh (mm)	*S* (mm)	*σus* (Mpa)	$Ø_L$ (mm)_No.s	σul (Mpa)	Axial Load (P_0)	Axial Load (kN)	Yield Force *Fy* (kN)	Yield Disp *Δy* (mm)	Peak Force Fp (kN)	Peak disp *Δy* (mm)	Ultimate Load Fu (kN)	Ultimate Disp Δu (mm)	Ultiamte Energy En (kN-m)	Ductility factor (*Δu*)	**ρsh%**
	N-10-0.35	300 x 300	1800	800	30	10	75	500	16_8	550	0.35	941	85.01	14.4	96.6	21.74	82.11	54.2	25.7	3.76	1.31
	N-10-0.5	300 x 300	1800	800	30	10	75	500	16_8	550	0.5	1344	65.59	8.56	74.54	14.83	63.35	28.14	6.83	3.29	1.31
	N-10-0.6	300 x 300	1800	800	30	10	75	500	16_8	550	0.6	1613	57.15	7.3	64.95	11.12	55.2	17.67	3.94	2.42	1.31
	N-10-0.7	300 x 300	1800	800	30	10	75	500	16_8	550	0.7	1889	47.14	7.1	53.57	7.2	45.5	14.11	3.12	1.99	1.31
Present Study	N-15-0.35	300 x 300	1800	800	30	10	75	500	16_8	550	0.35	941	64.53	20.14	73.33	29.58	62.33	46.77	14.95	2.32	1.31
	N-15-0.5	300 x 300	1800	800	30	10	75	500	16_8	550	0.5	1344	48.47	10.24	55.09	14.89	46.82	23.44	4.74	2.29	1.31
	N-15-0.6	300 x 300	1800	800	30	10	75	500	16_8	550	0.6	1613	44.43	7.2	50.49	11.24	42.91	16.13	3.05	2.24	1.31
	N-15-0.7	300 x 300	1800	800	30	10	75	500	16_8	550	0.7	1889	35.99	6.41	40.90	6.62	34.7	11.57	1.42	1.80	1.31
	N-20-0.35	300 x 300	1800	800	30	10	75	500	16_8	550	0.35	941	56.33	14.1	64.09	29.03	54.47	42.47	9.86	3.01	1.31
	N-20-0.5	300 x 300	1800	800	30	10	75	500	16_8	550	0.5	1344	43.87	10.2	49.86	14.34	42.39	22.1	2.82	2.17	1.31
	N-20-0.6	300 x 300	1800	800	30	10	75	500	16_8	550	0.6	1613	35.21	7.41	40.02	11.04	34	15.1	1.69	2.04	1.31
	N-20-0.7	300 x 300	1800	800	30	10	75	500	16_8	550	0.7	1889	24.08	7.11	27.37	7.19	23.26	12.15	0.96	1.71	1.31
Lacobucci, R. D.	AS-1NS	305 x 305	1473	610	31.4	10	300	680	20_8	640	0.33	965	95.2		108.2		91.9		66.2	3.7	0.61
et al.	AS-7NS	305 x 305	1473	610	37	10	300	680	20_8	640	0.33	965	103.1		117.2		99.6		7.7	5.4	0.61
	AS-8NS	305 x 305	1473	610	42.3	10	300	680	20_8	640	0.56	1638	93		105.7		89.8		7.9	5.4	0.61
K. Y. Dai, et al.	UC-0.1	300 x 300	1000	250	33.2	8	80	646	18_8	569	0.1	275	113.18	10.95	137.28	33.08	116.85	44.64	114.12	4.08	0.61
	UC-0.45	300 x 300	1000	250	33.2	8	80	646	18_8	569	0.45	1238	172.71	6.13	203.6	12.19	173.09	23.21	61.65	3.79	0.61
J. Cheng et al.	L-1	400 x 200	1800	800	36.2	8	100	556	16_4	456			31.5	10.3	35.3	30	29.8	64.2	13.10	6.19	0.503
	WF-3	300 x 300	1242	550	49.6	6	43	441	12_12	625	0.4		195	5.82	226	10.5	193.6	25	156.4	4.29	0.55
Z. Li et al.	WF-5	500 x 500	1820	800	49.6	10	71	346	20_12	595	0.4		510	9.15	577	12.4	508.5	32.2	724.1	3.51	0.55
	WF-7	700 x 700	2548	1120	49.6	14	100	351	28_12	636	0.4		907	10.9	1038	13.2	904.2	39.6	1987.2	3.6	0.55
	C-F-L	800 x 800	3200	800	43	12.6	150	470	32_24	473	0.09	2560	1518.75	26.9	2025	96	1721.25	112.3	50 x 10^2	4.2	0.42
	C-S-L	800 x 800	3200	800	43	6.4	350	398	32_24	473	0.09	2560	1092.75	17.3	1457	17.6	1238.45	24.3	8.2 x 10^3	1.4	0.02
P. P. Anh	C-F-H	800 x 800	3200	800	44	15.7	120	467	32_24	473	0.53	14822	1939.5	24	2586	30.8	2198.1	67.2	36.8 x 10^3	2.8	0.82
Huy. et al	C-FS-H	800 x 800	3200	800	43	9.5	120	473	32_24	473	0.54	14822	1879.5	19	2506	19.7	2130.1	33	20 x 10^3	1.7	0.3
	CO-15	D= 260	1000	300	32.4	8	100	510	16_6	573	0.15	277	61.41	4.42	63.16	33.17	62.63	37.4	74.64	8.46	0.61
Ma, Y. et al.	CO-25	D= 260	1000	300	32.4	8	100	510	16_7	573	0.25	461	71.23	5.16	75.88	30.67	68.57	38.09	72.83	7.38	0.61
	C0-40	D= 260	1000	300	32.4	8	100	510	16_8	573	0.4	737	80.23	4.13	85.23	10.23	75.84	24.08	53.54	5.82	0.61
Dai, K. Y. et al.	UC-0.1	300 x 300	1650	300	30	8	80	569	16_8	646	0.1	285	113.18	10.95	137.28	33.08	116.85	44.64	113.06	4.08	0.61
	UC-0.45	300 x 300	1650	300	30	8	80	569	16_9	646	0.45	1279	172.71	6.13	203.6	12.19	173.09	23.21	63.31	3.79	0.61
S. Y. Yang, et al.	ZZ-1	210 x 210	1100	300	46.4	6	90	727	18_4	573	0.15	470	50.7	8.2	59.4	28.4	52.3	44.6	32	7.3	0.49

Note: f'_c= compressive strength of concrete cylinder, $Ø_h$= diameter of transverse reinforcement, *s*= spacing of transverse reinforcement c/c, σ_{us}= Ultimate Stirrups strength, $Ø_L$= Longitudinal Reinforcement diameter, σ_{ul}= Longitudinal Bars strength, E_n= Cumulative Energy Dissipation, ρ_{sh}= transverse reinforcement ratio.

4.4 Results of Non- ductile Corroded Columns

A detailed parametric study was conducted to assess the combined effects of varying corrosion levels and ACRs on the seismic performance of Non-ductile corroded columns. The specimens were modeled with consistent material properties, reinforcement configurations, interaction mechanisms, lateral displacement protocols, and boundary conditions. The seismic response of all twelve numerical models was thoroughly analyzed and compared using several key parameters, including backbone curve analysis, stiffness degradation, energy dissipation, ductility factors, and overall deformability.

4.4.1 Backbone Curves Comparison

The backbone responses of all Eight Non-ductile corroded models for 0%, 15%, and 30% corrosion percentages at ACR levels from $0.35P_0$ to $0.7P_0$ are illustrated in Fig. 4. 14 (a-c), respectively. A consistent and linear connection between load and displacement was observed within the elastic response range. Nevertheless, when the seismic drift and ACR levels were increased, the load-deflection trajectory underwent drastic changes. The failure point in the post-peak range was taken as 85% of the peak load. However, the test was extended to examine its impact at elevated drift levels further.

It was observed that all corroded models showed a consistent reduction in their flexural capacity irrespective of their level of corrosion. The data derived from these envelope curves depict a comparative response of all the corroded columns and provide detailed information on how the rise in ACR directly affects the maximum strength, ductility, and post-peak response of all Non-ductile corroded columns.

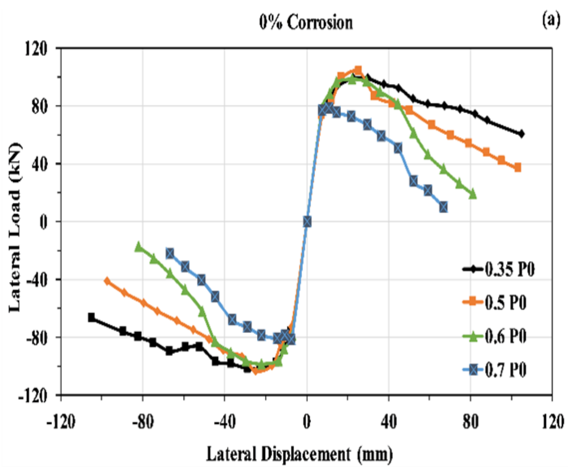

0% Corrosion

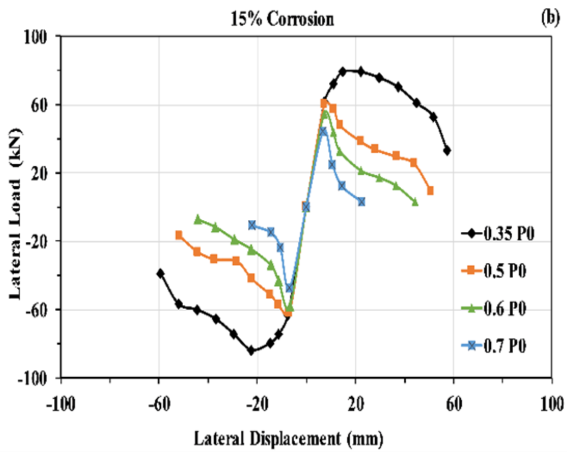

15% Corrosion

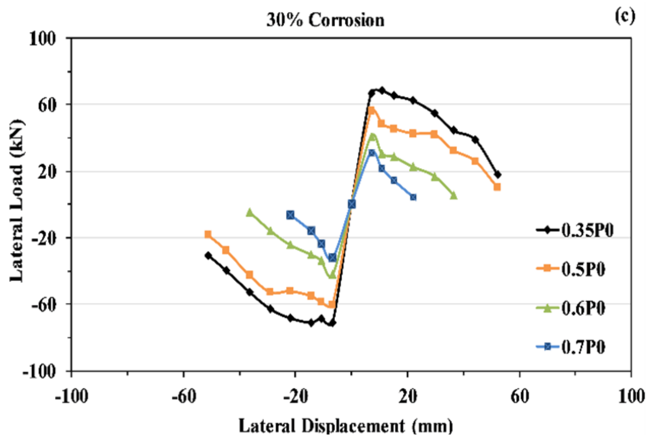

30% Corrosion

Fig. 4. 14 Backbone Curves of Non-ductile Corroded Columns at Various Corrosion Levels

4.4.2 Stiffness Deterioration

Secant stiffness (K_n) is a critical parameter in assessing the rate and extent of structural degradation, particularly under seismic loading. The deterioration of stiffness is influenced by multiple factors, including the reduction in the cross-sectional area of corroded steel, the deformation of longitudinal rebars due to compressive forces, and the weakening of the bond between the steel reinforcement and the surrounding concrete. These factors collectively diminish the structural stiffness over time.

Fig. 4. 15(a-c) illustrates the relationship between stiffness degradation and lateral displacement for non-ductile corroded columns subjected to different levels of corrosion. Notably, the data reveal an inverse relationship between stiffness and both ACR and corrosion levels, indicating that as ACR and corrosion increase, stiffness declines more sharply. In a comparative analysis, a 47.6% reduction in stiffness was observed in specimens with 30% corrosion at an ACR of $0.7P_0$, relative to the control specimens. This significant reduction highlights the compounded impact of corrosion and axial loading on structural stiffness, emphasizing the need for targeted retrofitting and rehabilitation strategies for such deteriorated columns.

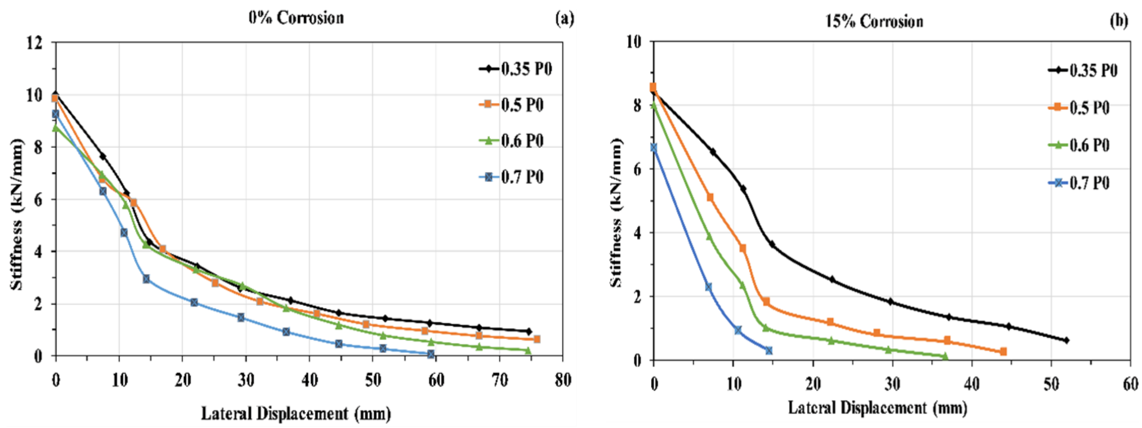

0% Corrosion

15% Corrosion

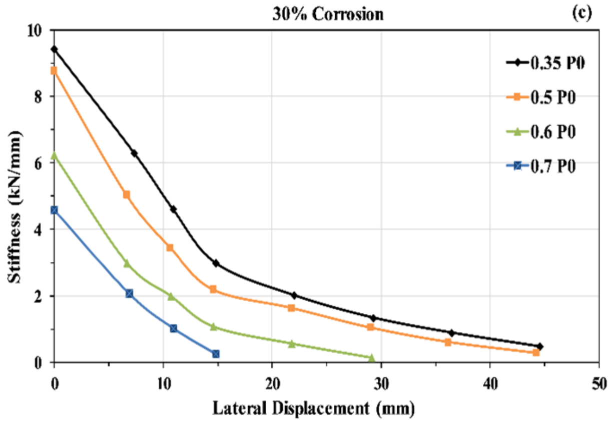

30% Corrosion

Fig. 4. 15 Stiffness Degradation of Non-ductile Corroded Columns at Various Corrosion Levels

4.4.3 Energy Dissipation Capacity

The energy dissipated during each loading cycle was quantified by calculating the net area under the envelope curve at each drift level using a MATLAB program. To determine the total energy accumulated up to any given drift level, the energy dissipated in the current cycle was added to the sum of all preceding cycles. Fig. 4. 16 illustrates the cumulative energy dissipation as a function of lateral drift for all non-ductile corroded column specimens.

The results clearly indicate that columns with higher ACR exhibit significantly reduced energy dissipation capacity. Notably, columns with an ACR of $0.7P_0$ dissipated less than half the energy compared to those with an ACR of $0.35P_0$, underscoring the negative impact of higher axial loads on seismic performance. Furthermore, as corrosion levels increased, a substantial reduction in total energy dissipation was observed, highlighting the detrimental effect of corrosion on the post-peak response of the structures. Even at similar or varying ACR levels, energy dissipation declined sharply with increasing corrosion, emphasizing the compounded effect of corrosion and axial load on the seismic resilience of Non-ductile columns.

This trend suggests that as the integrity of the steel-concrete bond deteriorates due to corrosion, the ability of these columns to dissipate seismic energy diminishes, making them more vulnerable to failure under seismic loading. These findings highlight the critical importance of addressing corrosion in Non-ductile columns to maintain their seismic performance and energy dissipation capacity.

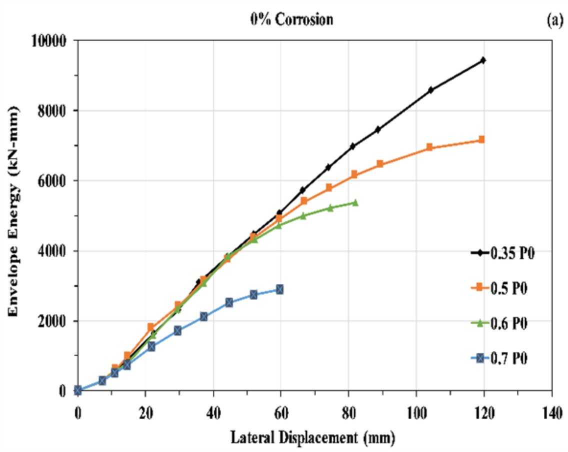

0% Corrosion

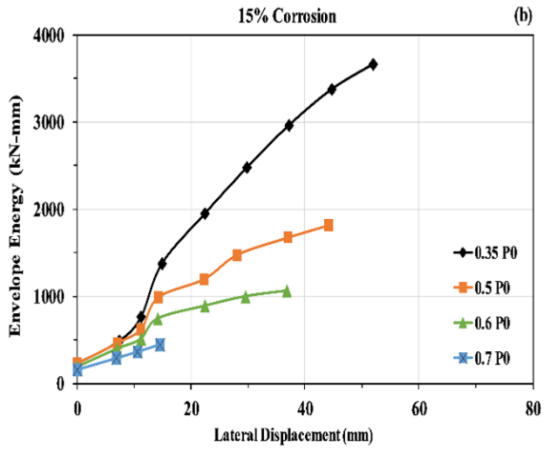

15% Corrosion

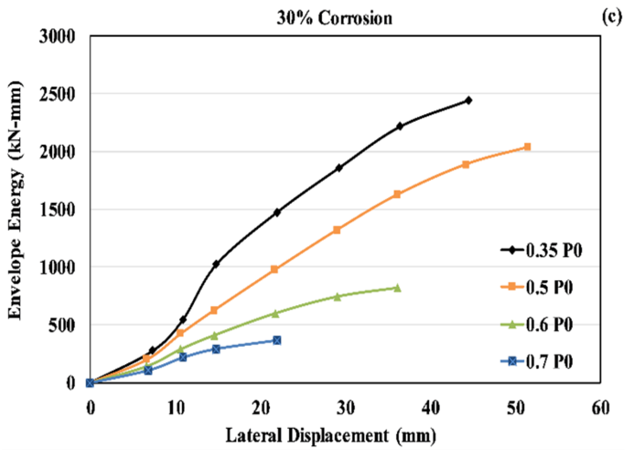

30% Corrosion

Fig. 4. 16 Cumulative Energy v/s Lateral Displacement Comparison

4.4.4 Deformability and Displacement Ductility

The current investigation comprehensively analyzed the deformability characteristics of the tested specimens by evaluating key performance indicators such as yield, peak, and ultimate displacement points. These parameters were then systematically compared in relation to varying ACR, as referenced in (Cheng et al., 2020). The results revealed a substantial influence of increasing ACR levels on the deformability metrics, manifesting in both the pre-peak and post-peak response phases across all corroded and control specimens.

Fig. 4. 17 illustrates a detailed comparison of how the twelve modeled specimens, both control and corroded at varying ACR levels, affected critical yield, peak, and ultimate displacement values. Notably, the study found that rising ACR levels had a pronounced impact on deformability parameters, particularly affecting ultimate displacement, peak displacement, and yield displacement in both corroded and uncorroded specimens.

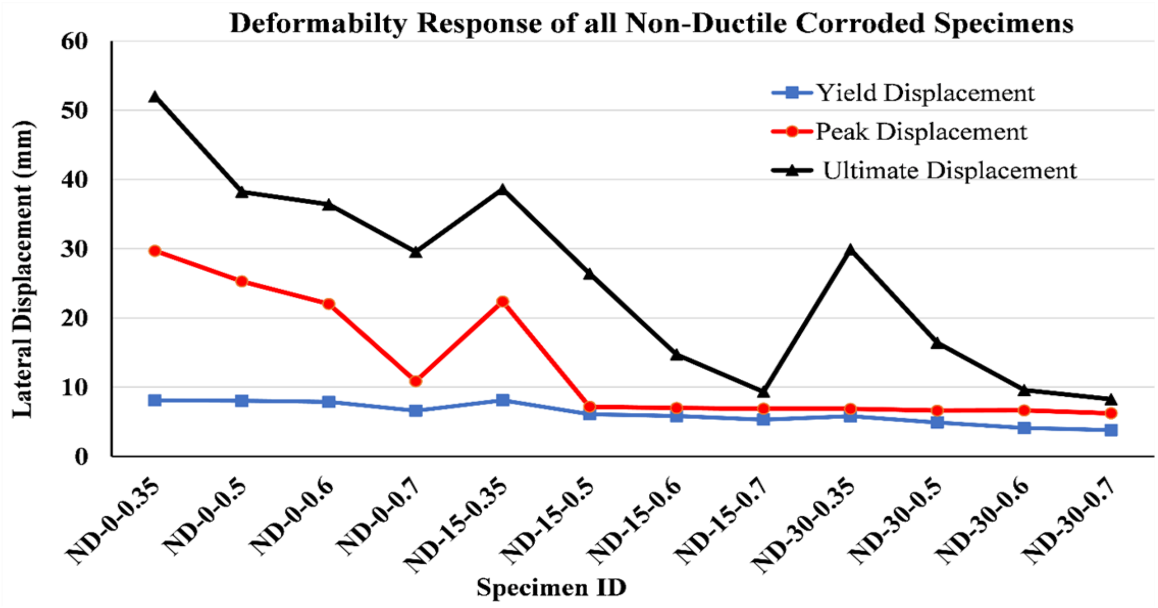

Fig. 4. 17 Deformability Response of Non- ductile Corroded Specimens

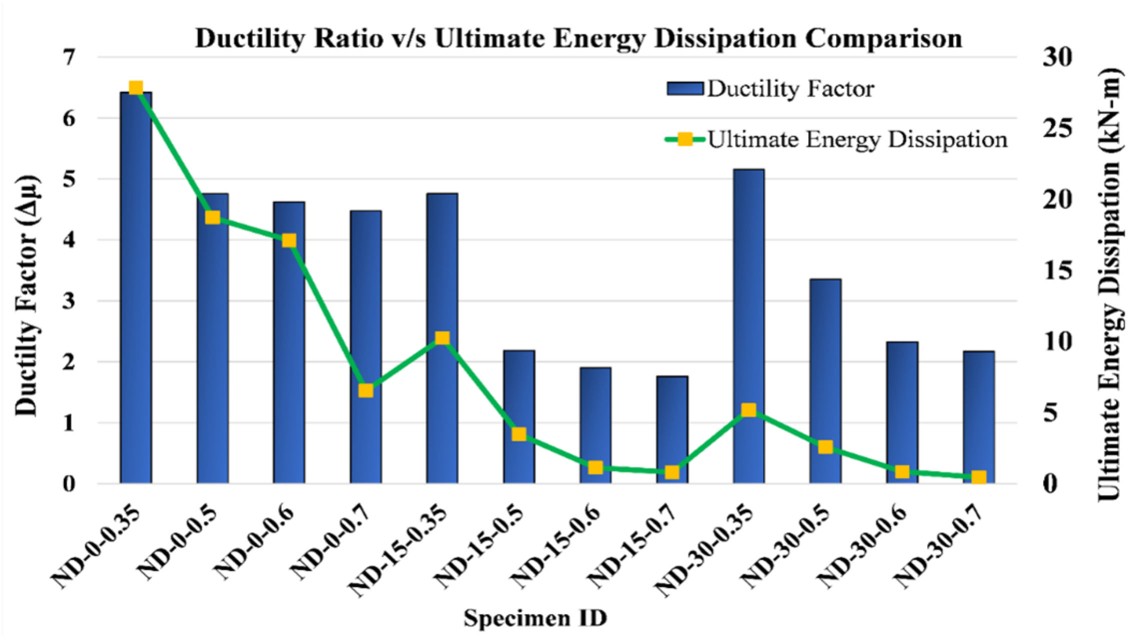

Fig. 4. 18 Ductility ratio v/s Ultimate Energy Dissipation Comparison

Additionally, Fig. 4. 18 offers an in-depth explanation of the ductility factor and cumulative energy dissipation for all modeled specimens. As expected, a consistent decline in both ductility and energy dissipation was observed with increasing ACR levels, highlighting the detrimental effects of corrosion. The findings underscore the correlation between increased ACR and reduced structural resilience.

Table 4. 4 presents the seismic performance characteristics of the twelve FE models, further supporting the conclusions drawn. In this context, "ND" denotes non-ductile simulation, the range "0 to 30" represents the corrosion percentage, and "$0.35P_0$ to $0.7P_0$" indicates the ACR levels. A thorough analysis

of these findings and their implications is discussed in the following section, providing greater insight into the complex relationship between corrosion-induced degradation and structural performance.

Table 4. 4 Summary of Seismic Performance of all Modeled Non- ductile Corroded Columns

Specimen ID	Axial Load (P0)	Axial load (kN)	Yield force F_y (kN)	Yield Disp. Δ_y (mm)	Peak force F_p (kN)	Peak Disp. Δ_p (mm)	Ultimate force Fu (kN) ($0.85F_p$)	Ultimate Disp. Δu (mm)	Ductility factor (Δμ)	Ultimate Energy Dissipation (kN-m)
ND-0-0.35	$0.35P_0$	941	80.1	8.1	98.97	29.7	85.85	52	6.41	27.84
ND-0-0.5	$0.5P_0$	1344	82.7	8.03	103.43	25.3	87.9	38.2	4.75	18.71
ND-0-0.6	$0.6\ P_0$	1613	79.2	7.87	98.8	22.1	83.98	36.4	4.62	17.11
ND-0-0.7	$0.7\ P_0$	1889	62.6	6.6	78.33	10.9	66.51	29.54	4.47	6.543
ND-15-0.35	$0.35P_0$	941	65.2	8.11	81.33	22.4	69.13	38.6	4.75	10.24
ND-15-0.5	$0.5\ P_0$	1344	48.9	6.1	61.17	7.17	51.99	13.32	2.18	2.278
ND-15-0.6	$0.6\ P_0$	1613	44.7	5.84	55.98	6.99	47.58	11.12	1.90	1.12
ND-15-0.7	$0.7\ P_0$	1889	36.7	5.31	45.88	6.88	38.99	9.34	1.75	0.81
ND-30-0.35	$0.35P_0$	941	55.2	5.8	69.01	6.87	58.65	29.91	5.15	5.18
ND-30-0.5	$0.5\ P_0$	1344	46.4	4.9	58.12	6.62	49.4	16.42	3.35	2.57
ND-30-0.6	$0.6\ P_0$	1613	33.2	4.11	41.5	6.65	35.27	9.57	2.32	0.85
ND-30-0.7	$0.7\ P_0$	1889	25.2	3.8	31.51	6.23	26.78	8.25	2.17	0.445

4.5 Discussion

4.5.1 Effect of ACR on Pre-Peak Response of Non- ductile Corroded Columns

The non-ductile corroded columns demonstrated significant vulnerability to the combined effects of increased axial compression and varying degrees of corrosion. A comparative analysis of the control specimens across different ACR levels revealed that the control specimen labeled "ND-0-0.5" (with an ACR of $0.5P_0$) exhibited a 3.12% higher flexural strength compared to the specimen at a lower ACR level of $0.35P_0$. This modest increase in strength may be attributed to the enhanced confined compression strength of the concrete.

However, as the ACR levels increased to $0.7P_0$, a steady reduction in strength was observed, which was likely due to the reduced confinement in the columns as a result of the sparse distribution of stirrups. In specimens subjected to 15% corrosion, the peak strength reductions were substantial, with declines of 20%, 40.3%, 45.45%, and 55.2% observed at ACR levels of $0.35P_0$, $0.5P_0$, $0.6P_0$, and $0.7P_0$, respectively, compared to the control specimens. Similarly, specimens exposed to 30% corrosion experienced even more severe strength reductions, with declines of 32.07%, 43.4%, 59.5%, and 69.3%

at the same ACR levels. These significant reductions highlight the critical impact of corrosion and axial compression on the structural integrity of the columns.

From a deformability perspective, the pre-peak response of the specimens also exhibited notable changes. For the specimen N-15–0.35, the peak response was reached at a drift level of 2.25%. In contrast, the peak responses for specimens N-15–0.5, N-15–0.6, and N-15–0.7 occurred at progressively lower drift levels of 0.81%, 0.72%, and 0.45%, respectively. A similar trend was observed in the 30% corroded specimens, with peak responses at 0.85%, 0.55%, 0.5%, and 0.41% drift levels for specimens N-30-0.35, N-30-0.5, N-30-0.6, and N-30-0.7, respectively. This marked reduction in drift levels can be attributed to the increasing influence of secondary stresses resulting from the P-Δ effect, which becomes more pronounced under higher axial compression.

The P-Δ effect, caused by the interaction between axial compression and lateral drift, generates a moment in the same direction as the primary moment induced by lateral forces. At elevated levels of axial compression, the contribution of the P-Δ moment becomes significant, leading to pronounced degradation in the pre-peak region. This degradation ultimately culminates in column buckling due to concrete crushing, which results in a rapid loss of structural strength.

These findings underscore the detrimental impact of increasing ACR and corrosion on the deformability of the specimens. As ACR levels rise, the specimens reach their pre-peak responses earlier, compromising both the safety and stability of the structure. The study highlights the critical need for considering the combined effects of corrosion and axial compression when evaluating the structural performance and safety of Non-ductile columns.

4.5.2 Effect of ACR on Post-Peak Response Domain of Non-ductile Corroded Columns

In the post-peak response phase of column behaviour, a critical stage known as the "Ultimate" stage is identified, where a specimen is considered to have failed when the load reduces to 85% of its peak flexural strength. Using this criterion, the study evaluated ductility parameters, such as the ductility ratio and cumulative envelope energy. It was observed that the overall deformability of columns decreased progressively with increasing ACR levels. Similar trends were found in the behaviour Non-ductile columns as they transitioned into the post-peak region, where their already low ductility characteristics were further compromised by increasing ACR levels.

As depicted in Fig 4. 14(b), specimens with 15% corrosion, subjected to ACR levels of $0.35P_0$, $0.5P_0$, $0.6P_0$, and $0.7P_0$, showed a significant reduction in ductility by 25.8%, 44.01%, 58.8%, and 60.6%, respectively, compared to control specimens. Furthermore, energy dissipation was considerably reduced by 63.1%, 87.8%, 90.4%, and 91.3%, as detailed in Fig. 4. 15(b). The structural performance further deteriorated at a higher corrosion level of 30%, as demonstrated by ductility reductions of

20.15%, 29.45%, 49.45%, and 51.1%, as shown in Fig. 4. 14(c). Concurrently, energy dissipation saw reductions of 81.3%, 86.2%, 94.1%, and 95.2% at the same ACR levels, as outlined in Fig. 4. 15(c). These results clearly indicate that Non-ductile columns subjected to elevated ACR levels experience catastrophic failure during the post-peak phase due to a significant loss in structural strength, ductility, and energy dissipation capabilities.

A noteworthy observation emerged when comparing the ductility characteristics of non-ductile corroded columns exposed to different levels of corrosion, specifically at 15% and 30%. Surprisingly, these columns subjected to 30% corrosion levels exhibited superior ductility compared to those exposed to 15% corrosion, particularly under higher axial loads, as presented in Table 4. 4. This counterintuitive result can be attributed to the pronounced reduction in yield displacement as corrosion levels increased.

As corrosion advances, the material properties of the columns degrade, leading to an earlier onset of yielding. Consequently, the ductility factor, defined as the ratio of ultimate displacement to yield displacement, increased for non-ductile corroded specimens with 30% corrosion. This phenomenon is largely driven by the significant reduction in yield displacement, which lowers the denominator in the ductility factor calculation. Therefore, despite the greater extent of damage observed in columns with higher corrosion levels, these specimens appear to exhibit enhanced ductility characteristics due to the relative decrease in yield displacement.

In summary, the findings highlight the complex interplay between corrosion, axial compression, and structural deformability. As ACR levels and corrosion increase, structural degradation becomes evident in both strength and energy dissipation, ultimately leading to premature failure. However, the unexpected improvement in ductility at higher corrosion levels underscores the nuanced effects of corrosion on the mechanical behaviour of non-ductile corroded columns, warranting further investigation into the implications for structural safety and resilience in real-world applications.

4.6 Conclusions

A comprehensive analysis was conducted to assess the effects of varying ACR levels on the seismic performance of corroded RC columns designed in accordance with ductile design standards. The study yielded several important conclusions:

1. Both ductile and non-ductile columns, whether corroded or uncorroded, exhibited significant structural degradation as ACR levels increased. This included reductions in strength, stiffness, deformability, and ductility, with ductility indices, particularly energy dissipation, experiencing a reduction five to seven times greater than the corresponding reduction in strength, highlighting the vulnerability of these columns under elevated ACR conditions.

2. Increased ACR levels caused a pronounced deterioration in pre-peak and post-peak response characteristics in both ductile and non-ductile columns, leading to earlier peak load attainment and higher susceptibility to post-elastic failures at lower drift levels.
3. In ductile columns, increasing ACR from $0.35P_0$ to $0.6P_0$ led to a 14.4% increase in peak strength in uncorroded specimens, while corroded specimens experienced a notable decline in strength under the same conditions. Similarly, in non-ductile columns, a modest 3.12% peak strength gain was observed at lower ACR levels, which reversed at higher ACRs, indicating that corrosion amplifies the adverse effects of ACR in both column types.
4. Energy dissipation behaviour, represented by the equivalent viscous damping ratio (ξ_{eq}), consistently increased in ductile corroded columns as ACR and corrosion levels rose. Conversely, in non-ductile columns, energy dissipation proved to be a more reliable indicator of structural performance post-peak than ductility factors.
5. Corroded ductile columns demonstrated a continuous decline in energy dissipation capacity and ductility ratio in the post-peak phase as ACR and corrosion levels increased. Similarly, non-ductile columns experienced reductions in ductility and energy dissipation that significantly reduced the strength, further emphasizing the structural vulnerabilities of both column types under these conditions.
6. The combination of high ACR levels and corrosion exacerbates premature structural failures in both ductile and non-ductile columns, particularly in the plastic hinge regions, where energy dissipation and post-peak performance are severely compromised.
7. The observed degradation patterns suggest that external strengthening techniques, such as retrofitting corroded columns in critical regions, are essential for maintaining seismic resilience and ensuring the safety of aging infrastructure subjected to elevated ACR conditions.

These findings collectively provide significant insights into the seismic performance of corroded reinforced concrete columns, emphasizing the necessity of tailored design and retrofitting approaches to address the compounded effects of axial compression and corrosion in both ductile and non-ductile structural elements.

Chapter 5

Discussions and Conclusions

5.1 Introduction

The study investigated the combined effect of corrosion and axial compression on the seismic performance of ductile and non-ductile columns. If focused on comprehensively evaluating the structural response that is subjected to corrosion-induced damages such as mechanical abrasion, uneven settlements, chloride intrusion, carbonation, and sulfate attacks, which accelerate structural weakening. Numerical models were developed to validate the experimental results for both control and corroded columns. After completing the validation process, an extensive parametric investigation was initiated using 3D numerical models to analyse the combined effect of varying ACR and corrosion on the structural performance of RC column with and without ductile detailing.

A significant contribution of this work was its focus on the hinge regions of columns, essential for ductile performance during seismic events. The investigation of hysteresis curves, backbone responses, and energy dissipation demonstrated that ductility, a key indicator of seismic resilience, decreased as ACR and corrosion levels increased. These findings underscore the need to consider ACR and corrosion in structural assessments and seismic design strategies. This research calls for integrating ACR considerations into current seismic design codes to enhance the predictability of RC column performance and inform maintenance and retrofitting practices. By quantifying the impacts of corrosion and ACR, this study provides engineers with essential data to develop strategies that prolong service life and ensure structural safety in seismically active and corrosive environments.

The insights gained support the need for updated design standards that account for these factors, enabling the development of more resilient infrastructure. Ultimately, this work offers a foundation for safer, more sustainable engineering practices prioritizing immediate structural integrity and long-term durability.

5.2 Research Conclusions

The analysis of ductile and non-ductile columns subjected to varying ACR and corrosion levels reveals important insights into their seismic behaviour and performance. The following discussion synthesizes the findings of this study, comparing the impact of different parameters on column strength, deformability, energy dissipation, and failure mechanisms.

1. The study demonstrated that increasing the ACR from $0.35P_o$ to $0.5P_o$ resulted in a slight improvement in flexural strength by 7%. Further increases in ACR to $0.6P_o$ and

$0.7P_o$ led to larger gains in flexural strength, with an increase of 14.12% at $0.6P_o$. However, at a 100% increase in ACR ($0.7P_o$), the flexural strength decreased by 11%, indicating the detrimental effect of excessive axial compression on strength.

2. The deformability of the columns was negatively affected by increasing ACR. For the ductile specimens, specimen D0.5 exhibited a 47% reduction in deformability with a 43% increase in ACR, while specimen D0.7 showed a 71.6% reduction in deformability. In contrast, non-ductile specimens exhibited even more severe reductions, with specimens ND0.6 and ND0.7 showing deformability losses of 82% and 89%, respectively.
3. As ACR increased, the drift at peak response for ductile specimens decreased drastically. The control specimen, D0.35, reached its peak response at 5.1% drift, whereas increasing ACR to $0.5P_o$, $0.6P_o$, and $0.7P_o$ resulted in peak drifts of 2.7%, 2%, and 1.5%, respectively. This suggests that higher axial compression reduces the flexibility of the column, leading to earlier failure at lower drift levels.
4. The pre-peak behaviour of the specimens was compromised as ACR increased, with brittle failure mechanisms such as buckling and crushing becoming more prominent. Post-peak behaviour also showed significant degradation, with ultimate displacement reductions of 31.2%, 60%, and 67.6% for D0.5, D0.6, and D0.7, respectively. This highlights the vulnerability of columns under excessive axial loads.
5. Energy dissipation capacity, a key factor in seismic performance, was severely reduced with higher ACR. Ductile specimens showed a decline in energy dissipation by 38.5%, 73%, and 90% at ACRs of $0.5P_o$, $0.6P_o$, and $0.7P_o$, respectively, compared to the control specimen. This indicates that higher axial loads significantly impair the column's ability to dissipate seismic energy.
6. Non-ductile columns showed a consistent decline in both flexural strength and deformability as ACR increased. For example, ND0.5 exhibited a 22% reduction in flexural strength and a 38% drop in deformability compared to D0.5. At higher ACR levels, non-ductile columns experienced even more severe reductions, with ND0.6 and ND0.7 showing cumulative energy dissipation reductions of 76% and 94.2%, respectively.
7. A comparison between ductile and non-ductile columns revealed that non-ductile columns outperformed ductile columns at higher ACRs in terms of ductility. For instance, ductile column D0.7 had 39% lower ultimate displacement and 61% less energy dissipation compared to non-ductile ND0.35, illustrating the performance trade-offs between ductile and non-ductile designs under high axial loads.

8. The failure mechanisms observed in both ductile and non-ductile columns under increased ACR levels were primarily due to the P-Δ effect. This effect, induced by axial compression, generated secondary stresses that led to concrete crushing, buckling, and a rapid loss of strength, particularly in columns with higher ACRs.
9. Energy dissipation was identified as a more reliable metric for post-peak performance compared to ductility factors, which can sometimes yield misleading values under severe damage. The cumulative energy dissipation reductions were especially pronounced in corroded columns, emphasizing the need for energy-based evaluation criteria in seismic design.
10. In the case of corroded ductile columns, the results were even more pronounced. For instance, in the case of 10% corrosion, ductility reductions were observed to be 5.92%, 54.72%, 54.81%, and 60.36% at ACRs of $0.35P_o$, $0.5P_o$, $0.6P_o$, and $0.7P_o$, respectively. This indicates that corrosion exacerbates the negative effects of increasing ACR, with significant losses in ductility and strength as corrosion levels rise.
11. The increase in axial compression further compounded the impact of corrosion on the performance of the columns. For columns with 15% corrosion, ductility reductions reached 21.23%, 43.57%, 47.80%, and 57.68% across the same ACR spectrum. For 20% corrosion, the reductions were even more severe, at 28.64%, 45.67%, 54.84%, and 56.40%, emphasizing the cumulative impact of corrosion and axial compression on the overall structural performance.
12. Cumulative energy dissipation in corroded specimens decreased significantly with higher corrosion levels. At ACRs of $0.35P_o$, energy dissipation reductions were 66.84%, 80.71%, and 87.28% for corrosion levels of 10%, 15%, and 20%, respectively. At a 43% increase in ACR, these reductions became more severe, reaching 85.68%, 90.06%, and 94.08%, respectively, demonstrating the critical loss of energy dissipation under combined ACR and corrosion effects.
13. The P-Δ effect played a crucial role in reducing flexural strength, particularly in corroded specimens. The secondary stresses induced by axial compression at high ACR levels contributed to rapid strength loss and led to concrete crushing, highlighting the vulnerability of corroded columns under high compression.
14. Finally, the interplay between corrosion and axial compression revealed a complex relationship in the behaviour of RC columns. While higher corrosion levels generally degrade structural properties, their influence on certain parameters, such as ductility, can lead to unexpected improvements under specific conditions. This suggests that further research is needed to better understand the real-world implications of these combined effects and to develop targeted retrofitting strategies for improving the seismic performance of corroded RC columns.

In summary, the results emphasize the importance of considering both axial compression and corrosion when designing reinforced concrete structures for seismic resilience. While moderate ACR levels can enhance strength, excessive axial loads and corrosion significantly degrade the performance of columns, particularly in terms of ductility and energy dissipation. These findings highlight the need for revised design guidelines that address the compounded effects of ACR and corrosion on seismic behaviour. Both ductile and non-ductile columns showed significant reductions in structural properties strength, deformability, stiffness, and ductility when subjected to elevated ACR levels.

5.3 Recommendations for Future Work

1. **Future studies Application of 3D FE Modelling for Retrofitted Columns**: Future research should extend the 3D FE models developed in this study to further investigate the seismic response of retrofitted corroded RC columns. This will provide valuable insights into the efficacy of various retrofitting strategies, contributing to the restoration or enhancement of seismic resilience of deteriorated structures.
2. **Investigation of Biaxial Loading Effects:** It is crucial to expand the analysis of lateral load responses by considering biaxial loading conditions. This would yield more realistic seismic simulations, allowing for a deeper understanding of how RC columns behave under complex dynamic forces in real-world scenarios.
3. **Incorporation of Environmental Corrosion Variables:** A more realistic representation of corrosion's effects can be achieved by incorporating environmental factors such as temperature, humidity, and oxygen levels. These factors influence the corrosion process in actual field conditions and would improve the model's accuracy in predicting structural behaviour under varying environmental circumstances.
4. **Parametric Studies on a Range of Structural Members:** Future research should extend the analysis to other structural members, such as beams, various cross-sectional designs, reinforcement configurations, and beam-column joints. This would provide a comprehensive understanding of how different structural components perform under varying conditions, including different grades of concrete and corrosion levels.
5. **Long-Term Studies on Corrosion Effects in Varying Environmental Conditions:** Conducting longitudinal studies to examine the impact of diverse environmental conditions on corrosion rates and structural degradation of RC elements would provide valuable data. These studies could inform predictive maintenance strategies and durability assessments for RC structures exposed to different climatic conditions.

Bibliography

ACI Code Committee 318-14. (2014). *Building Code Requirements for Structural Concrete and Commentary*.

ACI Committee 318-11. (2011). *Building code requirements for structural concrete and commentary*. American Concrete Institute.

Al-Osta, M. A., Al-Sakkaf, H. A., Sharif, A. M., Ahmad, S., & Baluch, M. H. (2018). Finite element modeling of corroded RC beams using cohesive surface bonding approach. *Computers and Concrete*, *22*(2), 167–182.

American Concrete Institute (ACI). (2008). *ACI 446R-08: Concrete Fracture*. American Concrete Institute.

Amini, S. N., & Rajput, A. S. (2022). Effect of Corrosion and Transverse Reinforcement on Flexural Response of 3D Finite Element Reinforced Concrete Beams. *International Conference on Civil, Structural and Transportation Engineering*, 122-136.

Amleh, L., & Ghosh, A. (2006). Modeling the effect of corrosion on bond strength at the steel–concrete interface with finite-element analysis. *Canadian Journal of Civil Engineering*, *33*(6), 673–682.

Anh Huy, P. P., Yuen, T. Y., Hung, C. C., & Mosalam, K. M. (2022). Seismic behaviour of full-scale lightly reinforced concrete columns under high axial loads. *Journal of Building Engineering*, *56*.

A.W. Taylor, C. Kuo, K. Wellenius, & D. Chung. (1997). *A Summary of Cyclic Lateral Load Tests on Rectangular Reinforced Concrete Columns* (NISTIR 5984). Building and Fire Research Laboratory, National Institute of Standards and Technology.

Azizinamini, A., Corley, W. G., & Johal, L. S. P. (1992). *Effects of Transverse Reinforcement on Seismic Performance of Columns*.

Bhargava, K., Ghosh, A. K., Mori, Y., & Ramanujam, S. (2008). Suggested Empirical Models for Corrosion-Induced Bond Degradation in Reinforced Concrete. *Journal of Structural Engineering*, *134*(2), 221–230.

Biondini, F., & Vergani, M. (2015). Deteriorating beam finite element for nonlinear analysis of concrete structures under corrosion. *Structure and Infrastructure Engineering*, *11*(4), 519–532.

Bru, D., González, A., Baeza, F. J., & Ivorra, S. (2018). Seismic behavior of 1960's RC buildings exposed to marine environment. *Engineering Failure Analysis*, *90*, 324–340.

Bureau of Indian Standard. (1993). *IS-13920 Ductile detailing of reinforced concrete structures subjected to seismic forces - Code of practice*.

Bureau of Indian Standard. (2019). *IS 10262:2019- Concrete Mix Proportioning- Guidelines (Second Revision)*.

Cabrera, J. G. (1996). Deterioration of Concrete Due to Reinforcement Steel Corrosion. *Cement & Concrete Composites*, *18*, 47–59.

Çağatay, I. H. (2005). Experimental evaluation of buildings damaged in recent earthquakes in Turkey. *Engineering Failure Analysis*, *12* (3), 440–452.

Cairns, J., Du, Y., & Law, D. (2008). Structural performance of corrosion-damaged concrete beams. *Magazine of Concrete Research*, *60*(5), 359–370.

Cairns, J., Plizzari, G. A., Du, Y., Law, D. W., & Franzoni, C. (2005). Mechanical Properties of Corrosion-Damaged Reinforcement. *Aci Materials Journal*, *102*, 256–264.

Canadian Standards Association. (2004). *CSA-A 23.3-04 Design of concrete structures*.

Canadian Standards Association A23.3-04. (2004). Canadian Standards Association standard A23.3-04 resistance factor for concrete in compression. *Canadian Journal of Civil Engineering*, *34*(9), 1029–1037.

Capozucca, R. (1995). Damage to reinforced concrete due to reinforcement corrosion. *Construction and Building Materials*, *9*(5), 295–303.

CEB-FIP Model code. (2010). *CEB-FIP Model code 2010: First complete draft, Volume 1* (Vol. 1). Fédération internationale du béton.

CEN. (2004). *Eurocode 2: Design of Concrete Structures – Part 1-1: General Rules and Rules for Buildings*. European Committee for Standardization.

Cheng, J., Luo, X., & Xiang, P. (2020). Experimental study on seismic behavior of RC beams with corroded stirrups at joints under cyclic loading. *Journal of Building Engineering*, *32*, 101489.

Choi, M.-H., & Lee, C.-H. (2022). Seismic Behavior of Existing Reinforced Concrete Columns with Non-Seismic Details under Low Axial Loads. *Materials*, *15*(3), 122-134.

Clark, L. A., Chan, A., & Du, Y. (2005). Residual capacity of corroded reinforcing bars. *Magazine of Concrete Research*, *57*, 135–147.

Coronelli, D. (2002). Corrosion Cracking and Bond Strength Modeling for Corroded Bars in Reinforced Concrete. *ACI Structural Journal*, *99*(3), 267–276.

Coronelli, D., & Gambarova, P. (2004). Structural Assessment of Corroded Reinforced Concrete Beams: Modeling Guidelines. *Journal of Structural Engineering, ASCE*, *130*(8), 1214–1224.

Dai, K. Y., Liu, C., Lu, D. G., & Yu, X. H. (2020). Experimental investigation on seismic behavior of corroded RC columns under artificial climate environment and electrochemical chloride extraction: A comparative study. *Construction and Building Materials*, *242*, 118014.

Dai, K. Y., Lu, D. G., & Yu, X. H. (2021). Experimental investigation on the seismic performance of corroded reinforced concrete columns designed with low and high axial load ratios. *Journal of Building Engineering*, *44*, 345-351.

Dassault Systems. (2022). *SIMULIA Abaqus FEA 6.14 Theory Manual and Documentation*.

Dizaj, E. A., Madandoust, R., & Kashani, M. M. (2018). Probabilistic seismic vulnerability analysis of corroded reinforced concrete frames including spatial variability of pitting corrosion. *Soil Dynamics and Earthquake Engineering*, *114*, 97–112.

El Maaddawy, T., & Soudki, K. (2007). A model for prediction of time from corrosion initiation to corrosion cracking. *Cement and Concrete Composites*, *29*(3), 168–175.

Eligehausen, R., Popov, I. E. P., & Bertero, V. V. (1983). *Local Bond Stress-Slip Relationships of Deformed Bars under Generalized Excitations*.

El-Joukhadar, N., Dameh, F., & Pantazopoulou, S. (2023). Seismic Modelling of Corroded Reinforced Concrete Columns. *Engineering Structures*, *275*.

Fernandez, I., Lundgren, K., & Zandi, K. (2018). Evaluation of corrosion level of naturally corroded bars using different cleaning methods, computed tomography, and 3D optical scanning. *Materials and Structures*, *51*(3), 78.

Gan, Y. (2000). *Bond Stress and Slip Modelling in Nonlinear Finite Element Analysis of Reinforced Concrete Structures*.

Ge, X., Dietz, M. S., Alexander, N. A., & Kashani, M. M. (2020). Nonlinear dynamic behaviour of severely corroded reinforced concrete columns: shaking table study. *Bulletin of Earthquake Engineering*, *18*(4), 1417–1443.

Henriques, J., Simões da Silva, L., & Valente, I. B. (2013). Numerical modeling of composite beam to reinforced concrete wall joints: Part I: Calibration of joint components. *Engineering Structures*, *52*, 747–761.

Hordijk, D. A., & Arend, D. (1991). *Local Approach to Fatigue of Concrete*. TU Delft.

IS-13920: (2016) *Ductile Design and Detailing of Reinforced Concrete Structures Subjected to Seismic Forces, Code of Practice. (First Revision)*

Kallias, A. N., & Imran Rafiq, M. (2010). Finite element investigation of the structural response of corroded RC beams. *Engineering Structures*, *32*(9), 2984–2994.

Kashani, M. M., Lowes, L. N., Crewe, A. J., & Alexander, N. A. (2012). Phenomenological hysteretic model for corroded reinforcing bars including inelastic buckling and low-cycle fatigue degradation. *Computers and Structures*, *156*(6), 58–71.

Kashani, M. M., Lowes, L. N., Crewe, A. J., & Alexander, N. A. (2015). Phenomenological hysteretic model for corroded reinforcing bars including inelastic buckling and low-cycle fatigue degradation. *Computers & Structures*, *156*, 58–71.

Lavorato, D., Fiorentino, G., Pelle, A., Rasulo, A., Bergami, A. V., Briseghella, B., & Nuti, C. (2020). A corrosion model for the interpretation of cyclic behavior of reinforced concrete sections. *Structural Concrete*, *21*(5), 1732–1746.

Lee, C., Bonacci, J., Thomas, M., Maalej, M., Khajehpour, S., Hearn, N., Pantazopoulou, S., & Sheikh, S. (2000). *Accelerated corrosion and repair of reinforced concrete columns using carbon fibre reinforced polymer sheets*.

Lee, H. S., & Cho, Y. S. (2009). Evaluation of the mechanical properties of steel reinforcement embedded in concrete specimen as a function of the degree of reinforcement corrosion. *International Journal of Fracture*, *157*(1–2), 81–88.

Lee, J., Fenves, G. L., & Member, A. (1998). Plastic-damage model for cyclic loading of concrete structures. *Journal of Engineering Mechanics*, *124*(8), 892–900.

Li, D., Wei, R., Xing, F., Sui, L., Zhou, Y., & Wang, W. (2018). Influence of Non-uniform corrosion of steel bars on the seismic behavior of reinforced concrete columns. *Construction and Building Materials*, *167*, 20–32.

Li, Z., & Gan, D. (2022). Cyclic behavior and strength evaluation of RC columns with dune sand. *Journal of Building Engineering*, *47*, 103801.

Li, Z., Yu, C., Xie, Y., Ma, H., & Tang, Z. (2019). Size effect on seismic performance of high-strength reinforced concrete columns subjected to monotonic and cyclic loading. *Engineering Structures*, *183*, 206–219.

Lubliner. J, Oliver. J. Oller. S. Onate. E. (1989). Plastic damage model for concrete. *International Journal of Solids Structures*, *25*, 299–326.

Ma, Y., Che, Y., & Gong, J. (2012). Behavior of corrosion damaged circular reinforced concrete columns under cyclic loading. *Construction and Building Materials*, *29*, 548–556.

Maaddawy, T. El, Soudki, K., & Topper, T. (2005). Analytical Model to Predict Nonlinear Flexural Behavior of Corroded Reinforced Concrete Beams. *American Concrete Institute*, *102*(4), 550–559.

Mander, J. B., Priestley, M. J. N., & Park, R. (1988). Theoretical Stress-strain Model for Confined Concrete. *Journal of Structural Engineering*, 1804–1826.

Mo, Y. L., & Wang, S. J. (2000). Seismic Behavior of RC Columns with Various Tie Configurations. *Journal of Structural Engineering*, *126*(10), 1122–1130.

Mohebkhah, A., & Tazarv, J. (2021). Equivalent viscous damping for linked column steel frame structures. *Journal of Constructional Steel Research*, *179*, 106506.

Murcia-Delso, J., & Benson Shing, P. (2015). Bond-Slip Model for Detailed Finite-Element Analysis of Reinforced Concrete Structures. *Journal of Structural Engineering*, *141*(4).

Narayanan, S. (2011). Design of confinement reinforcement for RC columns. *The Indian Concrete Journal*, 25–35.

New Zealand Standard. (2006). *NZS 3101.1:2006 Design of concrete structures*.

Ou, Y. C., & Nguyen, N. D. (2014). Plastic hinge length of corroded reinforced concrete beams. *ACI Structural Journal*, *111*(5), 1049–1058.

Ou, Y. C., & Nguyen, N. D. (2016). Influences of location of reinforcement corrosion on seismic performance of corroded reinforced concrete beams. *Engineering Structures*, *126*, 210–223.

Ou, Y. C., Susanto, Y. T. T., & Roh, H. (2016). Tensile behavior of naturally and artificially corroded steel bars. *Construction and Building Materials*, *103*, 93–104.

Palsson, R., & Mirza, M. S. (2002). Mechanical response of corroded steel reinforcement of abandoned concrete bridge. *ACI Structural Journal*, *99*(2), 157–162.

Park, R. (1989). *Evaluation of Ductility of Structures and Structural Assemblages from Laboratory Testing*. 155-166

Paultre, P., & Légeron, F. (2008). Confinement Reinforcement Design for Reinforced Concrete Columns. *Journal of Structural Engineering*, *134*(5), 738–749.

Qu, F., Li, W., Dong, W., Tam, V. W. Y., & Yu, T. (2021). Durability deterioration of concrete under marine environment from material to structure: A critical review. In *Journal of Building Engineering* 35, 102074.

Rajput, A. S., & Sharma, U. K. (2018a). Corroded reinforced concrete columns under simulated seismic loading. *Engineering Structures*, *171*, 453–463.

Rajput, A. S., & Sharma, U. K. (2018b). Seismic Behavior of Under Confined Square Reinforced Concrete Columns. *Structures*, *13*, 26–35.

Revathy, J., Suguna, K., & Raghunath, P. N. (2009). Effect of Corrosion Damage on the Ductility Performance of Concrete Columns. *American Journal of Engineering and Applied Sciences*, *2*, 324–327.

Rodrigues, H. (2018). Influence of seismic loading on axial load variation in reinforced concrete columns. *e-GFOS*, *9*(16), 37–49.

Saatcioglu M, & Ozcebe G. (1989). Response of Reinforced Concrete Columns to Simulated Seismic Loading. *ACI Structural Journal*, *86*(1), 1–12.

Sakai K, & Shamim A. (1989). What Do We Know About Confinement in Reinforced Concrete Columns? (A critical review of previous work and code provisions). *ACI Structural Journal*, *86*(2), 192–207.

Shi, Q., Ma, L., Wang, Q., Wang, B., & Yang, K. (2021). Seismic performance of square concrete columns reinforced with grade 600 MPa longitudinal and transverse reinforcement steel under high axial load. *Structures*, *32*, 1955–1970.

Stanish, K. (1997). *Corrosion Effects on Bond Strength in Reinforced Concrete*. University of Toronto.

Tanaka, H., & Park, R. (1993). *Seismic Design and Behavior of Reinforced Concrete Columns with Interlocking Spirals*.

Val, D. V, & Chernin, L. (2001). *Serviceability Reliability of Reinforced Concrete Beams with Corroded Reinforcement*.

Vu, N. S., Yu, B., & Li, B. (2016). Prediction of strength and drift capacity of corroded reinforced concrete columns. *Construction and Building Materials*, *115*, 304–318.

Wang, X. H., & Liang, F. Y. (2008). Performance of RC columns with partial length corrosion. *Nuclear Engineering and Design*, *238*(12), 3194–3202.

Wang, Y., Chen, P., Liu, C., & Zhang, Y. (2017). Size effect of circular concrete-filled steel tubular short columns subjected to axial compression. *Thin-Walled Structures*, *120*, 397–407.

Wu, B., Sun, G., Li, H., & Wang, S. (2022). Effect of variable axial load on seismic behaviour of reinforced concrete columns. *Engineering Structures*, *250*, 113388.

Wu, Y.-F., & Zhao, X.-M. (2013). Unified Bond Stress–Slip Model for Reinforced Concrete. *Journal of Structural Engineering*, *139*(11), 1951–1962.

Xiaoming, Y., & Hongqiang, Z. (2012). Finite Element Investigation on Load Carrying Capacity of Corroded RC Beam Based on Bond-Slip. *Jordan Journal of Civil Engineering*, *6*(1), 118–134.

Y. Fujita, & R. Ishimaru. (1994). Study on internal friction angle and tensile strength of plain concrete, *Fracture Mechanics of Concrete Structures Proceeding (FRAMCOS-3)*, 1–10.

Yang, S. Y., Song, X. B., Jia, H. X., Chen, X., & Liu, X. La. (2016). Experimental research on hysteretic behaviors of corroded reinforced concrete columns with different maximum amounts of corrosion of rebar. *Construction and Building Materials*, *121*, 319–327.

Yuan, W., Guo, A., Yuan, W., & Li, H. (2018). Shaking table tests of coastal bridge piers with different levels of corrosion damage caused by chloride penetration. *Construction and Building Materials*, *173*, 160–171.

Yuan, W., Zhang, Y., Xiao, Q., & Liu, Z. (2023). Effect of the axial compression ratio on the seismic behavior of resilient concrete walls with concealed column stirrups. *62*(1), 234-244.

Yuen, T. Y. P., & Kuang, J. S. (2017). Revisiting the effect of axial force ratio on the seismic behaviour of RC building columns. *Structural Engineering International*, *27*(1), 88–100.

Zandi Hanjari, K., Kettil, P., & Lundgren, K. (2011). Analysis of Mechanical Behavior of Corroded Reinforced Concrete Structures. *ACI Structural Journal*, *108*(5), 532–541.

Zandi, K., Kettil, P., & Lundgren, K. (2011). Analysis of Mechanical Behavior of Corroded Reinforced Concrete Structures. *ACI Structural Journal*, *108*, 532–541.

Zhang, Y., Bicici, E., Sezen, H., & Zheng, S. (2020). Reinforcement slip model considering corrosion effects. *Construction and Building Materials*, *235-246*.

Zhu, W., Jia, J., Gao, J., & Zhang, F. (2016). Experimental study on steel reinforced high-strength concrete columns under cyclic lateral force and constant axial load. *Engineering Structures*, *125*, 191–204.

Ziari, A., & Kianoush, M. R. (2014). Finite-Element Parametric Study of Bond and Splitting Stresses in Reinforced Concrete Tie Members. *Journal of Structural Engineering*, *140*(5), 4013106.

List of Publications from Thesis

International Journals

1. Amini, S.A., & Rajput, A.S. (2022). Effect of Corrosion Location and Transverse Reinforcement on Flexural-Ductile Response of Reinforced Concrete Beams. International Journal of Civil Infrastructure, 5, 104-114.

2. Amini, S.A., & Rajput, A.S. (2024). Seismic Response of Ductile Reinforced Concrete Corroded Columns with variation of Axial loads. Structures, 65, 106699.

3. Amini, S.A., & Rajput, A.S. (2024). Seismic performance of ductile and non-ductile reinforced concrete columns under varied axial compression. Structural Engineering and Mechanics, 91 (5), 427-441.

4. Amini, S.A., & Rajput, A.S. (2025). Effect of Reinforcement Corrosion and Axial Load Levels on Seismic Response of Non-Ductile Reinforced Concrete Columns. *Structural Concrete.* 25, 1-18.

5. Amini, S.A., & Rajput, A.S. (To be submitted). Structural Response of Reinforced Concrete Beams Affected by Accelerated Corrosion.

International Conferences

1. Amini, S.A., & Rajput, A.S. (2023). Effect of Inadequate Anchorage Detailing on Flexural Response of Reinforced Concrete Beams. *International Conference on Condition Assessment, Rehabilitation & Retrofitting of Structures*, IIT Hyderabad.

2. Amini, S.A., & Rajput, A.S. (2024). Assessing The Seismic Resilience of Lightly Reinforced Corroded Columns: An Experimental and Numerical Study. *World Conference on Earthquake Engineering, WCEE- Milan*.